Astronomy Letters, Vol. 31, No. 7, 2005, pp. 429–441. Translated from Pis'ma v Astronomicheskiĭ Zhurnal, Vol. 31, No. 7, 2005, pp. 483–485.

Parameters of the Classical Type-IIP Supernova SN 1999em

P. V. Baklanov[1*], S. I. Blinnikov[1,2], and N. N. Pavlyuk[1]

[1] *Sternberg Astronomical Institute, Universitetskiĭ pr. 13, Moscow, 119992 Russia*

[2] *Institute for Theoretical and Experimental Physics, ul. Bol'shaya Cheremushkinskaya 25, Moscow, 117259 Russia*

Received February 22, 2005

Abstract—Based on observations of SN 1999em, we determined the physical parameters of this supernova using hydrodynamic calculations including nonequilibrium radiative transfer. Taking the distance to SN 1999em estimated by the expanding photosphere method (EPM) to be $D = 7.5$ Mpc, we found the parameters of the presupernova: radius $R = 450R_\odot$, mass $M = 15M_\odot$, and explosion energy $E = 7 \times 10^{50}$ erg. For the distance $D = 12$ Mpc determined from Cepheids, R, M, and E must be increased to the following values: $R = 1000R_\odot$, $M = 18M_\odot$, and $E = 10^{51}$ erg. We show that one cannot restrict oneself to using the simple analytical formulas relating the supernova and presupernova parameters to obtain reliable parameters for type-IIP presupernovae. © *2005 Pleiades Publishing, Inc.*

Key words: *supernovae and supernova remnants, models, radiative transfer.*

INTRODUCTION

Recent years have brought more and more data on supernovae (SNe) in all ranges of the electromagnetic spectrum. Studying these objects is important both for understanding the physics of their explosions and for cosmology. The construction of computer models is a modern tool for studying the physics of SNe. The reliability of a model can be determined by comparing the model results with observational data. Since, in general, SNe are observed at great distances (tens and hundreds of Mpc), comprehensive observational data (photometry and spectra) are difficult to obtain for such objects. Particularly detailed observations can be performed only for nearby SNe. The type-IIP SN 1999em (Leonard *et al.* 2001; Elmhamdi *et al.* 2003a, 2003b; Pastorello *et al.* 2005) is among these thoroughly studied objects. SN 1999em exploded in the nearby galaxy NGC 1637 at a distance that was estimated from various measurements to be between 7.5 and 12.4 Mpc. A wealth of photometric and spectroscopic data has been accumulated for this SN through the observations of its explosion from the very outset and over a wide spectral range. In their recent studies, Nadyozhin (2003) and Hamuy (2003) used SN 1999em along with other SNe to determine the parameters of the presupernovae. Based on these parameters, they reached conclusions about the correlation between various quantities, for example, between the presupernova mass and the observed plateau luminosity etc.

Nadyozhin (2003) and Hamuy (2003) estimated the masses M, radii R, and explosion energies E for a number of SNe II. Based on the observed values of M_V, Δt, and $u_{\rm ph}$ on the plateau of the light curve, they determined M, R, and E using relations from Litvinova and Nadyozhin (1983, 1985). Popov (1993) analytically derived formulas similar to those obtained by Litvinova and Nadyozhin (1983, 1985).

In this paper, we focus our attention on SN 1999em as one of the most extensively observed SNe. The goal of our study is to construct a detailed nonevolutionary presupernova model that reproduces most faithfully the observed U, B, V, I, and R fluxes from SN 1999em and the photospheric velocity. In addition, our objective is to ascertain how closely the results obtained from the simple formulas from Litvinova and Nadyozhin (1983, 1985) agree with our much more complex and accurate radiation-hydrodynamics calculations.

OBSERVATIONS

SN 1999em was discovered on October 29, 1999, at the Lick Observatory during a search for SNe (Lacey *et al.* 1999a, 1999b). SN 1999em exploded in the galaxy NGC 1637; its measured magnitude was $m \sim 13\overset{m}{.}5$. In the image of the same region obtained nine days earlier, there is nothing at the SN location (the limiting magnitude in this image is $m \sim 19^m$ (Leonard *et al.* 2001)). This means that the

[*] E-mail: baklanovp@gmail.com

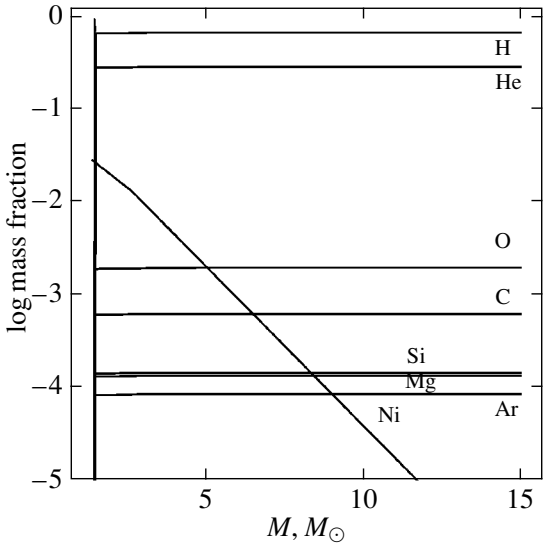

Fig. 1. Distribution of elements in the presupernova for the R450_M15_Ni004_E7 model.

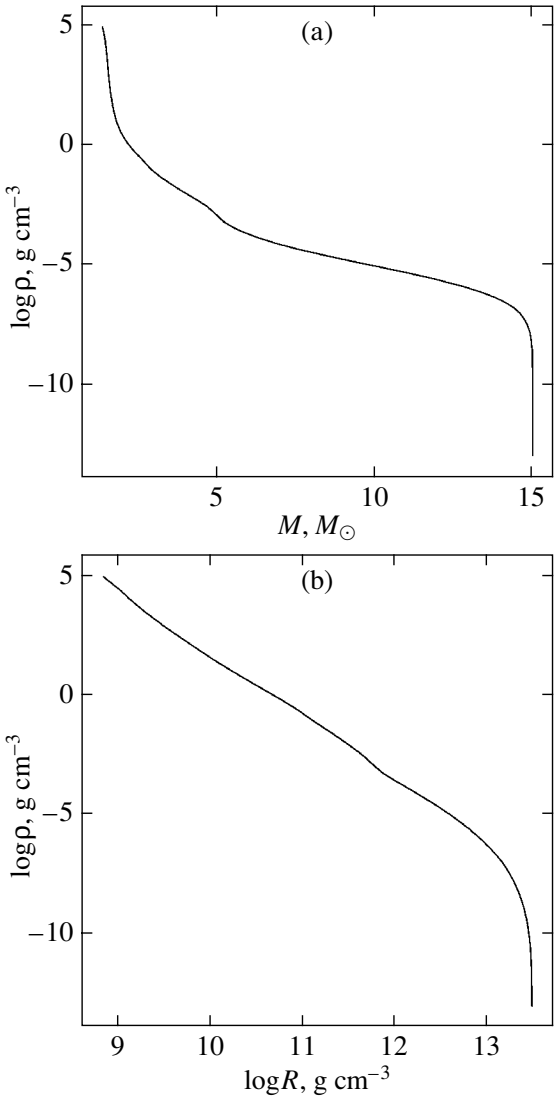

Fig. 2. Density versus (a) mass and (b) radius for the R450_M15_Ni004_E7 model.

SN was discovered almost immediately after its explosion. Photometric and spectroscopic observations allowed it to be classified as an SN IIP with a distinct plateau. The early and weak radio emission suggested a low density of the material surrounding the presupernova. This implies that there was no active mass outflow from the star before its explosion, and we see a "pure" SN explosion, without any interaction with the surrounding interstellar matter.

According to Baron *et al.* (2000), the reddening was assumed to be $E(B-V) = 0.1$.

The distance to the host galaxy was measured by several methods. The discrepancy between the distances determined by different methods is more than 50%. One group of results clustered near 7.8 Mpc. The expanding-photosphere method (EPM) yielded 7.5 Mpc (Hamuy *et al.* 2001) and 8.2 Mpc (Leonard *et al.* 2001); 7.8 Mpc was obtained from the brightest supergiants of the galaxy (Sohn and Davidge 1998). According to the catalog by Tully (1988), the distance to NGC 1637 is 8.9 Mpc. An appreciably larger value of 11.7 Mpc was obtained by Leonard *et al.* (2003) from Cepheids.

In this paper, we take a distance to SN 1999em of 7.5 Mpc as the value confirmed by a larger number of studies than the distance increased by 50% that was determined by Leonard *et al.* (2003) from Cepheids. However, Baron *et al.* (2004) found the distance to SN 1999em by the SEAM (Spectral-fitting Expanding Atmosphere Model) method to be 12.48 Mpc, i.e., close to the value by Leonard *et al.* (2003). We additionally studied the SN for this distance. Note in advance that the presupernova model changed toward a significant increase in the radius and an increase in the mass and explosion energy.

MODELING

We constructed the presupernova models in hydrostatic equilibrium by assuming a power-law dependence of the temperature on the density (cf. Chugai *et al.* 2004),

$$T \propto \rho^{\alpha}. \qquad (1)$$

For complete ionization and homogeneous chemical composition, this hydrostatic configuration is close to a polytrope with an index $1/\alpha$. The deviation

Table 1. Comparison of the parameters of the models by Nadyozhin (2003) and Hamuy (2003)

Initial parameters	Nadyozhin (2003)	Hamuy (2003)
D, Mpc	12.38	10.7
M_V	-16.78^m	-16.44^m
Δt, days	110	124
$u_{\rm ph}$, km s^{-1}	2900	3290
Derived parameters		
E, foe	0.63	1.2
M, $M_\odot$	13.2	27
R, $R_\odot$	569	249

from the polytropic model increases in the outer layers due to ion recombination and inhomogeneous chemical composition (Fig. 1). At the center of this configuration, we isolated a heavy gravitating point-like core (with a radius of $R_{\rm c} = 0.1R_\odot$, which is much larger than the actual core, but is much smaller than the radial step of the computational grid used in our hydrodynamic modeling). The computed structure is shown in Fig. 2. It is similar to the structure of a red supergiant.

As the shock wave travels from the center of the presupernova outward, a strong Rayleigh–Taylor instability (Basko 1994) that leads to a mixing of the SN material arises behind the shock front. In our modeling, we assumed that all elements, except ^{56}Ni, were uniformly mixed throughout the expanding SN envelope. Since the amount and distribution of ^{56}Ni synthesized during the explosion plays a crucial role in the SN luminosity, we made its radial distribution closer to the actual distribution, which falls off logarithmically away from the center. An approximate distribution of elements in the presupernova is shown in Fig. 1.

The SN explosion was modeled by the release of thermal energy E in a layer with a mass of $0.06M_\odot$ in 0.1 s, which is much shorter than the hydrodynamic time of the presupernova. As long as the energy release time is short compared to the hydrodynamic time, the resulting light curve does not depend on the particular features of the explosion mechanism (Imshennik and Nadyozhin 1982).

The Models by Nadyozhin and Hamuy

Nadyozhin (2003) and Hamuy (2003) determined the masses M, radii R, and explosion energies E for a number of SNe II. Based on the observed values of M_V, Δt, and $u_{\rm ph}$ on the plateau of the light curve, they obtained M, R, and E using relations from Litvinova and Nadyozhin (1983, 1985).

They included SN 1999em in their studies and obtained the parameters for it given in Table 1.

In their studies, Nadyozhin (2003) and Hamuy (2003) relied on the papers by Litvinova and Nadyozhin (1983, 1985), but their estimates of the presupernova parameters for SN 1999em differ greatly. Thus, for example, we see from Table 1 that the mass of the expelled envelope and the explosion energy in Nadyozhin's model are a factor of two lower than those in Hamuy's model, while the initial radius of the presupernova is twice as large, although the initial data differ by about 10%.

The distances D in these two models and, hence, the values of M_V also differ significantly. According to

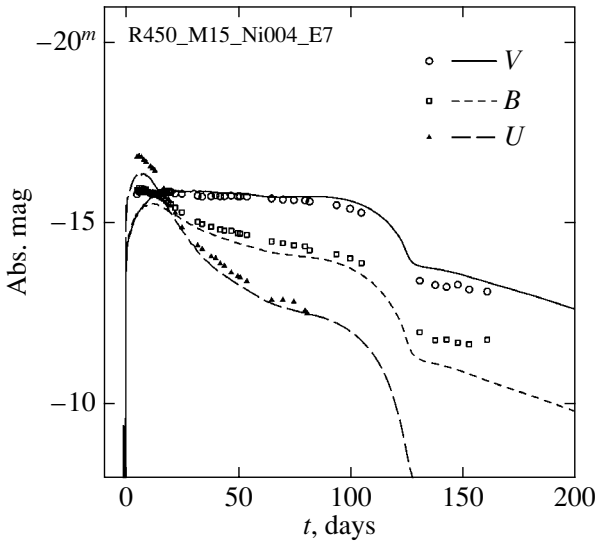

Fig. 3. U, B, V light curves of SN 1999em for model No. 1. Time from the explosion is along the horizontal axis.

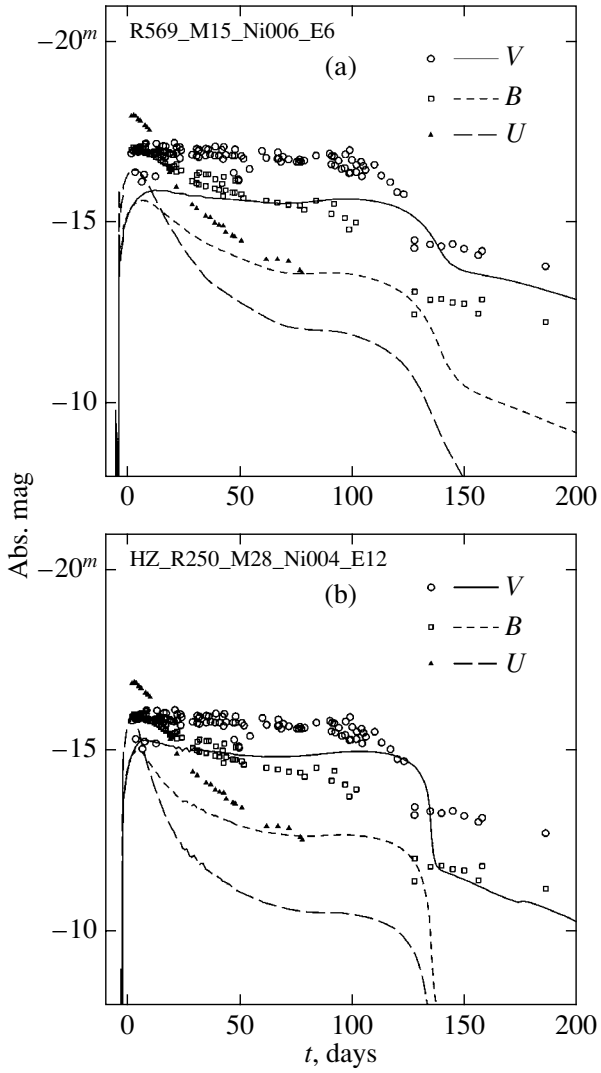

Fig. 4. Light curves of SN 1999em with the initial data from Nadyozhin (2003), $D = 12.38$ Mpc (a), and Hamuy (2003), $D = 7.5$ Mpc (b). The heavy-element abundance is $Z = 0.03$. Time from the first SN observation is along the horizontal axis.

the formulas by Litvinova and Nadyozhin (1985), the values of E, M, and R depend on the distance as

$$E \sim D^{-0.675}, \quad M \sim D^{-1.17}, \quad R \sim D^{2.86}. \quad (2)$$

Therefore, it is crucially important to know D with the maximum possible accuracy. However, different values of D can account for the difference in R alone, but not the differences in E and M: the D dependence for them is too weak. If we look at the UBV light curves in the paper by Litvinova and Nadyozhin (1983), we can see that they are very similar and, contrary to the observations, have the same plateau: actual SNe II have a clear plateau only in V and longer-wavelength bands, but not in B and U (see Leonard *et al.* 2001). This is because the models from Litvinova and Nadyozhin (1983, 1985) were computed in the approximation of radiative heat conduction.

This implies that more detailed models are required to reproduce the observed U, B, V fluxes. As an example, we consider the well-studied SN 1999em in an effort to determine its parameters using a more complex multigroup modeling of the SNe-II light curves. We used our STELLA code (Blinnikov and Bartunov 1993; Blinnikov *et al.* 1998; Sorokina and Blinnikov 2004). The algorithms included in the STELLA package model SNe with allowance made for the much richer physics than that in the papers by Litvinova and Nadyozhin (1983, 1985). Instead of the radiative heat conduction approximation, we describe the radiative transfer without assuming an equilibrium photon spectrum (in the multigroup approximation). We use much more accurate expressions for the opacity (including about 150 000 spectral lines). This allows us to reproduce with qualitative faithfulness the faster decline in the B and U fluxes than that in the V band at the plateau stage, as observed (Fig. 3). In addition, we take into account the SN envelope heating through the $^{56}\mathrm{Ni} \rightarrow {}^{56}\mathrm{Co} \rightarrow {}^{56}\mathrm{Fe}$ decays, including the transfer of gamma-ray photons. Baklanov (2002) constructed a theoretical catalog for M_{bol} and UBV light curves of SNe II obtained at various M, R, and E of the presupernovae. In addition to the parameters used by Litvinova and Nadyozhin (1983, 1985), the mass M_{Ni} of radioactive ^{56}Ni was considered.

For SN 1999em, we constructed a nonevolutionary presupernova model with an extended hy-

Table 2. Basic parameters of the models

No.	Model	$R, R_\odot$	$M, M_\odot$	$E, 10^{51}$ erg	$M_{\rm Ni}, M_\odot$	V	Δt	$u_{\rm ph}$
1	R450_M15_Ni004_E7	450	15	0.7	0.04	−15.8	120	3.0
2	R1000_M18_Ni006_E10	1000	18	1	0.06	−16.6	106	2.7
3	HZ_R250_M28_Ni004_E12	250	28	1.2	0.04	−14.8	119	3.3
4	NZ_R569_M15_Ni006_E6	569	15	0.6	0.06	−14.7	99	3.1
5	H_R250_M28_Ni004_E12	250	28	1.2	0.04	−15.5	123	3.2
6	N_R569_M15_Ni006_E6	569	15	0.6	0.06	−15.7	124	2.3
7	R600_M15_Ni008_E10	600	15	1	0.08	−15.5	95	3.0
8	R750_M12_Ni004_E12	750	12	1.2	0.04	−15.4	105	2.6
9	R900_M15_Ni004_E8	900	15	0.8	0.04	−16.6	72	4.0
10	R200_M15_Ni004_E10	200	15	1.0	0.04	−16.3	109	3.9
11	R300_M15_Ni004_E7	300	15	0.7	0.04	−16.8	74	4.5
12	R450_M19_Ni004_E7	450	19	0.7	0.04	−16.5	100	3.2

Note. At the input: R, M, E, and $M_{\rm Ni}$ for the presupernova. At the output: V—the absolute V magnitude in the middle of the plateau; Δt (days)—the plateau duration in V; and $u_{\rm ph}$ (10^3 km s^{-1})—the photospheric velocity of the SN material in the middle of the plateau in V.

drogen envelope, as in the papers by Litvinova and Nadyozhin (1983, 1985), but more realistic, since it has a compact massive core and ^{56}Ni mixing in the envelope, as in the models for SN 1987A (Blinnikov *et al.* 1998). Litvinova and Nadyozhin (1983, 1985) took $Z = 0.044$, while Maciel and Costa (2003) and Pilyugin *et al.* (2004) obtained $Z = 0.01$ for H II regions in NGC1637. In our first models, the hydrogen mass fraction in the envelope was $X = 0.7$; the metallicity was taken for the first models to be $Z = 0.03$ (50% higher than the value for the standard cosmic distribution of elements (Anders and Grevesse 1989) and 50% lower than that in the papers by Litvinova and Nadyozhin (1983, 1985)).

We first constructed two presupernovae with the radii, masses, and explosion energies suggested by Hamuy and Nadyozhin. We then modeled the explosion by the release of thermal energy E at the center (models Nos. 3 and 4 in Table 2).

Figure 4 shows our model light curves computed with the presupernova (and reddening) parameters from Nadyozhin (2003) and Hamuy (2003). We see that the model light curves constructed from the data by Nadyozhin and Hamuy differ significantly and do not reproduce the observations very well. For example, the differences at the plateau stage are $1\overset{m}{.}5$ and more than 2^m in the V and U bands, respectively.

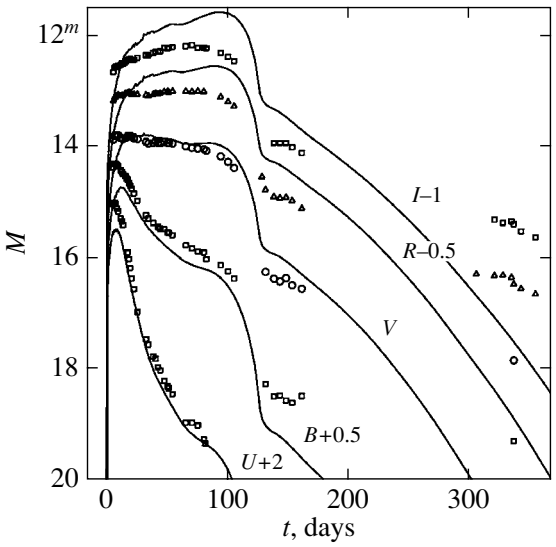

Fig. 5. U, B, V, R, I light curves of SN 1999em for model No. 1. Time from the explosion is along the horizontal axis.

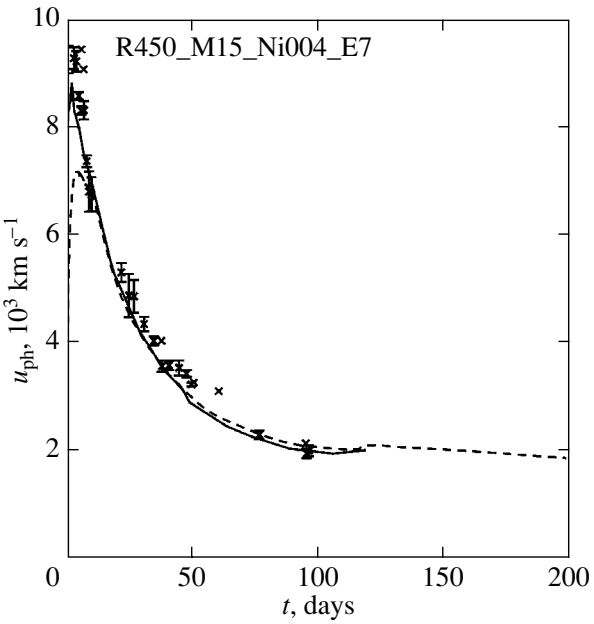

Fig. 6. Photospheric velocity for model No. 1. The crosses represent the observed values, the solid curve indicates the velocity obtained from our hydrodynamic modeling at the $\tau = 2/3$ level, and the dashed line represents the fit $u_{\rm ph} \approx R_{\rm ph}/t$. Time from the explosion is along the horizontal axis.

The Set of Supernova Models

There is no method that would allow us to solve the inverse problem, i.e., to determine the parameters of the presupernova that produced this explosion from observational data. We can only construct a model with specified parameters and see how accurately it reproduces the observations, e.g., as we did for the data by Nadyozhin and Hamuy.

In our modeling, we varied the parameters that affected most strongly the SN development over a wide range: the radius from 200 to 2000 $R_\odot$, the mass from 6 to $30M_\odot$, the ^{56}Ni mass from 0.01 to $0.08M_\odot$, and the explosion energy from 0.6 to 2×10^{51} erg. As we show below, the distribution of elements (their percentage abundance in the presupernova) plays a major role. Subsequently, we constructed the models, compared them with the observations, adjusted the initial conditions, and recomputed the models. The most interesting models are presented in Table 2. Models Nos. 3 and 4 correspond to the models by Hamuy and Nadyozhin, respectively.

The R450_M15_Ni004_E7 Model

As a result, we obtained the model that was closest in its data to the observations; it was called R450_M15_Ni004_E7 because of its main parameters (model No. 1 in Table 2). Before it exploded, the presupernova was a star with a mass of $15M_\odot$ and a radius of $450R_\odot$. Hydrogen, helium, and elements heavier than He accounted for 70%, 29.6%, and only 0.4% of the envelope, respectively. The low metallicity agrees with the modeled spectra by Baron *et al.* (2000). The distribution of elements in the presupernova for model No. 1 is shown in Fig. 1. The explosion was modeled by the release of energy $E = 7 \times 10^{50}$ erg near the center.

By fitting the model light curves, we found the best agreement with the observations (Fig. 3) precisely for this model at the distance $D = 7.5$ Mpc to the supernova (Hamuy *et al.* 2001). Figure 3 shows the U, B, V light curves for the absolute magnitudes corrected for the reddening $E(B-V) = 0.1$. The U, B, V, R, I light curves on a longer time interval and for the observed rather than absolute magnitudes are shown in Fig. 5.

Comparing the model and observed light curves, we found that the explosion of SN 1999em occurred on October 24, 1999, and was detected at the Lick Observatory 5 days later. Another 2.7 days later, it reached its maximum light in U.

It is interesting to compare the photospheric velocity $u_{\rm ph}$ with its observed values for the same model. The good agreement between the computed and observed values of $u_{\rm ph}$ in Fig. 6 is a weighty independent argument for choosing precisely this model. The dashed curve in Fig. 6 indicates a simple fit, $u_{\rm ph} \approx$

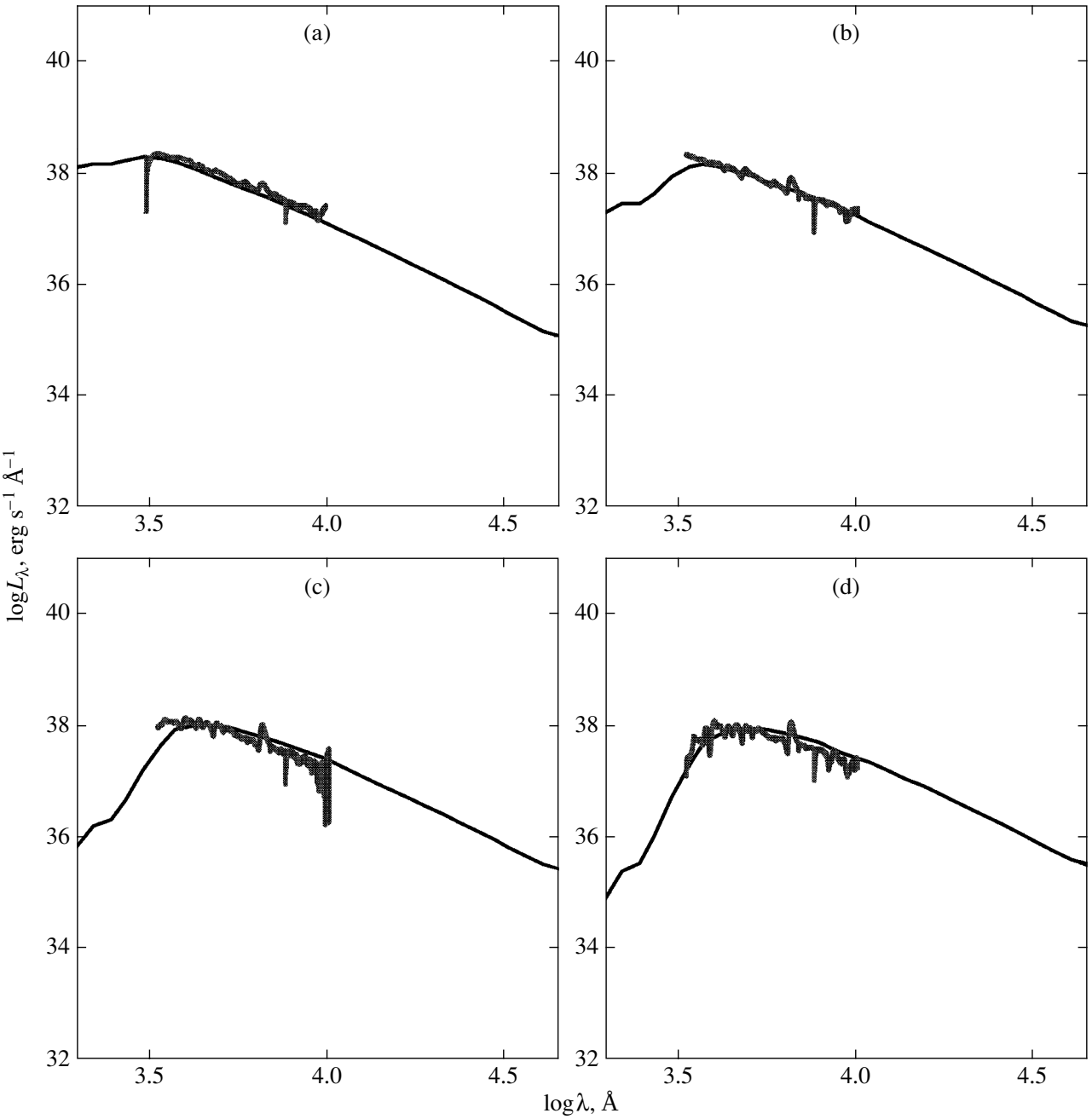

Fig. 7. Spectra for (a) October 30, 1999, (b) November 3, (c) November 9, and (d) November 14, 1999, for model No. 1.

$R_{\rm ph}/t$, which is applicable at the free (homologous) expansion stage. We see that $u_{\rm ph}$ at the $\tau = 2/3$ level is equal to $R_{\rm ph}/t$ only starting from day 15. This suggests that the EPM (Hamuy *et al.* 2001; Leonard *et al.* 2001) can be applied not earlier than this time.

Our model cannot completely reproduce the SN spectrum, since we do not resolve individual spectral lines in our calculations. The frequency range was broken down into a hundred groups in the numerical calculations; therefore, such fine features as spectral lines cannot be reproduced in the spectrum. Nevertheless, it is interesting to see how the computed spectrum fits the observed spectrum. We also plotted such curves for seven observing times obtained within the first two months after the onset of the explosion. We see from Figs. 7 and 8 that good agreement is achieved. Data on the observed spectra were retrieved from the Internet (Hamuy 2000).

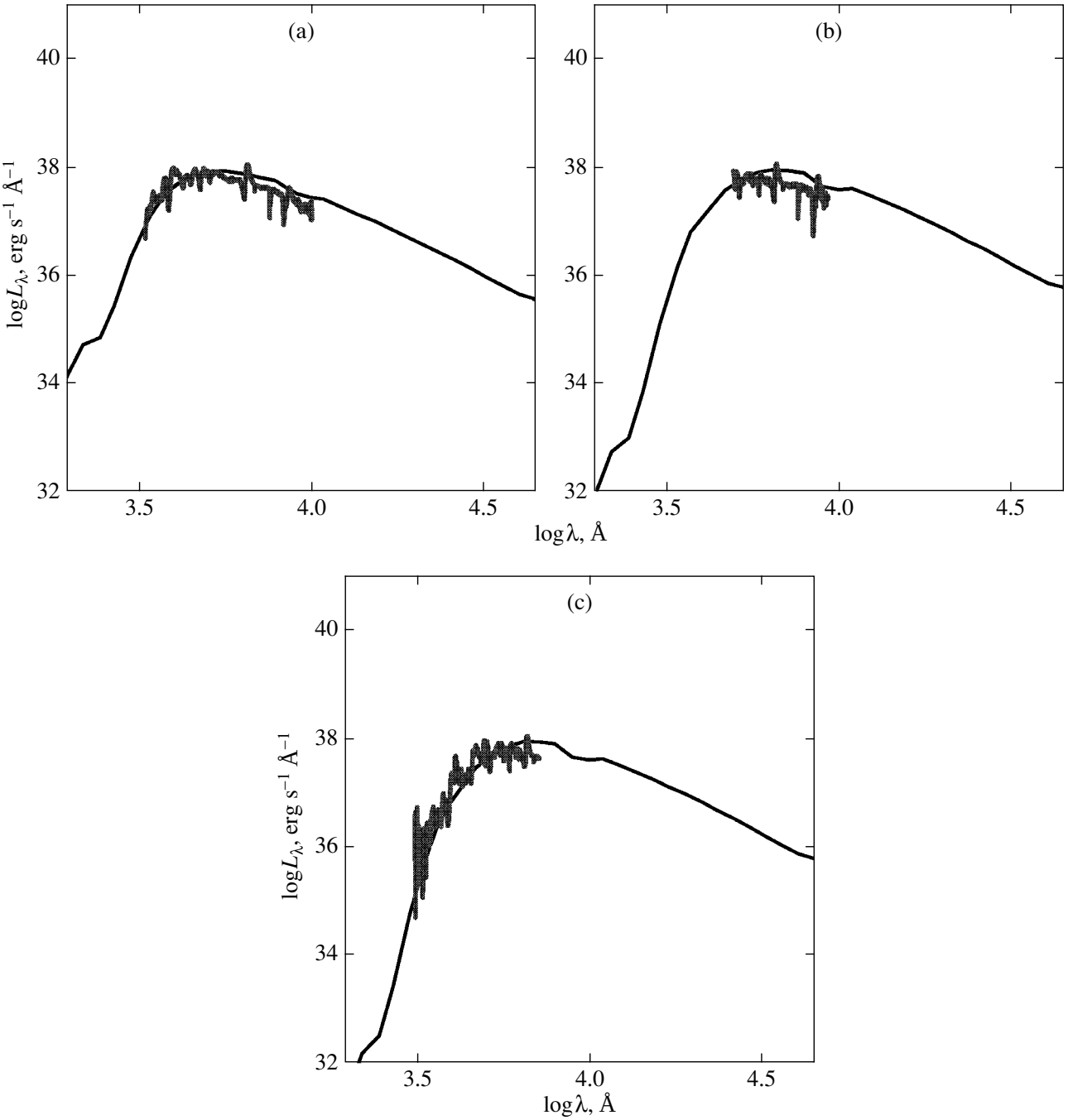

Fig. 8. Spectra for (a) November 19, 1999, (b) December 16, 1999, and (c) December 31, 1999, for model No. 1.

The R1000_M18_Ni006_E10 Model

Baron *et al.* (2004) estimated the distance to SN 1999em to be 12.48 Mpc, a value that is close to 11.7 Mpc (Leonard *et al.* 2003) determined from Cepheids, thereby strengthening the long distance scale to SN 1999em. Nadyozhin (2003) also used a similar distance, 12.38 Mpc. We took $D = 12.38$ Mpc from Nadyozhin (2003) as the basis for the second series of calculations; accordingly, the distance modulus for SN 1999em increased by more than 1^m. The model described above is invalid for this distance, since the observed light curves shifted significantly.

Having done work similar to that described above,

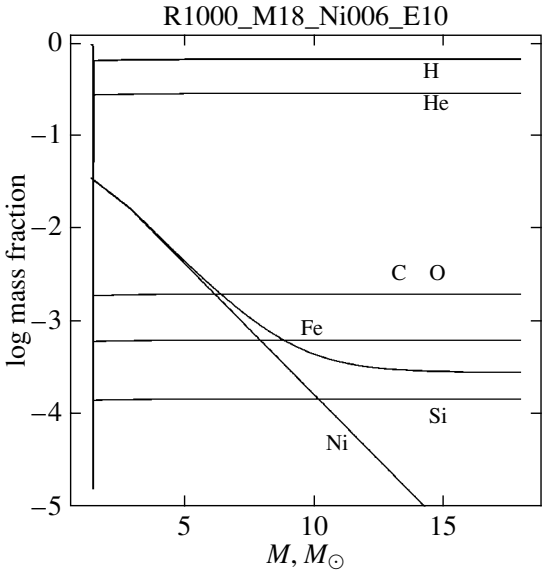

Fig. 9. Distribution of elements in the presupernova for model No. 2.

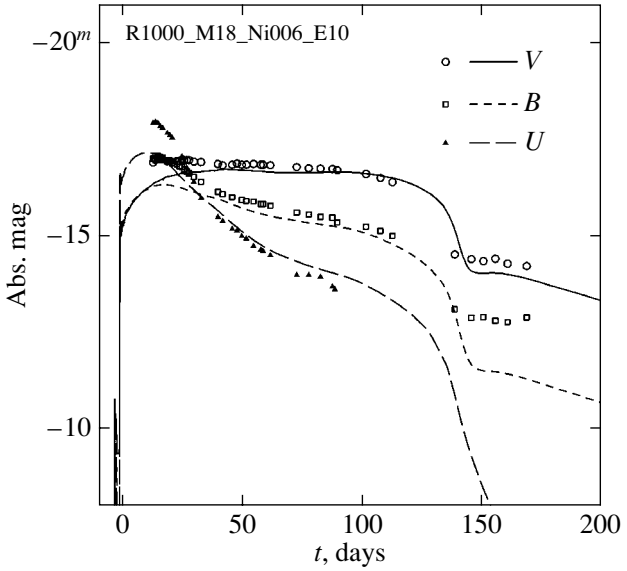

Fig. 11. Light curves of SN 1999em for model No. 2. $D = 12.38$ Mpc, the heavy-element abundance is $Z = 0.004$. Time from the explosion is along the horizontal axis.

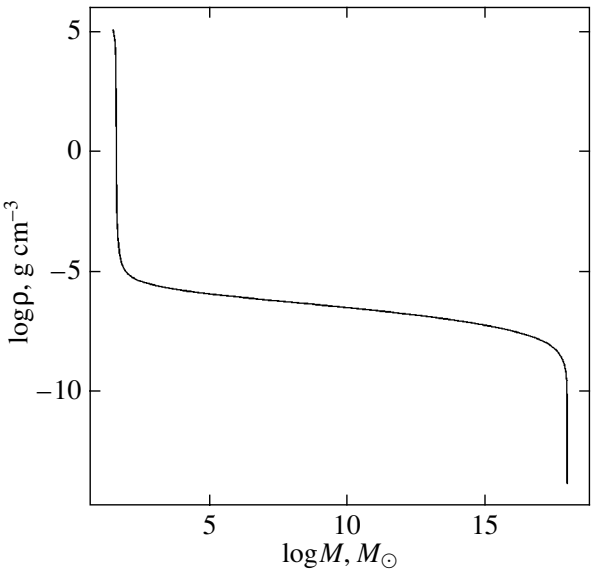

Fig. 10. Density versus mass (the Lagrangian coordinate) for model No. 2.

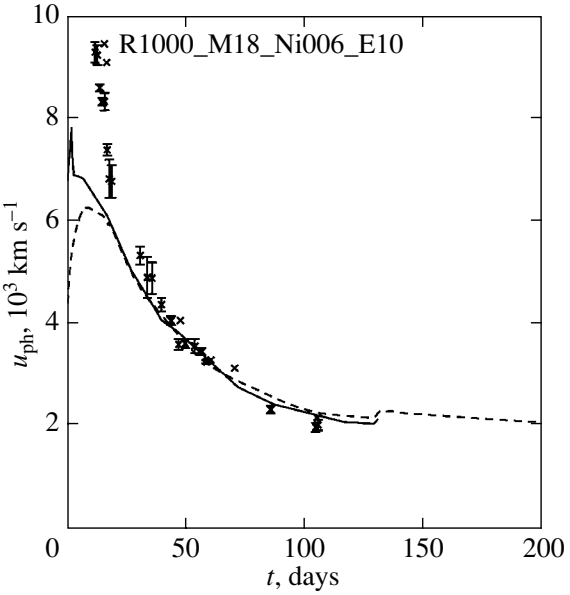

Fig. 12. Photospheric velocity for model No. 2. Time from the explosion is along the horizontal axis.

we obtained the R1000_M18_Ni006_E10 model (No. 2 in Table 2).

Before its explosion, the presupernova was a star with a mass of $18M_\odot$ and a radius of $1000R_\odot$. According to Woosley *et al.* (2002), a star with an initial mass between 15 and $25M_\odot$ at the core silicon burning stage (i.e., close to the presupernova) can have a radius between 800 and $1400R_\odot$. Hydrogen, helium, and elements heavier than He accounted for 70, 29.6, and only 0.4% of the envelope, respectively. The distribution of elements in the presupernova for model No. 2 is shown in Fig. 9. The density is plotted against the mass (the Lagrangian coordinate) in Fig. 10. The explosion was modeled by a release of energy $E = 10^{51}$ erg near the center.

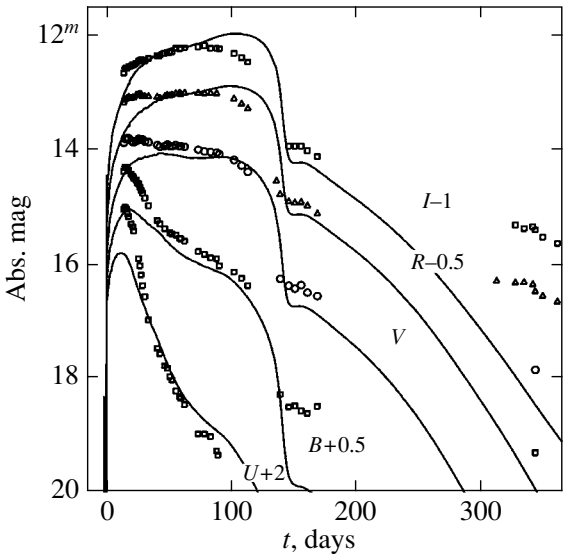

Fig. 13. U, B, V, R, I light curves of SN 1999em for model No. 2. Time from the explosion is along the horizontal axis.

The explosion began about 12 days before the SN was discovered on October 29, 1999; i.e., the SN explosion in this model occurred on October 17, 1999. We could shift the explosion onset back in time for better agreement between the V, R, I fluxes in the first 20 days if it were not for the following two restrictions: the observations of the galaxy NGC 1637 9 days before the explosion of SN 1999em (Leonard *et al.* 2001) and the measured photospheric velocities.

The U, B, V light curves (Fig. 11) and the photospheric velocity (Fig. 12) for this model are in slightly poorer agreement with the observational data than those for model No. 1. If, however, the model light curves and the observations in the U, B, V, R, I bands are superimposed on one another, then, globally, the light curves of model No. 2 (Fig. 13) pass more accurately through the observation points than those for model No. 1 (Fig. 5). However, model No. 1 seems preferred for the first 20 days, particularly from the $u_{\rm ph}$ observations (cf. Figs. 6 and 12). The better agreement for $u_{\rm ph}$ in the case of a shorter distance scale can be explained by a systematic error in the observed $u_{\rm ph}$. This error could lead to underestimation of the true EPM distance. At the same time, the short-wavelength spectra are also in better agreement with the observations for the short distance scale (Fig. 7). For the long distance scale, the theoretical spectra are found to be too soft (Figs. 14, 15), since the long distance scale corresponds to a larger presupernova radius, while the maximum achievable color temperature of the explosion produced by the outbreaking shock wave decreases at a larger radius. Thus, the larger spectral hardness argues for a shorter distance scale.

The appreciable deviation of the $UBVRI$ fluxes from their observed values in the first 20 days can be caused by the structural peculiarities of the outer atmospheric layers in the presupernova disregarded in our model. Note that, in general, the theoretical continuum spectra for the first days in Fig. 7 deviate from the observations less than, for example, the V fluxes, since the flux in this band is affected by spectral lines.

CONCLUSIONS

Our detailed calculations yielded presupernova parameters for SN 1999em that differ significantly from the results obtained by Nadyozhin (2003) and Hamuy (2003) using simple formulas from Litvina and Nadyozhin (1983, 1985). This suggests that, to determine the parameters of the SN IIP, we must model its light curves in all bands and the photospheric velocity by examining a large set of model supernovae and achieving the best agreement with the observations.

Taking the distance to SN 1999em estimated by the EPM to be $D = 7.5$ Mpc, we found reasonable parameters for the presupernova: radius $R = 450R_\odot$, mass $M = 15M_\odot$, and explosion energy $E = 7 \times 10^{50}$ erg. The UBV fluxes are in better agreement with the observations at a low metallicity of the presupernova, $Z = 0.004$. The values of R, M, and E for the presupernova must be increased for the distance $D = 12$ Mpc determined from Cepheids to the following values: $R = 1000R_\odot$, $M = 18M_\odot$ and $E = 10^{51}$ erg. Note that this behavior of M and E with increasing D differ qualitatively from that predicted by formulas (2) derived by Litvinova and Nadyozhin (1983, 1985).

For model No. 1, the U, B, V light curves and the photospheric velocity for $D = 7.5$ Mpc are in good agreement with the observations (Figs. 3, 6). In general, model No. 2 satisfactorily describes the entire range of the observations in five bands (Fig. 10) at $D = 12.38$ Mpc. The agreement of this model with the observations for the long distance scale in R and I is even better than that for model No. 1 for the short distance scale. At the same time, the poor agreement of the photospheric velocity with the U, B, V observations, particularly in the first 20 days, and the overly soft spectra in the first days for model No. 2 suggest that the distance $D = 7.5$ Mpc to SN 1999em is more realistic than $D = 12$ Mpc. This conclusion cannot be final until the light curves of this SN and its spectra are modeled in detail by taking into account factors that have not yet been included in our analysis: the

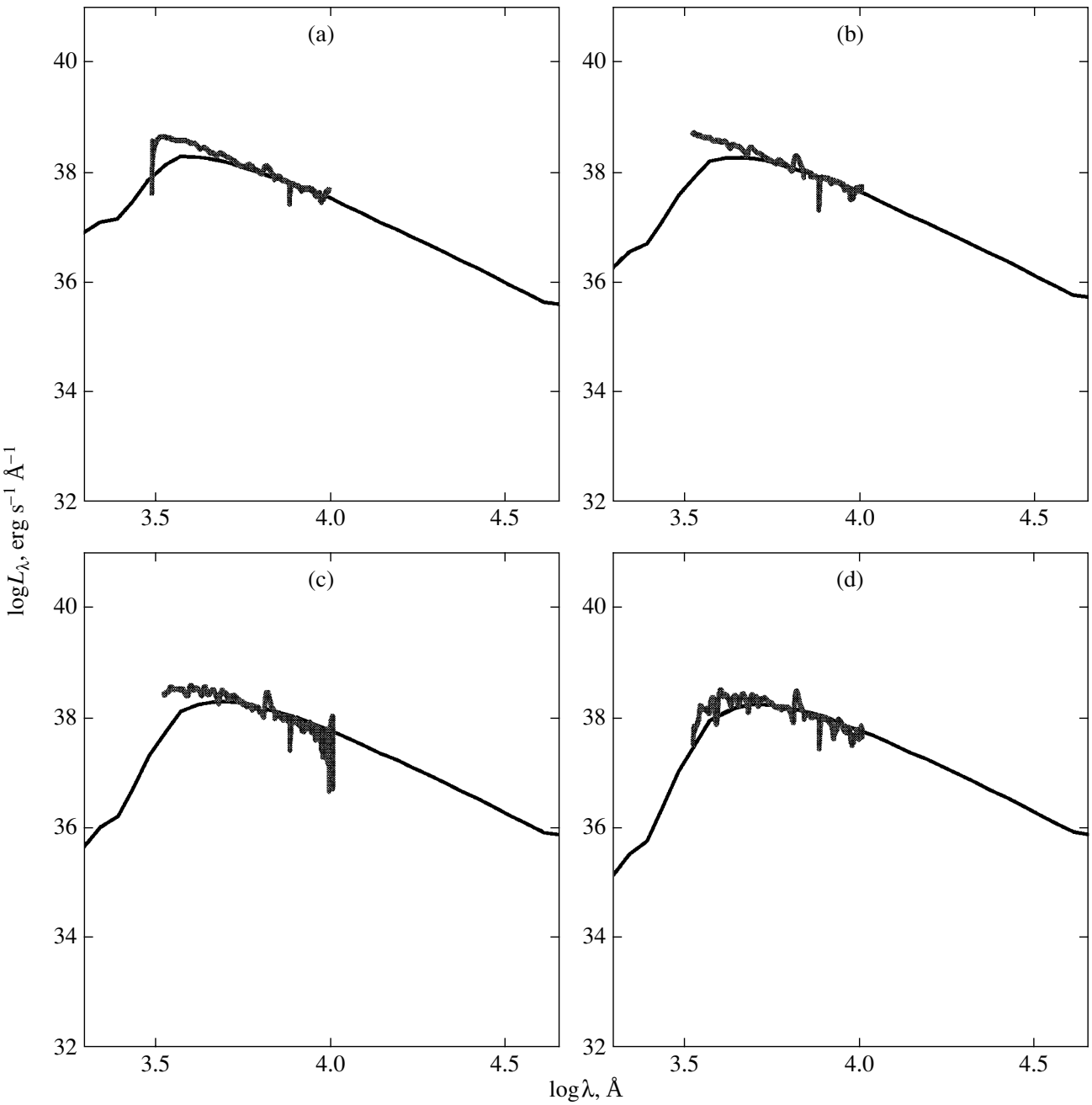

Fig. 14. Spectra for (a) October 30, 1999, (b) November 3, 1999, (c) November 9, 1999, (d) November 14, 1999, for model No. 2.

structural features of the outer layers, the nonsphericity, and the departure from local thermodynamic equilibrium. The value of $D = 8.9$ Mpc (Tully 1988) is also closer to our preferred case.

Our modeling showed that SN 1999em reached the homologous expansion stage not earlier than 15 days after its explosion. Consequently, we can estimate $u_{\rm ph}$ for this SN as $R_{\rm ph}/t$ and, accordingly, use the EPM only from this time. Hamuy *et al.* (2001) and Leonard *et al.* (2001) also used earlier points. The same remark also applies to the paper by Baron *et al.* (2004), who used the SEAM. Thus, a correction must be applied to the results for the distance D obtained by Hamuy *et al.* (2001), Leonard *et al.* (2001), and Baron *et al.* (2004) by discarding the data for the first two weeks.

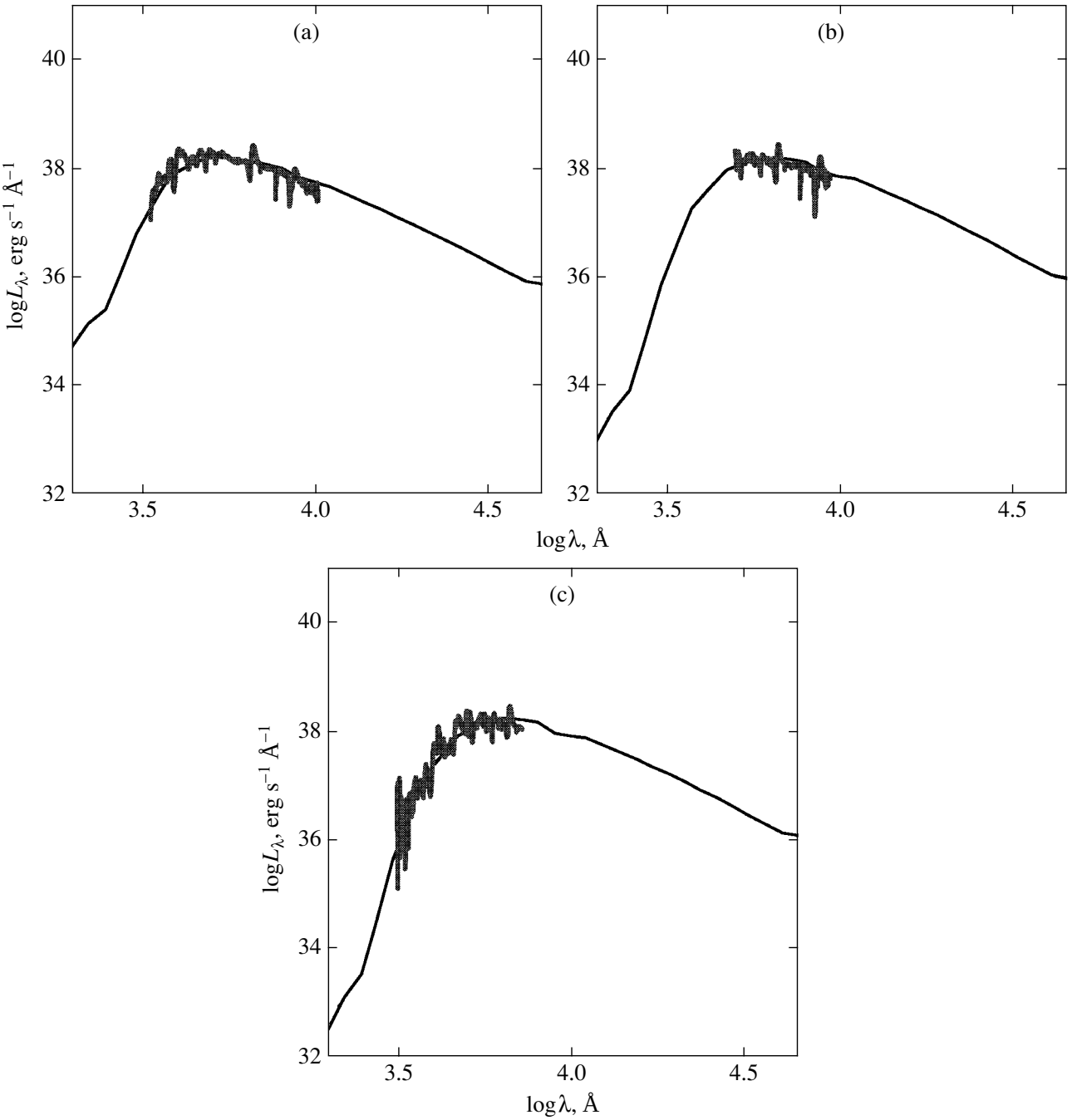

Fig. 15. Spectra for (a) November 19, 1999, (b) December 16, 1999, and (c) December 31, 1999, for model No. 2.

ACKNOWLEDGMENTS

We thank D.K. Nadyozhin, M. Hamuy, R. Hirschi, and Ph. Podsiadlowski for their helpful discussions. This work was supported by the Russian Foundation for Basic Research (project No. 02-02-16500a and No. 04-02-16793a), NSF AST-02-06111, and NASA NAG5-12D36. We are also grateful to W. Hillebrandt for support at the Max Planck Institute for Astrophysics (MPA, Garching, Germany). S.I. Blinnikov thanks INT (University of Washington program INT-04-2) and S. Woosley for their support.

REFERENCES

1. E. Anders and N. Grevesse, Geochim. Cosmochim. Acta **53**, 197 (1989).
2. P. V. Baklanov, http://www.astronet.ru:8101/db/msg/1 174 722 (2002).
3. E. Baron, D. Branch, A. V. Filippenko, *et al.*, Astrophys. J. **545**, 444 (2000).
4. E. Baron, P. E. Nugent, D. Branch, *et al.*, Astrophys. J. **616**, 91 (2004).
5. M. Basco, Astrophys. J. **425**, 264 (1994).
6. S. I. Blinnikov and O. S. Bartunov, Astron. Astrophys. **273**, 106 (1993).
7. S. I. Blinnikov and E. I. Sorokina, Astrophys. Space Sci. **290**, 13 (2004).
8. S. I. Blinnikov, R. Eastman, O. S. Bartunov, *et al.*, Astrophys. J. **496**, 454 (1998).
9. N. N. Chugai, S. I. Blinnikov, R. J. Cumming, *et al.*, Mon. Not. R. Astron. Soc. **352**, 121 (2004).
10. A. Elmhamdi, I. J. Danziger, and N. Chugai, Mon. Not. R. Astron. Soc. **338**, 939 (2003a); astro-ph/0209623.
11. A. Elmhamdi, N. N. Chugai, and I. J. Danziger, Astron. Astrophys. **404**, 1077 (2003b); astro-ph/0304144.
12. M. Hamuy, http://csp1.lco.cl/mhamuy/SNe/spec/SN1999em/ (2000).
13. M. Hamuy, Astrophys. J. **582**, 905 (2003).
14. M. Hamuy, P. A. Pinto, and R. G. Eastman, Astrophys. J. **558**, 615 (2001).
15. V. S. Imshennik and D. K. Nadyozhin, Itogi Nauki Tekh., Ser.: Astron. **21**, 63 (1982).
16. C. K. Lacey, R. A. Sramek, S. D. Van Dyk, *et al.*, IAU Circ., No. 7318 (1999a).
17. C. K. Lacey, R. A. Sramek, S. D. Van Dyk, *et al.*, IAU Circ., No. 7336 (1999b).
18. D. C. Leonard, A. V. Filippenko, E. L. Gates, *et al.*, astro-ph/0109535 (2001).
19. D. C. Leonard, S. M. Kanbur, C. C. Ngeow, *et al.*, Astrophys. J. **594**, 247 (2003).
20. I. Y. Litvinova and D. K. Nadyozhin, Astrophys. Space Sci. **89**, 89 (1983).
21. I. Y. Litvinova and D. K. Nadyozhin, Pis'ma Astron. Zh. **11**, 351 (1985) [Sov. Astron. Lett. **11**, 145 (1985)].
22. W. J. Maciel and R. D. D. Costa, IAU Symp. **209**, 551 (2003).
23. D. K. Nadyozhin, Mon. Not. R. Astron. Soc. **346**, 97 (2003).
24. A. Pastorello, M. Ramina, L. Zampieri, *et al.*, in *IAU Colloquium No. 192: Cosmic Explosions, On 10th Anniversary of SN 1993J, 2005*, p. 195.
25. L. S. Pilyugin, J. M. Vilchez, and T. Contini, Astron. Astrophys. **425**, 849 (2004).
26. D. V. Popov, Astrophys. J. **414**, 712 (1993).
27. Y. Sohn and T. J. Davidge, Astron. J. **115**, 130 (1998).
28. R. B. Tully, *Nearby Galaxies Catalog* (Cambridge Univ. Press, Cambridge, 1988).
29. S. E. Woosley, A. Heger, and T. A. Weaver, Rev. Mod. Phys. **74**, 1015 (2002).

Translated by V. Astakhov

Astronomy Letters, Vol. 31, No. 7, 2005, pp. 442–445. Translated from Pis'ma v Astronomicheskiĭ Zhurnal, Vol. 31, No. 7, 2005, pp. 496–499.

Influence of a Strong Magnetic Field on the Neutrino Heating of a Supernova Shock

A. A. Gvozdev* **and I. S. Ognev**

Yaroslavl State University, ul. Sovetskaya 14, Yaroslavl, 150000 Russia

Received January 17, 2005

Abstract—Based on the magnetorotational model of a supernova explosion with core collapse, we investigate the significant processes of neutrino heating of the supernova shock. These processes should be taken into account in self-consistent modeling, since the neutrino heating mechanism is capable of increasing the explosion efficiency. We show that, even in the presence of a strong magnetic field ($B \sim 10^{15}$ G) in the shock formation region, the heating rate is determined with good accuracy by the absorption and emission of neutrinos in direct URCA processes. Moreover, the influence on them of a magnetic field is reduced to insignificant corrections. © *2005 Pleiades Publishing, Inc.*

Key words: *supernovae, neutrino processes, magnetic field.*

Explosions of supernovae with core collapse are known to be generally accompanied by an intense outward ejection of part of the material. However, the currently existing models do not offen an efficient explosion mechanism. Thus, for example, in the standard spherically symmetric supernova explosion model, the shock stops on a scale on the order of a hundred kilometers from the center of the remnant. Attempts to improve this model by applying relativistic corrections and using a self-consistent description of neutrino propagation (based on the solution of the Boltzmann equation) do not lead to a significant modification of the explosion pattern (Liebendoerfer *et al.* 2001). The currently existing 2D calculations including the additional shock heating through convection and interaction with the neutrino flux do not lead to a successful supernova explosion either (Buras *et al.* 2003). On the other hand, the currently available observational data on several supernovae suggest that their explosions are asymmetric (Wheeler *et al.* 2002; Wang *et al.* 2001); moreover, this asymmetry can be fairly strong (Leonard *et al.* 2000). It would be natural to assume that this asymmetry is the result of the rapid rotation of the collapse remnant or the presence of a strong magnetic field. Note that, according to existing models, the generation of a magnetic field in the remnant is directly related to its rapid rotation.

At present, the best-known supernova explosion model with a self-consistent allowance for the magnetic field is the so-called magnetorotational model by Bisnovatyi-Kogan (1970). The presence of a primary magnetic field and an angular velocity gradient in this model leads to the linear growth of a secondary magnetic field with time to a certain critical value. Once the latter has been reached, an axially symmetric (relative to the equatorial plane) supernova explosion occurs. However, as recent calculations by Ardeljan *et al.* (2004) showed, the linear growth of the magnetic field is disrupted by the development of magnetorotational instability. The development of this instability leads to a rapid growth of magnetic field perturbations to strengths $B \sim 10^{15}$–10^{16} G, and to the formation of a shock.

As the magnetorotational instability develops, the kinetic energy of the rotation of the envelope with an angular velocity gradient transforms into the kinetic energy of the outward ejection of material through the rapidly growing magnetic field perturbations (Balbus and Hawley 1991, 1998). However, another additional energy source, shock heating by a neutrino flux, has long been known (Bethe and Wilson 1985). In the model under consideration, the neutrino heating mechanism is capable of increasing the explosion efficiency and is of particular interest.

The direct URCA processes

$$\nu_e + n \to p + e^-, \tag{1}$$

$$\tilde{\nu}_e + p \to n + e^+, \tag{2}$$

are generally believed to be the dominant neutrino shock heating reactions. Another popular neutrino–lepton process,

*E-mail: gvozdev@univ.uniyar.ac.ru

$$\nu_i + \tilde{\nu}_i \to e^+ + e^-, \quad i = e, \mu, \tau \tag{3}$$

is inefficient far from the center, because the angle between the neutrino and antineutrino momenta is small. Note that in a medium with a strong magnetic field, the production processes of an e^+e^- pair by a single neutrino,

$$\nu_i \to \nu_i + e^+ + e^-, \tag{4}$$

$$\tilde{\nu}_i \to \tilde{\nu}_i + e^+ + e^-, \quad i = e, \mu, \tau \tag{5}$$

open up kinematically and can be important. In this paper, we compare the neutrino shock heating efficiencies in the presence of a strong magnetic field in the standard direct URCA processes and reactions (4)–(5).

The neutrino heating rate per nucleon in the direct URCA processes (1)–(2) can be calculated as

$$Q_0^{\nu,\tilde{\nu}} = \frac{1}{N_{\rm N}} \int \omega K_{\nu,\tilde{\nu}} f_{\nu,\tilde{\nu}}(\omega, \mathbf{r}) \frac{d^3k}{(2\pi)^3}, \tag{6}$$

where $k_\alpha = (\omega, \mathbf{k})$ is the 4-momentum of the (anti)neutrinos, $f_{\nu,\tilde{\nu}}(\omega, \mathbf{r})$ is their local distribution function, $N_{\rm N}$ is the local nucleon number density, and $K_{\nu,\tilde{\nu}}$ is the absorption coefficient defined as the rate of reactions (1)–(2) underintegrated over the neutrinos. In what follows, we use the natural system of units with $c = \hbar = k = 1$.

In the case of a moderate magnetic field where the e^+e^- plasma occupies many Landau levels ($\langle \omega_{\nu_e}^2 \rangle \gtrsim 2eB$), its influence on the direct URCA processes is rather weak. For the absorption coefficient, we can in this case use its field-free expression. Assuming that the e^+e^- plasma is ultrarelativistic and that the nonrelativistic nucleons have a Boltzmann distribution, we can represent the absorption coefficient as

$$K_{\nu,\tilde{\nu}} = \frac{G^2}{\pi}(1 + 3g_a^2) Y_{n,p} N_{\rm N} \times \frac{\omega^2}{1 + \exp[(-\omega \pm \mu_e)/T]}. \tag{7}$$

Here, $G = G_{\rm F} \cos\theta_{\rm c}$, where $G_{\rm F}$ is the Fermi constant, $\theta_{\rm c}$ is the Cabibbo angle, $g_{\rm a} \simeq 1.26$ is the axial constant of the charged nucleon current, $Y_n = N_n/N_{\rm N}$, $Y_p = 1 - Y_n$, $N_{\rm N} = N_n + N_p$, where N_n and N_p are the local neutron and proton number densities, respectively, μ_e is the chemical potential of the electrons, and T is the local temperature.

It is convenient to while formula (6) for the heating rate of the medium in the direct URCA processes in terms of the mean quantities of neutrino radiation

$$\langle \omega_{\nu_e}^n \rangle = \left(\int \omega^{n+1} f_{\nu_e}(\omega, \mathbf{r}) \frac{d^3k}{(2\pi)^3} \right) \times \left(\int \omega f_{\nu_e}(\omega, \mathbf{r}) \frac{d^3k}{(2\pi)^3} \right)^{-1}, \tag{8}$$

$$\langle \chi_{\nu_e} \rangle = \left(\int \chi\omega f_{\nu_e}(\omega, \mathbf{r}) \frac{d^3k}{(2\pi)^3} \right) \times \left(\int \omega f_{\nu_e}(\omega, \mathbf{r}) \frac{d^3k}{(2\pi)^3} \right)^{-1}, \tag{9}$$

where χ is the cosine of the angle between the neutrino momentum and the radial direction and the total neutrino luminosity

$$L_{\nu_e} = 4\pi r^2 \int \chi\omega f_{\nu_e}(\omega, \mathbf{r}) \frac{d^3k}{(2\pi)^3}. \tag{10}$$

Here, r is the distance from the center of the remnant to a given point.

Under the additional simplifying assumption

$$\langle \omega_{\nu_e}^2 \rangle L_{\nu_e} / \langle \chi_{\nu_e} \rangle = \langle \omega_{\tilde{\nu}_e}^2 \rangle L_{\tilde{\nu}_e} / \langle \chi_{\tilde{\nu}_e} \rangle,$$

which holds in various supernova explosion models, we obtain a well-known (see, e.g., Janka 2001) expression for the shock heating rate in the direct URCA processes:

$$Q_0 = Q_0^\nu + Q_0^{\tilde{\nu}} = \frac{G^2}{\pi}(1 + 3g_a^2) \frac{L_{\nu_e} \langle \omega_{\nu_e}^2 \rangle}{4\pi r^2 \langle \chi_{\nu_e} \rangle} \simeq 55 \left(\frac{\rm MeV}{\rm nucleon\ s} \right) \left(\frac{L_{\nu_e}}{10^{52}\ {\rm erg/s}} \right) \times \left(\frac{\langle \omega_{\nu_e}^2 \rangle}{225\ {\rm MeV}^2} \right) \left(\frac{10^7\ {\rm cm}}{r} \right)^2, \tag{11}$$

where r is the characteristic distance to the shock.

The heating rate of the medium per nucleon in the additional processes (4)–(5) can be calculated as

$$Q_B^{\nu_i,\tilde{\nu}_i} = \frac{1}{N_N} \int E_{\nu_i,\tilde{\nu}_i} f_{\nu_i,\tilde{\nu}_i}(\omega, \mathbf{r}) \frac{d^3k}{(2\pi)^3}, \tag{12}$$

where $E_{\nu_i,\tilde{\nu}_i}$ is the heating rate of the medium per (anti)neutrino of type i. In the case of a moderate magnetic field where $\langle \omega_{\nu_e}^2 \rangle \gtrsim 2eB$, it can be represented in a logarithmic approximation (Kuznetsov and Mikheev 1997) as

$$E_{\nu_i,\tilde{\nu}_i} \simeq \frac{7G_F^2(c_{v_i}^2 + c_{a_i}^2)}{432\pi^3}(eB\omega\sin\varphi)^2 \times \ln\left(\frac{eB\omega\sin\varphi}{m_e^3}\right). \quad (13)$$

Here, φ is the angle between the momentum of the initial neutrino and the magnetic field, c_{v_i} and c_{a_i} are the vector and axial constants of the weak electron current ($c_{v_e} \simeq 0.96$, $c_{a_e} = 1/2$ for the electron neutrino; $c_{v_i} \simeq -0.04$, $c_{a_i} = -1/2$ for the μ- and τ-neutrino).

Formula (12) for the neutrino heating rate of the medium in processes (4)–(5) can also be expressed in terms of the mean quantities of neutrino radiation and its total luminosity:

$$Q_B^i = Q_B^{\nu_i} + Q_B^{\tilde{\nu}_i} = \frac{7G_F^2(c_{v_i}^2 + c_{a_i}^2)}{216\pi^3} \times \frac{(eB)^2\langle\omega_{\nu_i}\rangle}{N_N}\frac{L_{\nu_i}}{4\pi r^2\langle\chi_{\nu_i}\rangle}. \quad (14)$$

When deriving this formula, we assumed that $\sin\varphi \sim 1$, which holds good for the region where the neutrinos propagate almost freely. Under the additional simplifying assumption

$$\langle\omega_{\nu_i}\rangle L_{\nu_i}/\langle\chi_{\nu_i}\rangle = \langle\omega_{\tilde{\nu}_i}\rangle L_{\tilde{\nu}_i}/\langle\chi_{\tilde{\nu}_i}\rangle = \langle\omega_{\nu_e}\rangle L_{\nu_e}/\langle\chi_{\nu_e}\rangle,$$

which holds good in various supernova explosion models, we obtained the following expression for the ratio of the total neutrino heating rates in processes (4)–(5) and (1)–(2):

$$\frac{Q_B}{Q_0} \simeq 1.6\times10^{-2}\frac{(eB)^2\langle\omega_{\nu_e}\rangle}{N_{\rm N}\langle\omega_{\nu_e}^2\rangle} \simeq \frac{15\ {\rm MeV}}{\langle\omega_{\nu_e}\rangle}\frac{(eB)^2}{\rho}, \quad (15)$$

where $Q_B = \sum_i Q_B^i$ is the total neutrino heating rate for all types of neutrinos.

In this paper, we considered the most significant neutrino shock heating processes in the magnetorotational model. For the sake of generality, we derived the well-known expression for the heating rate in the URCA processes (11). Note that even this expression contains a number of simplifying assumptions discussed in the paper. In addition, the density of the medium decreases with distance much more slowly in the magnetorotational model than in the spherically symmetric model. This implies that, even at the characteristic distances where the shock is formed ($r \sim 100$ km), we must also take into account the neutrino radiation processes, which can significantly reduce the total rate of neutrino shock heating. Thus, formula (11) should be treated with caution, particularly in the magnetorotational model.

On the other hand, in the magnetorotational model, a fairly strong magnetic field ($B \sim 10^{15}$ G) can be generated at large distances ($r \sim 100$ km). Therefore, we must consider the effect of such a strong magnetic field on the neutrino shock heating. In particular, under these conditions, the new neutrino heating reactions (4)–(5) can compete with the direct URCA processes (1)–(2), which are the main processes in the spherically symmetric explosion model.

Our estimate (15) shows that the new neutrino heating reactions (4)–(5) become significant when $(eB)^2 \gtrsim \rho$. However, the strength of the magnetic field produced by the medium cannot be too large. For example, in the models with sub-Keplerian rotation rates (Akiyama *et al.* 2003; Thompson *et al.* 2004), the magnetic field strength reaches saturation when the field energy density becomes comparable to the rotation energy density of the medium, $B_{\rm sat}^2 \simeq 4\pi\rho(r\Omega)^2$ (where Ω is the local angular velocity of the medium at distance r). Using this estimate, we can present the ratio of the heating rates (15) as

$$\frac{Q_B}{Q_0} \lesssim 0.1\left(\frac{r\Omega}{c}\right)^2\frac{15\ {\rm MeV}}{\langle\omega_{\nu_e}\rangle} \ll 1, \quad (16)$$

where c is the speed of light in a vacuum. Thus, in all probability, the new reactions that open up in a magnetic field cannot compete with the standard neutrino shock heating processes. Consequently, even in the case of a fairly strong magnetic field, $B \sim 10^{15}$ G, the heating is almost completely determined by the absorption and emission of neutrinos in the direct URCA processes, with the influence of the magnetic field on them being reduced to insignificant corrections.

ACKNOWLEDGMENTS

We are grateful to N.V. Mikheev, G.S. Bisnovatyi-Kogan, and S.G. Moiseenko for their discussions and advice on the fundamental points of this work. This work was supported in part by the RF Presidential Council for Grants for the Support of Young Russian Scientists and the Leading Scientific Schools of the Russian Federation (grant no. NSh-1916.2003.2), the Russian Foundation for Basic Research (project no. 04-02-16253), and the RF Ministry (project no. E02-11.0-48).

REFERENCES

1. S. Akiyama, J. C. Wheeler, D. L. Meier, and I. Lichtenstadt, Astrophys. J. **584**, 954 (2003).
2. N. V. Ardeljan, G. S. Bisnovatyi-Kogan, and S. G. Moiseenko, astro-ph/0410234 (2004).

3. S. A. Balbus and J. F. Hawley, Astrophys. J. **376**, 214 (1991).
4. S. A. Balbus and J. F. Hawley, Rev. Mod. Phys. **70**, 1 (1998).
5. H. A. Bethe and J. R. Wilson, Astrophys. J. **295**, 14 (1985).
6. G. S. Bisnovatyi-Kogan, Astron. Zh. **47**, 813 (1970) [Sov. Astron. **14**, 652 (1970)].
7. R. Buras, M. Rampp, H. T. Janka, and K. Kifonidis, Phys. Rev. Lett. **90**, 241101 (2003).
8. H.-Th. Janka, Astron. Astrophys. **368**, 527 (2001).
9. A. V. Kuznetsov and N. V. Mikheev, Yad. Fiz. **60**, 2038 (1997) [Phys. At. Nucl. **60**, 1865 (1997)].
10. D. C. Leonard, A. V. Filippenko, A. J. Barth, and T. Matheson, Astrophys. J. **536**, 239 (2000).
11. M. Liebendoerfer, O. E. B. Messer, A. Mezzacappa, and W. R. Hix, astro-ph/0103024 (2001).
12. T. A. Thompson, E. Quataert, and A. Burrows, astro-ph/0403224 (2004).
13. L. Wang, D. A. Howell, P. Hoeflich, and J. C. Wheeler, Astrophys. J. **550**, 1030 (2001).
14. J. C. Wheeler, D. L. Meier, and J. R. Wilson, Astrophys. J. **568**, 807 (2002).

Translated by G. Rudnitskiĭ

Astronomy Letters, Vol. 31, No. 7, 2005, pp. 446–451. Translated from Pis'ma v Astronomicheskiĭ Zhurnal, Vol. 31, No. 7, 2005, pp. 500–505.

Phenomenological Explanation for the Shape of the Spectrum of Cosmic Rays with Energies $E > 10$ GeV

G. S. Golitsyn*

Obukhov Institute of Atmospheric Physics, Russian Academy of Sciences, Pyzhevskiĭ per. 3, Moscow, 109017 Russia

Received February 20, 2003

Abstract—Assuming that the energy gain by cosmic-ray (CR) particles is a stochastic process with stationary increments, we derive expressions for the shape of their energy spectrum up to energies $E \sim 10^{18}$ eV. In the ultrarelativistic case under study, the energy is proportional to the momentum, whose time derivative is the force. According to the Fermi mechanism, a particle accelerates when it passes through a system of shock waves produced by supernova explosions. Since these random forces act on time scales much shorter than the particle lifetime, we assume them to be delta-correlated in time. In this case, due to the linear energy–momentum relationship, the mean square of the energy (increments) is proportional to the differential scale $\tau(E) \sim E\tau(\geq E)$, where $\tau(\geq E)$ is the cumulative time it takes for a particle to gain an energy $\geq E$. The probability of finding a particle with energy $\geq E$ somewhere in the system is inversely proportional to the time it takes to gain the energy E. To estimate an upper limit for the space number density of CR particles, we use estimates of the CR volume energy density, a quantity known for our Galaxy. It is taken to be constant in the range $10\,\text{GeV} \leq E \leq 3 \times 10^6$ GeV, where the index of the energy spectrum was found to be $-8/3 \approx -2.67$ against its empirical value of -2.7. In the range $3 \times 10^6\,\text{GeV} \leq E < 10^9$ GeV, the upper limit for the volume energy density is estimated by using the results from the previous range to be $-28/9 \approx -3.11$ against its empirical value of -3.1. The numerical coefficients in the suggested shapes of the spectrum can be determined by comparison with observational data. Thus, the CR energy spectrum is the result of the random walks of ultrarelativistic particles in energy/momentum space caused by the Fermi mechanism. © *2005 Pleiades Publishing, Inc.*

Key words: *cosmic rays, nonthermal radiation processes.*

INTRODUCTION

The cosmic-ray (CR) energy spectrum at energies $E > 10^{10}$ eV $= 10$ GeV has three power-law portions with different indices n. No explanation has been found for these values of n for three decades. Clearly, different particle acceleration (and destruction) mechanisms operate over a range of energies E spanning about ten orders of magnitude. These processes are associated mainly with supernova (SN) explosions and, for energies of $\sim 10^{18}$ eV or more, with processes in quasars and/or clusters of galaxies (see Ginsburg (1969), from where we took the main numerical values).

The latest models for the origin of the shape of the CR spectrum can be found in the reviews by Hoerandel (2004) and Erlykin (2004). The models include various hypotheses and constants; the reliability of the former and the estimates of the latter have always been open to question. At the same time, the retention of the spectral shape over several orders of magnitude implies that some simple statistical mechanisms leading to self-similar spectral shapes are operating. Here, we show that in its simplest interpretation, the statistical mechanism of CR acceleration by SN shock waves in the interstellar medium suggested by Fermi (1949) is one of the mechanisms in the evolution of systems in which random forces act with a correlation time much shorter than the lifetime of the system itself, or even shorter than the interval between two successive encounters of CR particles with shock waves.

Leontovich (1935) showed that the Boltzmann kinetic equation could be derived by assuming that the collisions between molecules form a Markovian chain. The latter is equivalent to assuming a short correlation time, namely, a delta correlation in time, compared to the system's response time. Leontovich (1983) used a similar assumption to derive a functional equation for the mean square of the displacement of a Brownian particle. The solution of this equation is proportional to the time, i.e., equivalent to

*E-mail: mail_adm@ifaran.ru

1063-7737/05/3107-0446$26.00

formula (9) derived below for the diffusion or random walks of CR particles in momentum space.

Below, we provide the basic information needed below about CRs and our Galaxy. The Galactic disk has a thickness on the order of $h = 200$ pc and a radius of 15 kpc (1 pc $= 3 \times 10^{16}$ m). Thus, the volume of the Galaxy is 10^{61} m$^3 = 10^{67}$ cm^3 (without the halo). The CR volume energy density is $w_0 \sim 0.5$ eV cm$^{-3} \approx 10^{-13}$ J m^{-3}, 1 eV $= 1.6 \times 10^{-12}$ erg $= 1.6 \times 10^{-19}$ J. Thus, the total CR energy is $\sim W \approx 10^{48}$ J. The rate of energy release from SNe exploding two or three times in a century is $G \approx 3 \times 10^{33}$ W at an explosion energy of 10^{42}–10^{43} J. These values yield a CR lifetime of $\tau_e = W/G = 3 \times 10^{14}$ s $= 10^7$ yr. Thus, about $\sim 10^3$ CR generations have changed over the lifetime of our Galaxy, $\sim 10^{10}$ yr. The time τ_e is approximately four orders of magnitude longer than the time it takes for a particle moving at the speed of light c (1 pc = 3.26 light years) to cross the disk thickness. Particles do not escape from the Galaxy, as it possesses a magnetic field $H \approx 5 \times 10^{-6}$ G whose volume energy density $H^2/8\pi$ is almost equal to the CR energy density. In the ultrarelativistic approximation, the particle energy is

$$E = pc, \tag{1}$$

where p is the momentum, and c is the speed of light (recall that the intrinsic energy of the proton is close to 1 GeV, whereas our particles have energies $E > 10$ GeV). The Larmor radius of the proton is given by the formula

$$R_{\rm L} = E_{18}/H_{-6}\ \text{kpc}, \tag{2}$$

where the energy, the magnetic field, and the radius are measured in 10^{18} eV, 10^{-6} G, and kpc, respectively. For this energy and a magnetic field of 5×10^{-6} G, we obtain $R_{\rm L} = 1/5 = 0.2$ kpc $=$ 200 pc, i.e., the thickness of the Galactic disk. The knee (steepening) in the spectrum is observed at $E \approx 3 \times 10^{15}$ eV $= 3 \times 10^{-3} E_{18}$, where $R_{\rm L} = 0.6 \times 10^{-3}$ kpc $= 0.6$ pc, i.e., the dimensionless radius $R_{\rm L}/h \sim 3 \times 10^{-3}$. The CR escape from the Galaxy probably becomes noticeable, starting from the $R_{\rm L}$ that is a factor of 300 smaller than the disk thickness.

The book by Ginzburg (1969) cited above gives the shapes of the cumulative CR energy spectra obtained from observational data:

$$I(\geq E) \tag{3}$$
$$= \begin{cases} 1 \times [E(\text{GeV})]^{-1.7}, \\ 10\ \text{GeV} \leq E \leq 3 \times 10^6\ \text{GeV} \\ 3 \times 10^{-10}[10^{-6}E(\text{GeV})]^{-2.1}, \\ 3 \times 10^6\ \text{GeV} \leq E \leq 10^9\ \text{GeV} = 10^{18}\ \text{eV}. \end{cases}$$

The quantity on the left means the number of particles with the threshold energy E per nucleon per unit area (1 cm^2) per unit time (1 s) arriving from a unit solid angle. The cumulative spectrum $I(\geq E)$ is related to the differential spectrum $I(E)$ by

$$I(\geq E) = \int_E^\infty I(E)dE. \tag{4}$$

Thus, the differential spectrum $I(E)$, the number of particles in the energy interval $[E, E + dE]$, is

$$I(E) = -\frac{d}{dE} I(\geq E). \tag{5}$$

The two spectra are related to the CR particle energy distribution function

$$n(\geq E) = \int_E^\infty n(E)dE \tag{6}$$
$$= \frac{4\pi}{c} \int_E^\infty I(E)dE = \frac{4\pi}{c} I(\geq E).$$

Above $E \sim 10^{18}$ eV, the spectrum again flattens out, although the statistical scatter of its values increases. The detection of CRs with energies above 10^{20} eV when the Greisen–Zatsepin–Kuzmin effect (the production of π mesons during the interaction of CRs with cosmic microwave background photons) comes into play is still a great puzzle.

DERIVATION OF THE FORMULA FOR THE FIRST PORTION OF THE SPECTRUM

We assume that the observed CRs (at least those with energies below the knee) are produced in the Galaxy, i.e., their spectrum is formed as they are accelerated by the shock waves (SWs) that the particles encounter, on average, two or three times in a century or more frequently, depending on the SW lifetime and their location in space. The forces $f(x_i, t)$ that produce stochastic acceleration are assumed to act on time scales much shorter than the CR lifetime and even the time intervals between successive SWs, which are randomly distributed in space and in time and generate random fields that are spatially uniform

and stationary in time. These forces can then be assumed to be delta-correlated:

$$B_f(\tau) = \sigma_f^2 \tau_0 \delta(\tau) \equiv G_p \delta(\tau), \quad G_p = \sigma_f^2 \tau_0, \quad (7)$$

where σ_f^2 is the variance of the random forces, and τ_0 is the correlation time of the random forces in a single Fermi-type acceleration event during the interaction with a shock wave. The frequency spectrum corresponding to the correlation function (7) is white noise with an energy density $G_p = \text{const}$.

The momentum is the time integral of the force, since

$$dp/dt = f. \quad (8)$$

The field of the forces for the correlation function (7) is statistically stationary in time; the momentum variation is then a stochastic process with stationary increments of the first order. It is characterized by the structure function calculated by integrating (8):

$$D_p(\tau) = \langle [p(t+\tau) - p(t)]^2 \rangle = 2G_p \tau. \quad (9)$$

This formula can be interpreted as the CR diffusion in momentum space in view of its clear analogy with the diffusion of a Brownian particle in coordinate space, for which the linear time dependence of the mean square of the displacement arises from the delta correlation between the momenta transferred to the Brownian particle. In our case, however, the forces that are the derivatives of the momenta are delta-correlated; therefore, the diffusion takes place in momentum space (see Golitsyn (2004), where we showed how one assumption could explain numerous statistical distributions in nature). In view of formula (1), we have the diffusion in energy space.

Here, there is a close analogy with the Kolmogorov turbulence of liquid Langrange particles (LLPs). Yaglom (1949) established that, in the inertial range of turbulence, the frequency spectrum of the LLP acceleration field is white noise with an energy density ε, the generation/dissipation rate of kinetic energy per unit mass. The time correlation function is

$$B_a(\tau) = \sigma_a^2 \tau_v \delta(\tau) = \varepsilon \delta(\tau),$$

where $\sigma_a^2 = \varepsilon^{3/2} \nu^{-1/2}$ is the mean square of the acceleration fluctuations, $\tau_v = (\nu/\varepsilon)^{1/2}$ is the Kolmogorov time microscale, and ν is the kinematic viscosity. The time structure function of the velocity $u(\tau)$ is

$$D_u(\tau) = \langle [u(t+\tau) - u(t)]^2 \rangle = 2\varepsilon\tau. \quad (10)$$

This formula was known to A. M. Obukhov in 1941. In explicit form (without the coefficient 2), it was first published in the first edition of the book by Landau and Lifshitz (1944), where it was derived from dimension considerations. Subsequently, Obukhov (1959) called ε in formula (10) the diffusion coefficient in velocity space (for a detailed history and a more rigorous discussion, see Monin and Yaglom (1975) and Obukhov and Yaglom (1951)). A paper by Novikov (1963), who derived formulas of type (10) using the Langevin equation with random forces in the limit of short correlation times, should also be mentioned. Previously (Golitsyn 2001a, 2001b, 2003), we showed how the Kolmogorov–Obukhov results for turbulence in the inertial range follow from this.

Recalling that, in the ultrarelativistic case, the energy is related to the momentum by the linear relation (1), we can rewrite formula (9) as

$$D_E(\tau) = \langle [E(t+\tau) - E(t)]^2 \rangle = c^2 G_p \tau. \quad (11)$$

Considering fairly long times τ, such that the initial energy can be ignored, we rewrite formula (11) as

$$E^2(\tau) \approx c^2 G_p \tau(\geq E) \quad (12)$$
$$= \frac{d}{dt}\left(\frac{E^2}{2}\right)\tau(\geq E) = \left(E\frac{dE}{dt}\right)\tau(\geq E),$$

where we removed the averaging symbol and where only the cumulative waiting time $\tau(\geq E)$ has the dimension of time. Hence,

$$E(\tau) \approx G\tau(\geq E), \quad E(\tau) \approx G\tau(\geq E), \quad (13)$$

where $G = dE/dt$ is the generation rate of CR energy in the Galaxy, which was estimated above to be 3×10^{33} W. Previously (Golitsyn 1997), we derived this relation from dimension considerations.

The relation between the cumulative time it takes to gain an energy $\geq E$ and the differential parameter $\tau(E)$ follows from equality

$$\frac{1}{\tau(\geq E)} = \int_E^\infty \frac{dE_i}{\tau(E_i)}. \quad (14)$$

In fact, this relationship between the frequencies follows from the relation between the cumulative probability and the probability density function (not normalized to any long time interval). The latter has a dimension that are the inverse of its parameter. It follows from formula (14) that the dimensions of $[\tau(\geq E)] = [\tau(E)][E]^{-1}$ and

$$\frac{1}{\tau(\geq E)} \approx \frac{E}{\tau(E)} \quad (15)$$

to within a numerical coefficient. This coefficient can be estimated by substituting $E_i = Ex$ in (14) and is

$$\int_1^\infty \frac{dx}{\tau(x)} = O(1)$$

for all moderately slowly decreasing functions $[\tau(x)]^{-1}$ that ensure the convergence of this integral. Below, we determine the numerical coefficients that establish the correspondence between the formulas derived in this paper and the empirical relations (3) by comparing them with measurements. Thus, we obtain from (13)–(15)

$$\frac{1}{\tau(\geq E)} \approx \frac{G}{E}, \quad \frac{1}{\tau(E)} \approx \frac{G}{E^2}, \quad \tau(E) \approx E\tau(\geq E). \tag{16}$$

These three formulas can also be obtained from dimensional considerations, remembering that we do not claim to be deriving expressions with accurate numerical coefficients.

Formulas (13)–(16) estimate the frequencies in the entire system under study (i.e., in the Galaxy), while the CR measurements are made in an area that occupies a negligible fraction of the cross section of the Galaxy. Therefore, it is necessary to estimate the particle space number density as a function of their energy and, in addition, via measurable or known parameters. This can be done by estimating an upper limit by writing the following system of inequalities for the CR number density:

$$n(\geq E) = \int_E^\infty n(E)dE = \int_E^\infty \frac{E}{E} n(E)dE \tag{17}$$
$$< \frac{1}{E}\int_E^\infty En(E)dE = \frac{w(\geq E)}{E},$$

where $w(\geq E)$ is the volume energy density of CRs with energies higher than or equal to E. We will only reinforce inequality (17) if we substitute $w_0 \approx 0.5$ eV/cm^3 for $w(\geq E)$ on the right-hand side. This makes it possible to estimate an upper limit for the scale of the inverse area to which the CR flux must be referred via the CR energy

$$1/S(\geq E) = [n(\geq E)]^{2/3} < (w_0/E)^{2/3}. \tag{18}$$

Thus, we have the two main scales given by formulas (16) and (18) that determine the measured particle flux. These scales may be considered as the probabilities of finding CRs in space and in time. Assuming these probabilities to be independent, we multiply them to obtain the spectrum. The probabilities are normalized when we determine the numerical coefficients by comparison with observational data; this determines the phenomenology of our analysis of the problem. As a result, we obtain

$$I(E) \approx \frac{3}{5} c_1 G E^{-2} \left(\frac{w_0}{E}\right)^{2/3} = \frac{3}{5} c_1 G w_0^{2/3} E^{-8/3}. \tag{19}$$

The cumulative spectrum can be calculated by integrating the differential spectrum using formula (4):

$$I(\geq E) = c_1 G w_0^{2/3} E^{-5/3}. \tag{20}$$

A comparison of formulas (20) and (3) yields a value for c_1 that is close to 10^{-37} for the global energy generation rate $G = 3 \times 10^{33}$ W and the above value of $w_0 = 0.5$ eV cm^{-3}. Note that the index that we obtained in (19), $n = 8/3 \approx 2.67$, is remarkably close to its empirical value of 2.7. We disregarded this difference and determined c_1 from the midpoint of the interval of relations (3).

Note also that the measured indices n decrease slightly with increasing atomic weight of the CR particles, being 2.67 for helium and slightly less for iron (Ginzburg 1969). In our scheme, this corresponds to some "pinkness" of the spectrum of random forces, i.e., their slow increase toward the lower frequencies and the moderately fast decrease of their correlation function with time, suggesting a relationship to the large-scale structure of the Galaxy. This is a purely pro forma remark without any discussion of the possible physical causes for this effect.

Formula (20) for the cumulative spectrum was derived previously (Golitsyn 1997) from similarity and dimension considerations. In this paper, we show the statistical nature of the result obtained previously by considering the stochastic gain of energy by ultrarelativistic CRs under the action of random forces with a short correlation time, whose action is treated as a stationary random process. Since we do not go into the details of the mechanism and operate with the quantities that characterize the entire Galaxy, we can determine only the shape of the spectrum. It proves to be similar to the observed spectral shape, and the smallness of the numerical coefficient c_1 can be explained by our units of measurement and scales being tens of orders of magnitude smaller than the corresponding Galactic ones.

ESTIMATING THE SHAPE OF THE SPECTRUM IN THE ENERGY RANGE 3×10^6 GeV $< E < 10^9$ GeV

This part of the energy spectrum from the knee to the ankle begins definitively to feel the CR escape from the Galactic disk, since, as we showed above, the Larmor radius of a proton in the Galactic magnetic field at an upper limit of $E = 10^{18}$ eV is equal to the disk thickness; i.e., the magnetic field ceases to confine the particles. Nevertheless, the fate of the individual high-energy particles is still described by formula (13), because the destruction or escape of

particles does not affect the fate of the remaining particles, and the energy is still gained by them stochastically through diffusion or random walks in momentum/energy space in the ultrarelativistic case.

However, the escape of particles from the Galaxy and the shape of the spectrum itself change the number densities of high-energy CRs. In the previous section, we estimated an upper limit for their number density and the separation between them using the constant quantity w_0, the CR volume energy density, as an analog of their pressure. The quantity w_0 is formed mostly by particles with energies as high as several hundred GeV, while in the range of energies considered in this section, their values are higher at least by four orders of magnitude.

Here, we can again estimate an upper limit for $w(\geq E)$ using formulas (4) and (6) with (20), i.e., by extending the estimate of the CR number density as a function of the particle energy from the previous range of the energy spectrum to the spectrum after the knee:

$$w(\geq E) > En(\geq E) = \frac{4\pi}{c} c_1 \left(\frac{w_0}{E}\right)^{2/3} G. \quad (21)$$

This introduces an additional energy dependence of the CR number density. Expressing the area scale as $[E/w(\geq E)]^{2/3}$ and relating it to the differential time scale from formula (16), we obtain the following formula for the differential spectrum:

$$I(E) \approx \frac{9}{19} c_2 \frac{G}{E^2} \left(\frac{G}{cE}\right)^{2/3} \left(\frac{w_0}{E}\right)^{4/9} \quad (22)$$
$$= \frac{9}{19} c_2 c^{-2/3} G^{5/3} w_0^{4/9} E^{-28/9}.$$

Hence, we have for the cumulative spectrum

$$I(\geq E) \approx c_2 c^{-2/3} G^{5/3} w_0^{4/9} E^{-19/9}. \quad (23)$$

A comparison of the latter formula with the observational data (3) for the values of G and w_0 mentioned above yields $c_2 \approx 5 \times 10^{-37}$. Note that our index $28/9 = 3 + 1/9$ is close to its empirical value of 3.1.

If there were several intervals with different slopes of the CR energy spectrum, then relations of type (21) would always hold in them. We could then develop a procedure of successive approximations to estimate the area scales using each time the estimate from the previous spectral interval. It is reduced to repeatedly taking the power 2/3 of the ratio $(w_0/E) = [n(\geq E)]^{2/3}$. The final index n in the dependence of the spectrum on energy E for k intervals can be found as

$$\sum_{i=0}^{k} \left(\frac{2}{3}\right)^i = n_k,$$

where $i = 1$ corresponds to the shape of the spectrum in the initial interval, in which $I(\geq E) \propto E^{-5/3}$. In the limit $k \to \infty$, the dependence on w_0 vanishes, and the spectrum acquires the shape $I(\geq E) \simeq G^3 c^{-2} E^{-3}$, which is most likely unattainable in nature. If a third energy interval of Galactic CRs existed in the spectrum above $E = 10^9$ GeV, then one could expect its index to be

$$n_3 = 1 + \frac{2}{3} + \frac{4}{9} + \frac{8}{27} = \frac{65}{27} \approx 2.4.$$

Our procedure shows that the index in the energy spectrum is determined mainly by the stochastic CR acceleration mechanism, the diffusion in energy–momentum space in the ultrarelativistic case, while the spatial CR distribution affects the shape of the spectrum to a lesser degree.

Below, we make several remarks about the shape of the spectrum for energies $E > 10^{18}$ eV. Here, the statistics are not very numerous and the scatter is significant, but the spectrum clearly becomes less steep and similar in shape to the portion before the knee. Since the particles here are clearly extragalactic in origin, the parameters that determine the shape and magnitude of this spectrum must refer to clusters of galaxies, quasars, etc. (see, e.g., Ostrowski 2002; Carilli and Taylor 2002).

CONCLUSIONS

The CR energy spectrum is the result of a stochastic process with stationary increments, which arises from the stochastically stationary effects of random delta-correlated (in time) forces (white noise) on the CRs. This is the simplest mathematical representation of the Fermi mechanism, the acceleration of ultrarelativistic CR particles by random shock waves from supernova explosions. The CR spatial frequency (number density) as a function of their energy can be estimated using the known CR volume energy density and the system of inequalities. The calculated spectral indices agree well with their experimental values. The numerical coefficients can be found from comparing the indices with the measurements. The simplest analog of the methodology used here is a description of the statistical properties of the motion of Brownian particles, but here the energy is gained through the random walks of ultrarelativistic particles in energy–momentum space.

The same results, at least those concerning the first portion of the spectrum, can also be obtained using the methods of similarity and dimensional theory, which, however, do not reveal the statistical nature of the process.

ACKNOWLEDGMENTS

Parts of this work were reported during the period 1995–2004 at several seminars held in different countries. The questions and remarks of their participants contributed significantly to my comprehension of the problem of the CR spectrum and to a clearer presentation of the results. I am especially grateful to the three referees of this paper whose remarks led to a significant revision of the paper and to a more rigorous and consistent presentation of its results (without changing the final conclusions). I am very grateful to A.A. Vikhlinin, who provided me with the literature on magnetic fields and CR origins. M.A. Mal'kov gave specific advice on how to present the results described here in a way satisfactory for CR experts. This work was supported in part by a grant from the Presidium of the Russian Academy of Sciences (No. 11 Nonlinear Dynamics and Chaos).

REFERENCES

1. C. L. Carilli and G. B. Taylor, Annu. Rev. Astron. Astrophys. **40**, 303 (2002).
2. A. D. Erlykin, astro-ph/0411223.
3. E. Fermi, Phys. Rev. **75**, 1169 (1949).
4. G. S. Golitsyn, Pis'ma Astron. Zh. **23**, 149 (1997) [Astron. Lett. **23**, 127 (1997)].
5. G. S. Golitsyn, Izv. Ross. Akad. Nauk, Fiz. Atmos. Okeana **37**, 438 (2001a).
6. G. S. Golitsyn, Vychisl. Seĭsmol. **32**, 138 (2001b).
7. G. S. Golitsyn, *Nonlinear Waves* (Inst. Prikl. Fiz. Ross. Akad. Nauk, Nizh. Novgorod, 2003), p. 117 [in Russian].
8. G. S. Golitsyn, Dokl. Akad. Nauk **398**, 177 (2004) [Dokl. Phys. **49**, 501 (2004)].
9. J. E. Hoerandel, Astropart. Phys. **21**, 241 (2004).
10. L. D. Landau and E. M. Lifshitz, *Mechanics of Continuum Media* (Tekhniko-Teoreticheskaya Literatura, Moscow, 1944) [in Russian].
11. M. A. Leontovich, Zh. Éksp. Teor. Fiz. **5**, 211 (1935).
12. M. A. Leontovich, *An Introduction to Thermodynamics. Statistical Physics* (Nauka, Moscow, 1983) [in Russian].
13. A. S. Monin and A. M. Yaglom, *Statistical Fluid Mechanics* (MIT Press, Cambridge, 1975; Gidrometeoizdat, St. Petersburg, 1996).
14. E. A. Novikov, Zh. Éksp. Teor. Fiz. **44**, 2159 (1963) [Sov. Phys. JETP **17**, 1449 (1963)].
15. A. M. Obukhov, Adv. Geophys. **6**, 113 (1959).
16. A. M. Obukhov and A. M. Yaglom, Prikl. Mat. Mekh. **15**, 3 (1951).
17. M. Ostrowski, Astropart. Phys. **18**, 229 (2002).
18. *The Astrophysics of Cosmic Rays*, Ed. by V. L. Ginzburg (Israel Program for Scientific Translations, Jerusalem, 1969; Nauka, Moscow, 1990).
19. A. M. Yaglom, Dokl. Akad. Nauk SSSR **67**, 795 (1949).

Translated by A. Dambis

Astronomy Letters, Vol. 31, No. 7, 2005, pp. 452–457. Translated from Pis'ma v Astronomicheskiĭ Zhurnal, Vol. 31, No. 7, 2005, pp. 506–512.

Unusual Color Variability of Eruptive Stars

A. F. Pugach*

Main Astronomical Observatory, National Academy of Sciences of Ukraine, ul. Akademika Zabolotnogo 27, Kiev, 03680 Ukraine

Received December 24, 2004

Abstract—We substantiate the conclusion that the unusual color variability found previously in some eruptive stars is typical of a broad class of nonstationary objects, manifests itself over a wide temperature range (from B0 to K3), and can be regarded as a new type of stellar variability. © *2005 Pleiades Publishing, Inc.*

Key words: *stars—variable and peculiar.*

INTRODUCTION

For the vast majority of eruptive and pulsating stars, the $B{-}V$ color index is known to increase with decreasing brightness of the objects; i.e., the coefficient K in the equation

$$V = a + K(B{-}V),$$

which relates the V magnitude and the $B-V$ color index, is positive ($K > 0$). This relation holds irrespective of whether the brightness variations are caused by surface-temperature variations (pulsating variables), flares, or variable dust extinction (eruptive stars). It is true that some of the irregular Algol-like variables show a blueing effect, but this is observed only at deep brightness minima and is basically a secondary effect, since it is attributable to the scattering of photospheric emission by the dust of circumstellar envelopes (Grinin 1988). This effect is not considered here, since it bears no relation to the color anomaly.

Our analysis of $UBVR$ observations for two F-type antiflare stars, BO Cep (Sp F2e) and SU Aur (Sp F5–G2 III), has revealed that the small brightness fluctuations near normal light are accompanied by unusual color variations during which the coefficient K is negative; i.e., the emission becomes bluer rather than redder as the star fades (Pugach 2003, 2004a). The goal of this paper is to search for unusual color variability (UCV) in other stars.

OBSERVATIONS AND THEIR ANALYSIS

Our analysis of the observations of several stars preformed previously at the Terskol high-altitude observing station (Pugach 1996) revealed UCV in stars of spectral types earlier than F. In particular, it was found in VX Cas (Sp A0 IIIe) and IP Per (Sp A3e) (see the table). The results of our analysis of the hot B-type emission-line star $L_kH\alpha$ 373, which has been recorded so far as a variable only in the NSV catalog (NSV 13395), are also of considerable interest. Figure 1 shows the observations of $L_kH\alpha$ 373 performed by Kardopolov and Filip'ev (1985). The solid line in this figure indicates a linear fit to the $V{-}(B{-}V)$ relation for which the coefficient K is negative, suggesting the presence of UCV. In this and all of the following cases, the coefficient K and its error were calculated by the least-squares method.

That UCV is found in stars with greatly differing effective temperatures was the reason why we searched for the UCV in other stellar objects. We used data from various published sources to analyze the color behavior of nonstationary stars of different types. The results of this analysis are presented in the table. This table gives the following: the star's name; its spectral type; the date of observations or the whole period during which the UCV persisted; the number of observations; the amplitude ΔV over the analyzed time interval; the sought-for coefficient K; the cross-correlation coefficient C_c, which shows how closely the quantities being compared are correlated; the references to original data; and notes. In particular, the last column provides information about the photometric systems used in the observations. Some of the authors performed their observations in Strömgren's *uvby* system or the seven-band Vilnius $UPXYZVS$ system rather than in the $UBVR$ system. In these cases, we chose the bands closest to B ($\lambda_{\text{eff}} = 445$ nm) and V ($\lambda_{\text{eff}} = 545$ nm) for our analysis. Thus, for example, we took the observations in the b ($\lambda_{\text{eff}} = 410$ nm) and y ($\lambda_{\text{eff}} = 547$ nm) bands from the observations performed in the four-band

*E-mail: pugach@mao.kiev.ua

1063-7737/05/3107-0452$26.00

Table

Object	Sp	JD 2400000+	N	ΔV	$K \pm \sigma$	$C_c \pm \sigma$	References*	Notes
SU Aur	G2IIIev	41949	50	0.11	-0.563 ± 0.110	-0.591 ± 0.019	1	
VX Cas	A0IIIe	41072	27	0.22	-0.190 ± 0.048	-0.359 ± 0.031	1	
BO Cep	F2e	42191	23	0.111	-0.879 ± 0.245	-0.616 ± 0.035	1	A cross found in the $V-(B-V)$ diagram
V425 Cyg	Bpe	44763–44853	65	0.13	-0.289 ± 0.056	-0.538 ± 0.013	2	
BN Ori	A7–F2pe	46389–46442	24	0.047	-0.150 ± 0.070	-0.413 ± 0.004	3	$b-y$ color index
FU Ori	F2–G3Iape	45250–46486	65	0.184	-0.060 ± 0.027	-0.276 ± 0.010	3, 5	$b-y$ color index
IU Ori	K3III	45265	38	0.137	-0.953 ± 0.256	-0.526 ± 0.046	4	
V346 Ori	A5III	46066–46097	12	0.036	-0.502 ± 0.214	-0.596 ± 0.090	3	$b-y$ color index
V372 Ori	B9.5V+A0.5	45245–46696	85	0.094	-0.361 ± 0.033	-0.771 ± 0.006	3	$b-y$ color index
V380 Ori	B8–A2eq	46381–46443	25	0.079	-0.238 ± 0.065	-0.608 ± 0.008	3	$b-y$ color index
NX Pup	A1–F2IIIe	45246–45324	15	0.408	-0.095 ± 0.059	-0.406 ± 0.028	3, 5	A multitier cross found
		46382–46406	14	0.564	-0.078 ± 0.045	-0.523 ± 0.028		in the $y-(b-y)$ diagram
		46420–46440	14	0.476	-0.053 ± 0.013	-0.701 ± 0.008		
IP Per	A3III	42345	14	0.052	-0.717 ± 0.278	-0.598 ± 0.014	1	
WW Vul	A0III	44819	13	0.17	-0.138 ± 0.081	-0.454 ± 0.015	6	At deep minimum
AS 310	B0e	49577–50308	9	0.092	-0.713 ± 0.287	-0.684 ± 0.024	7	$Z-V$ color index
$L_kH\alpha$ 118	B5Ve	46588–46670	7	0.101	-0.353 ± 0.356	-0.405 ± 0.029	3	$b-y$ color index
$L_kH\alpha$ 324	A/F	49575–50313	15	0.124	-1.019 ± 0.184	-0.837 ± 0.022	7	$Z-V$ color index; V 1982 Ori
$L_kH\alpha$ 373	B	44763–44853	68	0.25	-0.323 ± 0.055	-0.588 ± 0.022	2	
MWC 297	O9e	49577–50315	14	0.076	-0.338 ± 0.453	-0.219 ± 0.242	7	$Z-V$ color index
22 Sco	B3V	46658–46694	34	0.045	-0.277 ± 0.067	-0.590 ± 0.005	3	$b-y$ color index

* References: 1: Pugach (1996); 2: Kardopolov and Filip'ev (1985); 3: Manfroid *et al.* (1991); 4: Koval'chuk (1986); 5: Sterken *et al.* (1993); 6: Zaĭtseva (1983); 7: Eimontas and Sudzius, 1998.

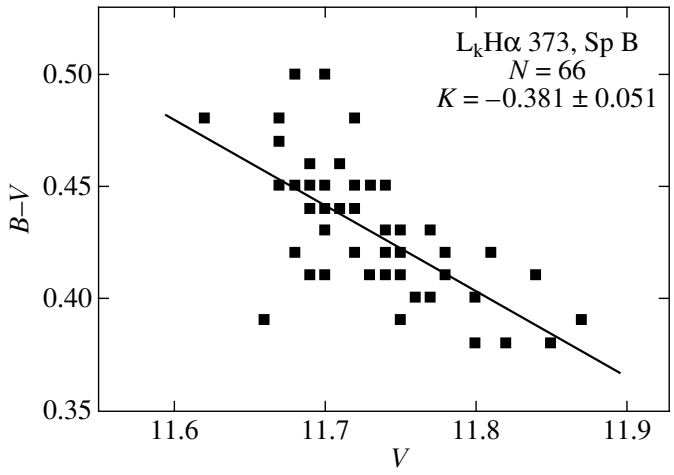

Fig. 1. UCV of the star $L_kH\alpha$ 373 from the observations by Kardopolov and Filip'ev (1985).

uvby system and in the Y or Z bands (the effective wavelengths are 466 and 516 nm, respectively) and the V band ($\lambda_{eff} = 544$ nm) from the observations in the Vilnius $UPXYZVS$ system.

In these cases, of course, the coefficients K derived from slightly differing bands of different photometric systems are not completely identical. We are interested not in the absolute value of the coefficient K but in its sign, an indicator of the sought-for anomaly. Clearly, the noncoincidence of the closely-spaced bands does not change the sign of the relation between V and $B–V$ or similar bands.

RESULTS

Figures 2–5 show the diagrams that point to the presence of a color anomaly in the stars observed by different authors with different telescopes. UCV is present in the brightness variations of not only dwarfs but also giants. Figure 3 shows the color behavior of one of the best-known stellar objects, the supergiant FU Ori, the prototype of a whole subtype of variable stars. The UCV of FU Ori is seen both in the entire set of observations (see the table) and in individual seasons (Fig. 3). It follows from the figures and the table that the UCV manifests itself mainly in small brightness variations. The amplitude averaged over all ΔV values from the table (except NX Pup) is $0^m.114$. This sheds light on why UCV does not always manifest itself, why it is observed most commonly in the state of normal light of the star, and why it is absent during global fadings: at this time, low-amplitude UCV is unseen against the background of large brightness variations.

Figure 4 shows the first published UCV diagram that presents the observations of BO Cep (Pugach 1996). The solid line corresponds to the main process, in which the $B–V$ color index increases with V. The dashed line reflects the presence of a color anomaly. These two lines are almost perpendicular and form a kind of a cross. Clearly, when the two processes act simultaneously, the corresponding data points in the $V–(B–V)$ diagram move in different directions, and the overall pattern becomes ambiguous. UCV priority becomes obvious only when there are no large-amplitude global fadings. That is why UCV is mainly observed when the star's brightness is near its normal value, i.e., when the main variability process is absent. Probably for this reason, we failed to establish the presence of UCV in photometrically very active stars in which the main process is almost always present, e.g., in WW Vul (its light curve was published by Zaĭtseva (1983)), with the exception of one not quite characteristic case on JD 2444819 (the observations by Zaĭtseva (1983)).

The observations of NX Pup, an irregular variable with Algol-like fadings (Manfroid *et al.* 1991), give an even more surprising example of the coexistence of UCV and the main variability process. The UCV manifestations in this star are noticeable even at a fairly large variability amplitude, reaching $1^m.6$. If we break down all of the available observations for NX Pup into seasons, then we easily notice that the color anomaly was clearly present in some of them (in our case, seasons 1, 6, and 7 in Fig. 5a), since fitting precisely these data points yields a slope of the color–magnitude relation characteristic of the UCV (Fig. 5b). Of particular interest is that the star's brightness was attenuated when the UCV clearly manifested itself.

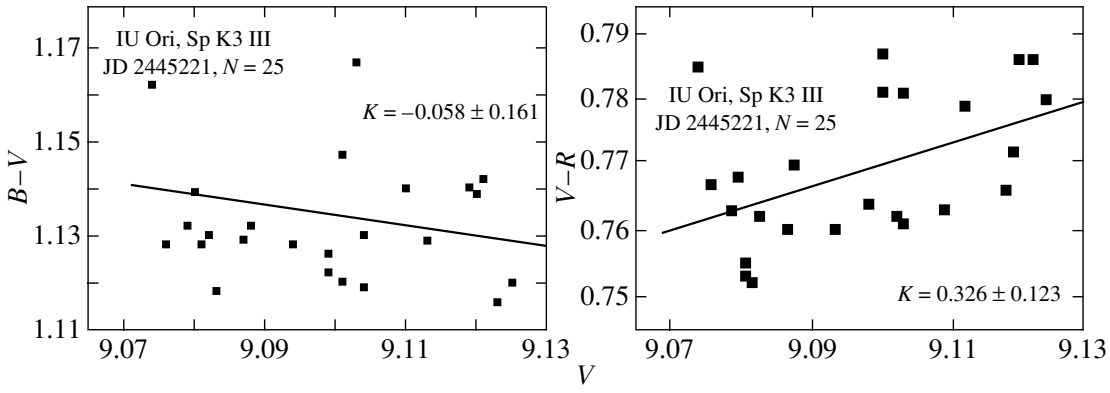

Fig. 2. UCV of IU Ori from the observations on JD 2445221 (Koval'chuk 1986). A similar behavior of the $B-V$ and $V-R$ color indices was also observed on other dates.

Another important characteristic feature of UCV is worth mentioning. During UCV, the $B-V$ and $V-R$ variations are often out of phase: whereas one of the color indices increases, the other decreases and vice versa. Previously, this phenomenon was observed in BO Cep (Pugach 2003) and SU Aur (Pugach 2004a). It has now been confirmed by observations of other stars (see, e.g., the relations in Fig. 2), which are not given here to save space.

DISCUSSION

An analysis of the table suggests that the unusual color variability (UCV) discussed in this paper is typical of a broad class of objects with markedly different physical parameters. UCV has been found in dwarfs, giants, and even the supergiant FU Ori; the photospheric temperatures of these objects range from around 4000 to 20 000 K. This most likely indicates that the color anomaly is not a peculiarity of a particular type or class of stars, but is a certain unstudied physical process that is inherent in stars in general. We cannot help but note that UCV has been found in stars whose circumstellar medium contains dust, as evidenced by the main variability process accompanied by a reddening or by large IR excesses, as, e.g., in the objects MWC 297 and FU Ori.

Another unusual peculiarity of UCV is the opposite behavior of the $B-V$ and $V-R$ color indices. Simple reasoning leads us to conclude that this relation between the color indices would observed only if the anomaly were caused by the variability of light in the V band or, strictly speaking, if the variability amplitude in V were larger than that in the adjacent bands. The same reasoning is also valid for the observations in the bands of Strömgren's or Vilnius systems. It is not yet clear how this relation between $B-V$ and $V-R$ can be reconciled with the well-known variability mechanisms.

The detected effect is unlikely to have a direct bearing on the dust that causes global fadings. First, UCV manifests itself most often precisely when the photometric activity of circumstellar dust structures (individual clouds or a disk) is at a minimum or completely absent. Second, the optical properties of this dust have recently been shown (Pugach 2004b) to be almost the same as those for the interstellar medium. These properties are well known, and there is no place for UCV manifestations here. Therefore, it would be unreasonable to expect the UCV effect from circumstellar dust, at least in antiflare stars.

The phenomenon of a multitier cross that was found for NX Pup, and that manifests itself in less distinct form for several other stars, is a major puzzle for interpreters. If UCV is assumed to be observed only when the main variability is absent, we inevitably

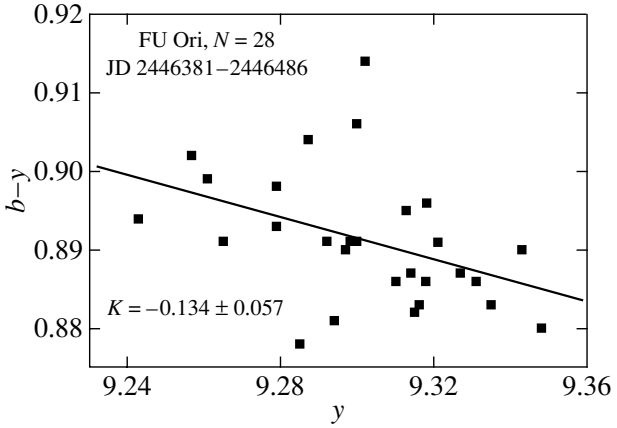

Fig. 3. UCV in the supergiant FU Ori from the observations by Manfroid *et al.* (1991).

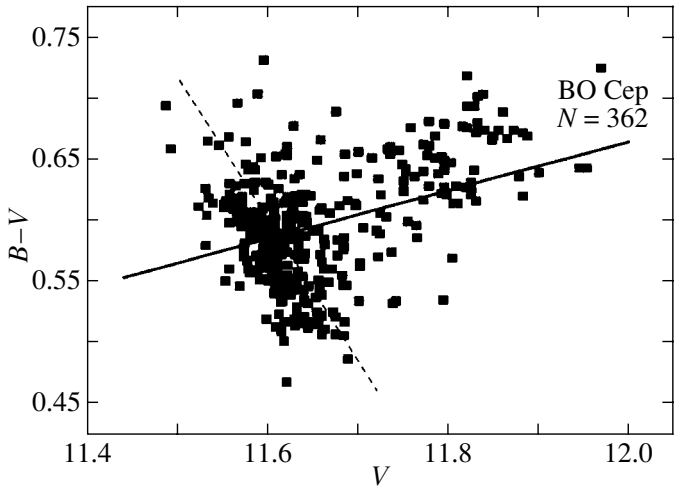

Fig. 4. Superposition of two variability processes for BO Cep, the main process (solid line) and the brightness fluctuations with UCV (dashed line), forming a kind of a cross, since the color–magnitude relations have different signs for these processes.

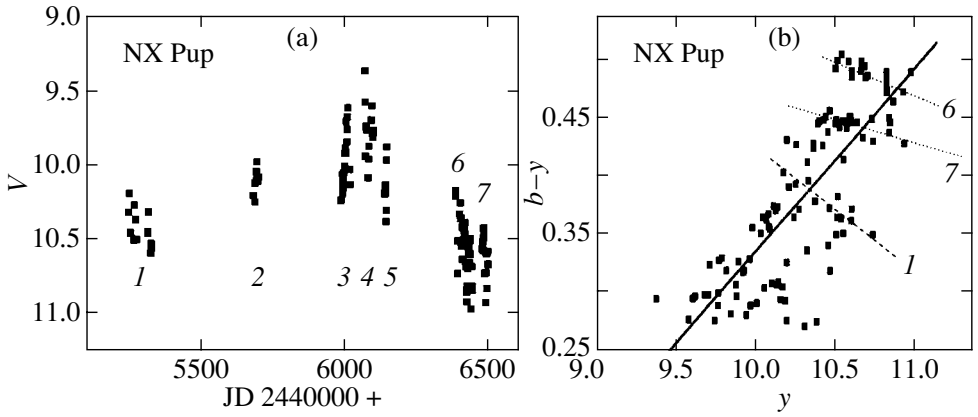

Fig. 5. Peculiarities of the color variability in NX Pup: (a) the brightness variations during individual seasons; (b) the magnitudes and color indices are compared, the dotted rectilinear segments correspond to the UCV observed in seasons 1, 6, and 7. Clearly, these segments are oriented almost across the trend corresponding to the main variability process, forming a multitier cross with it.

come to the paradoxical conclusion that, at certain times, the main variability process of NX Pup freezes at a certain level of brightness to make it possible for UCV to manifest itself.

A conclusion useful for applications can be drawn from the aforesaid. It concerns the photometric observations of many eruptive stars for which no relations between the brightness and color variations have been clearly established, or whose relations differed from the standard ones. In these cases, the idea of two simultaneously acting opposite trends, one of which must be excluded to separate out the other, may prove to be useful.

By no means does UCV always manifest itself. Thus, for example, the observations of the stars 22 Sco and V380 Ori by Sterken *et al.* (1993) during the periods JD 2447023–2447771 and JD 2447806–2448164, respectively, revealed no characteristic UCV features, despite the absence of the main process during these periods and, as a result, the small variability amplitudes, $0^m.10$ and $0^m.15$, respectively.

So far it is too early to talk about the nature of the detected effect. We can say with certainty only that neither emission lines nor their intensity variations are responsible for UCV. For the contribution of an emission line to be 5–10% of the total

light in the V photometric band, its equivalent width must reach several dozen Å. The medium- and low-dispersion spectra of SU Aur, VX Cas, BO Cep, BN Ori, WW Vul, and several other objects with suspected UCV, taken by the author using the 6-m BTA and 2.6-m ZTSh telescopes, show no such strong emission lines in the spectral range under consideration. We can only assume that the UCV is probably associated with circumstellar dust formation at the earliest stages of emergence and growth of the cores of future dust grains. This assumption is consistent with UCV being observed most commonly at maximum light, when the main variability process is absent.

CONCLUSIONS

The numerous observations performed by different authors with different instruments, at different times, and for different objects, clearly reveal the existence of a hitherto unknown type of stellar photometric variability that manifests itself in an unusual behavior of the $B-V$ color index. This variability has arbitrarily been labeled *unusual* because the sign of the $V-(B-V)$ relation during UCV manifestations differs from that observed during the brightness variations caused by temperature variations, flares, or the dust extinction of starlight. Unusual color variability is inherent in eruptive objects with a wide range of physical and geometrical characteristics. These include dwarfs, giants, and supergiants with photospheric temperatures from 4×10^3 to 2×10^4 K; there are many objects with small and/or poorly studied variability among them.

It follows from a comparison of the color behavior of these objects in the U, B, V, and R bands that the unusual behavior under study is due mainly to the V light variations. However, we cannot yet say more about the origin of the UCV, although we have reason to believe that it is not associated with emission lines.

ACKNOWLEDGMENTS

I wish to thank R.E. Gershberg and all of the members of the Crimean Observatory staff who participated in the discussion of this material.

REFERENCES

1. A. Eimontas and J. Sudzius, Baltic Astron. **7**, 407 (1998).
2. V. P. Grinin, Pis'ma Astron. Zh. **14**, 65 (1988) [Sov. Astron. Lett. **14**, 27 (1988)].
3. V. I. Kardopolov and G. K. Filip'ev, Perem. Zvezdy **22**, 103 (1985).
4. G. U. Koval'chuk, Preprint No. 86-29R, ITF UAN (Inst. Theor. Phys. Acad. Sci. Ukr. SSR, 1986).
5. J. Manfroid, C. Sterken, A. Bruch, *et al.*, Astron. Astrophys., Suppl. Ser. **87**, 481 (1991).
6. A. F. Pugach, Perem. Zvezdy **23**, 391 (1996).
7. A. F. Pugach, Kinematika Fiz. Nebesnykh Tel **19**, 234 (2003).
8. A. F. Pugach, Inform. Bull. Var. Stars **5540**, 1 (2004a).
9. A. F. Pugach, Astron. Zh. **81**, 517 (2004) [Astron. Rep. **48**, 470 (2004b)].
10. C. Sterken, J. Manfroid, K. Anton, *et al.*, Astron. Astrophys., Suppl. Ser. **102**, 79 (1993).
11. G. V. Zaĭtseva, Perem. Zvezdy **21**, 1 (1983).

Translated by N. Samus'

Astronomy Letters, Vol. 31, No. 7, 2005, pp. 458–473. Translated from Pis'ma v Astronomicheskiĭ Zhurnal, Vol. 31, No. 7, 2005, pp. 513–530.

Modeling Infrared Absorption Bands with Nonspherical Particles

T. V. Zinov'eva*

Sobolev Astronomical Institute,
St. Petersburg State University, Universitetskii pr. 28, St. Petersburg, 198504 Russia

Received January 27, 2005

Abstract—We investigated the two deepest absorption bands observed in the spectra of stars and protostars, the water-ice band with the center near 3.1 μm and the silicate band with the center near 9.7 μm, by using a core–mantle confocal spheroid model with various axial ratios and relative volumes of the core material. We considered the effect of grain size, shape, structure, chemical composition, and orientation on the central wavelengths of the two bands, their full widths at half maximum (FWHMs), the ratio of the optical depths at their centers, and the polarization. We found that the observed relationships between the FWHMs of the bands and the ratio of their optical depths at the band centers could be explained if we chose slightly oblate or prolate particles ($a/b \lesssim 2$) of small sizes ($r_V \lesssim 0.35$ μm) with a silicate core and a thin ice mantle ($V_{\rm core}/V_{\rm total} \gtrsim 0.7$). © *2005 Pleiades Publishing, Inc.*

Key words: *interstellar medium, gaseous nebulae, infrared absorption bands.*

1. INTRODUCTION

The polarization of light in the interstellar medium suggests the presence of nonspherical dust grains, since spherical grains do not polarize the directly transmitted radiation. Infinite circular cylinders, homogeneous (Greenberg 1968), and core–mantle (Hong and Greenberg 1980; Voshchinnikov *et al.* 1986) particles were the first models of nonspherical particles that were used to interpret the interstellar polarization. Core–mantle particles were introduced due to the assumption about grain growth in interstellar clouds if initial condensation nuclei were present in them (Aannestad and Purcell 1973). In this case, particles composed of a refractory core and a volatile mantle are formed. However, the model of infinite circular cylinders is only an approximation with unclear validity boundaries. Therefore, another model of nonspherical particles, spheroidal particles, has been suggested.

At present, there are many methods for solving the problem of light scattering by a spheroid, but, in most cases, the need for solving infinite series or systems of high-order equations arises. Solving the problem by the method of the separation of variables is most convenient for calculations. This method was first applied to spheroids by Asano and Yamamoto (1975). Subsequently, Farafonov (1983) suggested a different solution for a homogeneous spheroid; Voshchinnikov and Farafonov (1985a–1985c, 1986, 1987) modified it to a more convenient form for performing calculations (for a detailed description of this solution, an analysis of the optical properties of spheroidal particles, and their discussion, see Voshchinnikov (1991)).

Farafonov (1994) used the method of the separation of variables to solve the problem of light scattering by core–mantle confocal spheroids; the solution was described in detail by Farafonov *et al.* (1996). The optical properties of spheroidal interstellar dust grains have been investigated by Martin (1978), Rogers and Martin (1979), Onaka (1980), Mishchenko (1989), Voshchinnikov (1990), Voshchinnikov and Farafonov (1993), Kim and Martin (1995), and others. The scattering of light by core–mantle spheroids was also computed in the Rayleigh approximation by Lee and Drain (1985), O'Donnel (1994), and Il'in (1994) when interpreting the infrared dust bands. Somsikov and Voshchinnikov (1999) showed that for small particles, $r_V \lesssim 1$ μm (r_V is the radius of a sphere with the same volume as the spheroid), the relative deviation of the Rayleigh approximation for coated spheroids in the near infrared from the exact solutions does not exceed 10% at any relative volume of the material in the core and the mantle, or at any axial ratio of the spheroid. They used the Rayleigh approximation presented by Draine and Lee (1984).

A comparison of the computed extinction, linear, and circular polarization factors for statically oriented prolate and oblate homogeneous and core–mantle spheroidal particles (Somsikov 1996) showed that

*E-mail: upasika@mail.ru

1063-7737/05/3107-0458$26.00

their optical properties differ only slightly if the relative volume of the silicate core exceeds 0.75 of the total particle volume, while the appearance of even a small silicate core in an ice particle changes greatly its optical properties. This author found the equivalent radii of the core–mantle spheroidal dust grains responsible for the formation of maximum polarization to be $r_V \approx 0.15$–0.35 μm. A study of two infrared absorption bands (the ice and silicate bands with the centers near 3.1 and 9.7 μm, respectively) in many objects in terms of random grain orientation also showed that the grain sizes are small, $r_V \lesssim 0.35$ μm, and the ice mantles of the grains are thin (Zinov'eva 2003). All of the observational data for the ten-micron silicate band could not be explained in terms of random grain orientation. A constraint on the thickness of the ice mantle also follows from a comparison of the observed and computed silicate band profiles (Zinov'eva 2005).

In this paper, we analyze the dependences of the parameters of the ice and silicate absorption bands on the core–mantle spheroid model parameters. We use both the exact solution of the problem of light scattering by a confocal core–mantle spheroid obtained by Farafonov (1994) and the solution in the Rayleigh approximation. Since we used only small particles, the differences between the computational results are insignificant. In both cases, we computed the efficiency factors with the codes written by Voshchinnikov, Somsikov, and Farafonov for core–mantle confocal spheroidal particles in 1994–1998 at the Astronomical Institute of the St. Petersburg State University.

In Section 2, we perform model calculations for two infrared absorption bands: the 3.1-μm water-ice and 9.7-μm silicate bands. In Section 2.1, we briefly analyze the dependences of the extinction efficiency factors at the centers of the ice and silicate bands and their full widths at half maximum (FWHMs) on the particle size and shape (spheres, spheroids with various axial ratios) and the core material (olivine, astrosil) for randomly oriented particles. In Section 2.2, we impose a constraint on the particle shape in terms of static orientation. In Section 2.3, we study the effect of changes in the particle shape and the angle between the line of sight and the magnetic field on the parameters of the two bands for perfect Davies–Greenstein orientation. In Section 2.4, the same studies are performed for imperfect Davies–Greenstein orientation.

The dependences of the profiles for each of the bands on the model properties and the type of grain orientation are discussed in Section 3. In Section 4, we compare our model calculations of the absorption bands with the observed dependences of the band parameters and model the two bands for protostellar objects. In the last section, we reach conclusions about the shape, size, structure, and chemical composition of the interstellar dust grains that produce the absorption bands with the centers near 3.1 and 9.7 μm in the spectra of stars and protostellar objects.

2. MODEL CALCULATIONS OF THE BANDS

For nonpolarized incident radiation, the efficiency factors of a spheroidal particle are defined as follows:

$$Q_{\rm ext} = \frac{Q_{\rm ext}^{\rm TM} + Q_{\rm ext}^{\rm TE}}{2},$$

$$Q_p = \frac{Q_{\rm ext}^{\rm TM} - Q_{\rm ext}^{\rm TE}}{2},$$

where $Q_{\rm ext}$ is the extinction efficiency factor, $Q_{\rm p}$ is the polarization efficiency factor, $Q_{\rm ext}^{\rm TM}$ is a TM-type wave whose magnetic vector is perpendicular to the plane specified by the particle rotation axis and the direction of propagation of the radiation, and $Q_{\rm ext}^{\rm TE}$ is a TE-type wave whose electric vector is perpendicular to this plane. The model of core–mantle spheroids is described by the following parameters:

(1) the refractive indices of the core and the mantle. We took the refractive indices of the $Mg_{2y}Fe_{2-2y}SiO_4$ olivine with $y = 0.4$ and 0.5 and astrosil for the core and H_2O ice with impurities for the mantle. The optical constants for the silicates and ice were taken from the database of optical constants (JPDOC; see Henning *et al.* 1999);

(2) the axial ratio of the mantle a/b, where a is the semimajor axis, and b is the semiminor axis. By varying a/b, we can change the particle shape from spheres ($a/b \simeq 1$) to needles (extremely prolate spheroids) and disks (extremely oblate spheroids);

(3) the size parameter $2\pi r_V/\lambda$, where r_V is the radius of a sphere of the same volume as the spheroid);

(4) the ratio of the core volume to the total particle volume $V_{\rm core}/V_{\rm total}$.

2.1. Choosing Parameters for Randomly Oriented Particles

The mean cross section for $3D$ orientation is

$$\langle C_{\rm ext}\rangle^{3D} = \int_0^{\pi/2} \frac{1}{2}\left[Q_{\rm ext}^{\rm TM}(\alpha) + Q_{\rm ext}^{\rm TE}(\alpha)\right]\bar{G}(\alpha)\sin\alpha d\alpha. \quad (1)$$

Here, $\bar{G}(\alpha)$ is the mean geometrical cross section of the spheroid,

$$\bar{G}(\alpha) = \frac{G(\alpha)}{\pi r_V^2} = \frac{\left[(a/b)^2\sin^2\alpha + \cos^2\alpha\right]^{1/2}}{(a/b)^{2/3}}$$

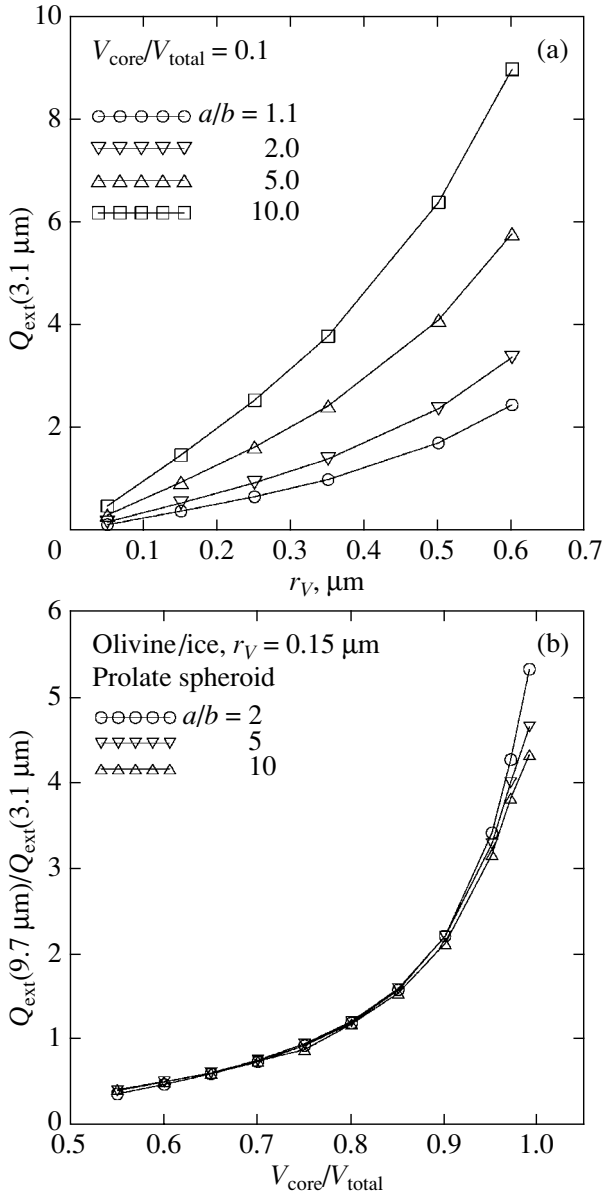

Fig. 1. (a) Extinction efficiency factor at the center of the 3.1-μm ice band versus effective radius of the spheroidal particle and (b) ratio of the extinction efficiency factors at the centers of the silicate and ice bands versus relative volume of the core material for various axial ratios a/b of the spheroid.

for prolate spheroids and

$$\bar{G}(\alpha) = \frac{G(\alpha)}{\pi r_V^2} = \frac{\left[(a/b)^2\cos^2\alpha + \sin^2\alpha\right]^{1/2}}{(a/b)^{1/3}}$$

for oblate spheroids, and α is the angle between the rotation axis and the line of sight. A description of the $3D$ oprientation can be found in the review by Voshchinnikov (2002). We computed integral (1) using the QANC8D code, an automatic adaptive code based on the sixth-order Newton–Cotes formula (Forsythe *et al.* 1977). The relative computational error was 10^{-10}. The extinction efficiency factor was computed with a $\Delta\alpha = 5$ step.

Let us investigate the effect of core–mantle spheroid model parameters on the parameters of the absorption bands. Increasing the particle size causes the central wavelength λ_0 in both bands to shift to the longer wavelengths. The lowest value of λ_0 in the three-micron band is 2.95 μm; the more oblate or prolate the spheroid, the lower the value of λ_0. There is no size dependence in the Rayleigh approximation. In the ten-micron band, λ_0 shifts intangibly if the particle size does not exceed 1 μm. As the ice mantle grows, the central wavelength in the ice band can shift greatly, up to $\Delta\lambda_0 = 0.1$ μm. In the silicate band, it changes only slightly, by 0.05 μm for a thin mantle. If the thickness of the ice mantle is large enough, the 9.7-μm silicate band turns into a single combined band, silicate plus ice, due to the effect of the 12-μm ice band. In this case, the central wavelength is very difficult to determine.

The extinction efficiency factors at λ_0 depend strongly on the particle shape, as demonstrated by Fig. 1a for the ice band. In this figure, the efficiency factor at the center of the three-micron ice band is plotted against the effective particle radius (the calculations were performed by an exact method) for various axial ratios of the spheroids. The figure is drawn for prolate spheroids with a very thick mantle, $V_{core}/V_{total} = 0.1$. We see that Q_{ext} for more prolate particles increases faster with effective particle radius r_V. For oblate spheroids, the extinction efficiency factor behaves similarly.

The ratio of the extinction efficiency factors at the centers of the two bands, $Q_{ext}(9.7\,\mu m)/Q_{ext}(3.1\,\mu m)$, depends very weakly on the particle shape (Fig. 1b), particularly for $V_{core}/V_{total} > 0.95$. The $FWHM$ of the ice band decreases significantly with increasing mantle thickness, from 0.57 μm at $V_{core}/V_{total} \approx 0.99$ to 0.3 μm at $V_{core}/V_{total} \approx 0.55$. In this case, the dependence on the particle shape is weak; the $FWHM$ for a spheroid with an axial ratio of $a/b = 10$ is larger than that for a spheroid with $a/b = 2$ by 0.02 μm. For the silicate band, the $FWHM$ depends strongly on both the mantle thickness and the particle shape. At a mean band $FWHM \approx 3$ μm, it can change from $FWHM \approx 2.5$ μm ($a/b \lesssim 2$ and $V_{core}/V_{total} \gtrsim 0.8$) to $FWHM \approx 3.2\,\mu$m ($V_{core}/V_{total} \lesssim 0.6$ or $a/b = 10$) if the $Mg_{0.4}Fe_{1.2}SiO_4$ olivine is taken as the core material. If the core of the spheroidal particle is composed of astrosil, then the dependence of the silicate band $FWHM$ is even stronger; at $a/b = 10$, it is about 4 μm. For oblate particles, the increase

in the band $FWHM$ with a/b is larger than that for prolate particles.

2.2. Static Orientation

The simplest orientation is the situation where all particles point in the same direction ($\alpha = 90°$) and do not rotate. In this case, the polarizability of a dust grain is at its maximum (in reality, the dust grains rotate due to the unavoidable collisions with gas atoms, causing the polarizability to decrease). This orientation is called a complete static orientation or a "picket fence."

The following relationship defining the polarizability is used to characterize the optical properties of an ensemble of aligned nonrotating particles of the same size:

$$\frac{Q_\mathrm{p}}{Q_\mathrm{ext}} = \frac{Q_\mathrm{ext}^\mathrm{TM} - Q_\mathrm{ext}^\mathrm{TE}}{Q_\mathrm{ext}^\mathrm{TM} + Q_\mathrm{ext}^\mathrm{TE}}.$$

Since the polarization is commonly described in percentage terms, we rewrite this formula as

$$\frac{P(\lambda)}{\tau(\lambda)} = \pm\frac{Q_\mathrm{p}}{Q_\mathrm{ext}} \times 100\% = \pm\frac{Q_\mathrm{ext}^\mathrm{TM} - Q_\mathrm{ext}^\mathrm{TE}}{Q_\mathrm{ext}^\mathrm{TM} + Q_\mathrm{ext}^\mathrm{TE}} \times 100\%, \quad (2)$$

where the "+" and "−" signs are for prolate and oblate particles, respectively; $P(\lambda)$ is the polarization of light by dust grains (in percent), and $\tau(\lambda)$ is the optical depth.

In the case of static orientation, it is convenient to consider the ratio $Q_\mathrm{ext}^\mathrm{TM}/Q_\mathrm{ext}^\mathrm{TE}$, which can easily be derived from formula (2):

$$\frac{Q_\mathrm{ext}^\mathrm{TM}}{Q_\mathrm{ext}^\mathrm{TE}} = \left[\frac{1 + \frac{P/100\%}{\tau}}{1 - \frac{P/100\%}{\tau}}\right]^j,$$

where $j = 1$ and -1 for prolate and oblate spheroids, respectively. If we now assume P/τ to be fixed (e.g., taken from observations), we can determine the dependence of this ratio on the particle shape, the value of P/τ at the band center, and the relative volume of the mantle and the core and find constraints on the grain shape and composition for static orientation by calculating $Q_\mathrm{ext}^\mathrm{TM}/Q_\mathrm{ext}^\mathrm{TE}$. Figure 2a shows this dependence of $Q_\mathrm{ext}^\mathrm{TM}/Q_\mathrm{ext}^\mathrm{TE}$ on P/τ, given in percent, for prolate and oblate particles. Here, the wavelength can be arbitrary (in the infrared), but, in general, the central wavelength λ_0 in the absorption band is considered. Knowing P/τ at the centers of the bands, we can determine $Q_\mathrm{ext}^\mathrm{TM}/Q_\mathrm{ext}^\mathrm{TE}$ and the set of admissible a/b for them (Fig. 2b). We see from Fig. 2b that only nearly spherical particles, $a/b \approx 1$–1.5, can be used to explain the low polarizations in terms of static orientation.

Let us consider the dependences of the band parameters on the model parameters. Figures 2c and 2d show the shift of the central wavelength λ_0 to the longer wavelengths in the three-micron ice and ten-micron silicate bands as the axial ratio of the spheroid a/b increases. The figures were drawn for prolate spheroids with a thin mantle, $V_\mathrm{core}/V_\mathrm{total} = 0.9$; for oblate spheroids, we obtain the same results. We see from these figures that, in both bands, the extinction becomes lower, the efficiency factors decrease, as the axial ratio of prolate spheroids increases. For oblate particles, the efficiency factors increase with a/b. However, as with randomly oriented dust grains, the ratio of the extinction efficiency factors at the centers of the bands for static orientation, $Q_\mathrm{ext}(9.7\ \mu\mathrm{m})/Q_\mathrm{ext}(3.1\ \mu\mathrm{m})$, depends very weakly on the grain shape, changing by no more than 0.5 (as the thickness of the ice mantle increases, this ratio can change significantly, from $Q_\mathrm{ext}(9.7\ \mu\mathrm{m})/Q_\mathrm{ext}(3.1\ \mu\mathrm{m}) \approx 7$ at $V_\mathrm{core}/V_\mathrm{total} = 0.99$ to $Q_\mathrm{ext}(9.7\ \mu\mathrm{m})/Q_\mathrm{ext}(3.1\ \mu\mathrm{m}) \approx 0.3$ at $V_\mathrm{core}/V_\mathrm{total} = 0.5$). The $FWHM$ of the ice band is virtually independent of the grain shape if the grains are statically oriented. The $FWHM$ of the silicate band for such orientation depends strongly on the grain shape. Its minimum value is 2.8 μm at $a/b = 1.1$; the band $FWHM$ is 3.3 μm at $a/b = 10$ and is almost constant as a/b increases further.

2.3. Perfect Davies–Greenstein Orientation

The perfect Davies–Greenstein rotational orientation is a more complex case. For this orientation, the principal axis of a nonspherical particle (in our case, a spheroid) always lies in the same plane. This mechanism has been popular among researchers for many years. It was first suggested by Davies and Greenstein (1951) and received the name paramagnetic relaxation (for a detailed description of this mechanism, see Bohren and Huffman 1983; van de Hulst 1957; Greenberg 1968; Spitzer 1978; Dolginov *et al.* 1979).

The rotation of a dust grain can be decomposed into the rotation around the axis perpendicular to the axis of symmetry and the precession of the angular momentum vector around the magnetic-field direction. The nutation of the angular velocity vector around the angular momentum vector is generally disregarded. For the perfect Davies–Greenstein orientation, only the rotation around the grain axis is taken into account; the precession of the angular momentum vector is disregarded. Therefore, the precession angle is zero, while the angle θ between the line of sight and the height of the cone that the angular

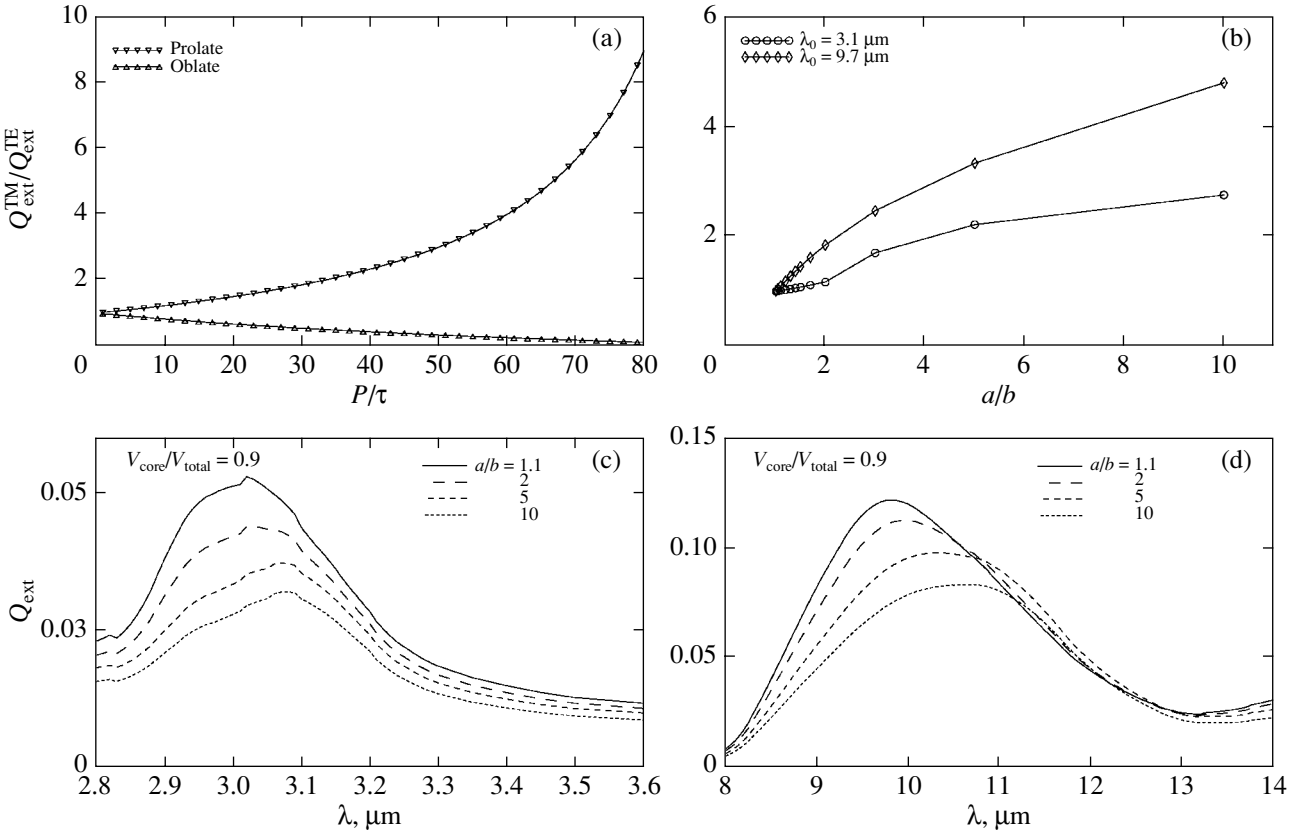

Fig. 2. Ratio $Q_{ext}^{TM}/Q_{ext}^{TE}$ versus (a) P/τ and (b) a/b for prolate and oblate spheroids and extinction efficiency factor versus wavelength in the (c) 3.1-μm ice and (d) 9.7-μm silicate bands.

momentum vector describes about the vector **B** is equal to the angle Ω between the line of sight and the magnetic-field direction, $\theta = \Omega$. The efficiency factors should be averaged only over the rotation angle φ:

$$\bar{Q}_{ext}(m,x,\beta,\Omega) = \frac{2}{\pi}\int_0^{\pi/2} Q_{ext}(m,x,\alpha)d\varphi, \qquad (3)$$

$$\bar{Q}_{p}(m,x,\beta,\Omega) = \frac{2}{\pi}\int_0^{\pi/2} Q_{p}(m,x,\alpha)\cos 2\psi d\varphi,$$

where

$$\cos 2\psi = 1 - \frac{2\cos^2\varphi\sin^2\Omega}{1-\cos^2\varphi\sin^2\Omega}, \qquad (4)$$

$$\cos\alpha = \sin\Omega\cos\varphi.$$

Formulas (3) and (4) to calculate the average extinction and polarization efficiency factors were taken from the paper by Voshchinnikov (1991).

For oblate particles, $\Omega = \alpha$ and the calculations are simplified significantly; no integration is performed. The chemical composition of the dust grain is taken to be the same as that in the previous sections: an olivine core and an impure ice mantle. Since the $Mg_{0.8}Fe_{1.2}SiO_4$ olivine contains iron atoms, the grains may be assumed to have paramagnetic properties. The calculations were performed in the Rayleigh approximation; the integral (for prolate particles) was computed using the QANC8D code with a relative error of 10^{-10}.

For the perfect Davies–Greenstein orientation, the central wavelengths of the two bands (the ice and silicate bands with the centers near 3.1 and 9.7 μm, respectively) shift to the shorter wavelengths as the angle Ω between the line of sight and the magnetic-field direction increases for both oblate and prolate particles. An increase in the axial ratio of the spheroid a/b at fixed Ω causes λ_0 to shift to the longer wavelengths for both bands. Therefore, the shifts to the shorter and longer wavelengths must be taken into account when studying the position of the central wavelength in the absorption band.

At small angles Ω, the extinction efficiency factors at the centers of the two bands depend weakly on Ω (Figs. 3a and 3b) for any axial ratio of the spheroid and any thickness of the ice mantle. The differences

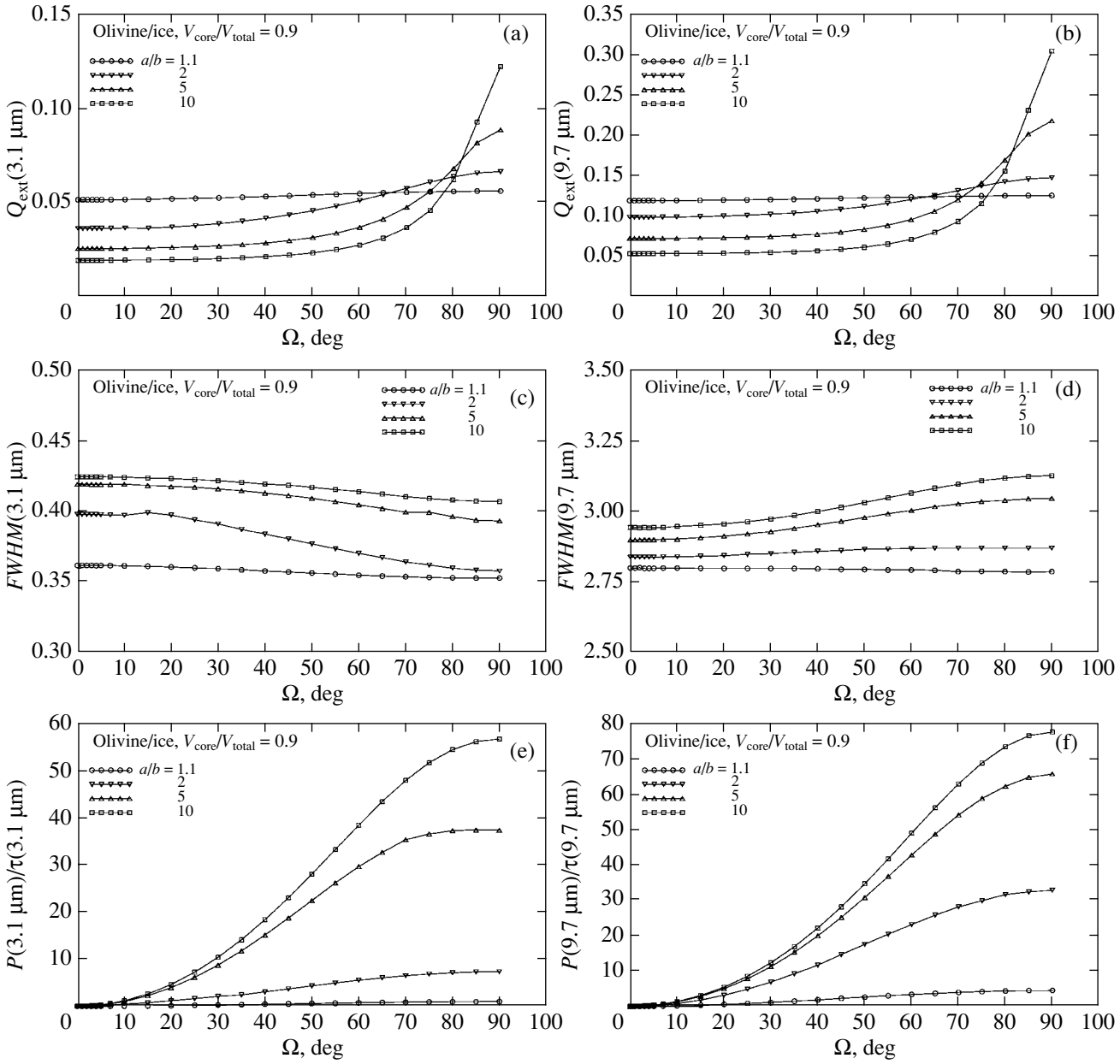

Fig. 3. Extinction efficiency factor at the center of the (a) 3.1-μm ice and (b) 9.7-μm silicate bands, FWHMs of the (c) ice and (d) silicate bands, and polarization in the (e) ice and (f) silicate bands versus angle Ω between the line of sight and the direction of the magnetic-field for various axial ratios of an oblate spheroid.

are significant only at $\Omega > 60°$, with the grain shape playing a major role here. Whereas $Q_{ext}(\Omega = 90°)$ at $a/b = 2$ in both the ice and silicate bands is twice $Q_{ext}(\Omega = 0°)$, $Q_{ext}(\Omega = 90°)$ at $a/b = 10$ increases by a factor of 5. Figure 3 shows the case of an oblate spheroidal particle with a thin mantle, $V_{core}/V_{total} = 0.9$; for any other values of V_{core}/V_{total}, the pattern of behavior of the efficiency factors is qualitatively the same. The ratios of the extinction efficiency factors at the band centers are sensitive to variations in Ω, particularly at small a/b. However, their values lie within a narrow range, $Q_{ext}^{max} - Q_{ext}^{min} \lesssim 0.7$.

The FWHMs of the bands depend very weakly on the angle Ω; this is especially true for the three-micron ice band, whose FWHM decreases slightly with increasing Ω (Fig. 3c). In contrast, the FWHM of the ten-micron silicate band increases with Ω; this is particularly noticeable for large axial ratios of the

spheroid (Fig. 3d). As we see from the figures, the FWHMs of the two bands depend strongly on a/b, increasing significantly with it.

The linear polarization depends most strongly on the angle between the line of sight and the magnetic-field direction. As we see from Figs. 3e and 3f, when the incident radiation is absorbed by oblate spheroids, it depends weakly on Ω only at small Ω or a/b (nearly spherical particles), particularly in the silicate band. At $\Omega > 30^\circ$, oblate spheroidal particles with an axial ratio $a/b > 2$ produce a fairly high polarization; it increases rapidly with Ω and a/b, reaching its maximum at $\Omega = 90^\circ$. The dependence on the mantle thickness is very weak, especially if the mantle is thin. In the silicate band, the polarizability varies by about the same value, changing by no more than 1% if $V_{\rm core}/V_{\rm total} > 0.7$; as the mantle thickness increases further, it changes by only a few percent. In the ice band, the polarizability slowly and monotonically decreases by a few percent with growing particle mantle.

For prolate particles, the situation with polarization is opposite: prolate particles yield the highest polarizability at $\Omega = 0^\circ$; its value is one and a half times lower than that for oblate spheroidal particles. The behavior of the extinction efficiency factors and the band FWHMs when the radiation is absorbed by prolate particles is the same as that for the absorption by oblate particles, the only difference being that the dependence on Ω and a/b is weaker.

2.4. Imperfect Davies–Greenstein Orientation

The interaction of the magnetic moment of a dust grain with a weak magnetic field leads to a precession of the angular momentum of the grain about the direction of the magnetic field. Paramagnetic relaxation slows down the rotation of dust grains around the axes that do not coincide with the magnetic field's direction. In this case, the semimajor axis of the grain tends to become perpendicular to the angular momentum vector. Precession causes the angle between the direction of propagation of the radiation and the direction of the angular momentum vector to change.

For the imperfect Davies–Greenstein orientation, the efficiency factors should be averaged not only over the rotation angle, but also over the precession angle. In this case, formulas (3) and (4) that relate the angles take a more complex form.

The linear polarization produced by rotating spheroidal particles of the same size can be written in general form as

$$P(\lambda) = \frac{2}{\pi^2}\int\limits_0^{\pi/2}\int\limits_0^{\pi}\int\limits_0^{\pi/2} N_{\rm d} C_{\rm p}(m, r_V, \lambda, a/b, \alpha) \quad (5)$$
$$\times f(\xi,\beta)\cos 2\psi d\varphi d\omega d\beta \times 100\%,$$

where $N_{\rm d}$ is the particle column density,

$$C_{\rm p}(m, r_V, \lambda, a/b, \alpha 0) = \bar{G}(\alpha) Q_{\rm p}(m, r_V, \lambda, a/b, \alpha) \quad (6)$$

is the polarization cross section,

$$\cos 2\psi = \cos 2\Phi\left[\frac{2\cos^2\varphi\sin^2\theta}{1-\cos^2\varphi\sin^2\theta} - 1\right], \quad (7)$$
$$\cos\theta = \cos\Omega\cos\beta + \sin\Omega\sin\beta\cos\omega,$$
$$\cos 2\Phi = \frac{2\sin^2\beta\sin^2\omega - \sin^2\theta}{\sin^2\theta},$$
$$\cos\alpha = \sin\theta\cos\varphi.$$

Here, Φ is the angle between the x axis and the projection of the angular momentum vector onto the xy plane, θ is the angle between the line of sight and the height of the cone that the angular momentum vector describes about the vector **B**, Ω is the angle between the line of sight and the magnetic field's directions, β is the opening angle of the cone that the angular momentum vector describes about the vector **B**, and ω is the precession angle.

The optical depth $\tau(\lambda)$ for the imperfect Davies–Greenstein orientation of spheroidal particles is

$$\tau(\lambda) = \left(\frac{2}{\pi}\right)^2\int\limits_0^{\pi/2}\int\limits_0^{\pi/2}\int\limits_0^{\pi/2} N_{\rm d} \quad (8)$$
$$\times C_{\rm ext}(m, r_V, \lambda, a/b, \alpha) f(\xi,\beta) d\varphi d\omega d\beta.$$

The imperfect Davies–Greenstein orientation is described by the function $f(\xi,\beta)$, which depends on the orientation parameter ξ and the angle β. In the simplest case,

$$f(\xi,\beta) = \frac{\xi\sin\beta}{(\xi^2\cos^2\beta + \sin^2\beta)^{3/2}}. \quad (9)$$

The orientation parameter ξ is a function that depends on the grain size, the imaginary part of the magnetic susceptibility of the grain material $\chi'' = \kappa\omega_{\rm d}/T_{\rm d}$ ($\omega_{\rm d}$ is the angular velocity of the dust grain), the gas density $n_{\rm g}$, the magnetic field strength B, and the dust, $T_{\rm d}$, and gas, $T_{\rm g}$, temperatures:

$$\xi^2 = \frac{r_V + \delta_0^{\rm IDG}(T_{\rm d}/T_{\rm g})}{r_V + \delta_0}, \quad (10)$$

where

$$\delta_0^{\rm IDG} = 8.28\times 10^{23}\frac{\kappa B^2}{n_{\rm g} T_{\rm g}^{1/2} T_{\rm d}} \ \ \mu{\rm m}. \quad (11)$$

Formulas (5)–(11), which are needed to compute the average extinction and polarization efficiency factors, were taken from the papers by Voshchinnikov (1991, 2002).

The value of κ is generally taken to be $\kappa = 2.5 \times 10^{-12}$, and was first obtained by Davies and Greenstein (1951). The mean interstellar magnetic field strength is $B \approx 3$ μG. Using these values and the mean parameters that characterize the interstellar gas and dust, $n_g = 1\ \mathrm{cm}^{-3}$, $T_g = 100$ K, and $T_d = 10$ K, we obtain after their substitution into (11) $\delta_0^{IDG} \approx 0.19$ μm (see Voshchinnikov 1991). In general, the silicate dust temperature is slightly higher, $T_d \approx 20$ K. In this case, as was noted by Voshchinnikov (1986), the dependence of the dust temperature on the grain size is not strong. Mezger *et al.* (1982) found the grain temperatures at a ratio of the grain radii $\lesssim 10^3$ to differ by less than 20%.

In this paper, we restrict our analysis to the parameters of the absorption bands produced by silicate grains coated with ice mantles with the weight function $f(\xi, \beta)$ determined by the orientation mechanism that depends on the fixed orientation parameter ξ.

Greenberg (1968) showed that decreasing the degree of grain orientation from the perfect Davies–Greenstein orientation reduces the polarization and flattens its wavelength dependence. Figures 4a and 4b show this dependence for the imperfect Davies–Greenstein orientation for the two infrared bands under study. Since the grain column density N_d is generally unknown and can vary from object to object, it is usually eliminated by studying not the optical depths and polarization in the bands, but their ratios: $\tau(9.7\ \mu\mathrm{m})/\tau(3.1\ \mu\mathrm{m})$, $P(9.7\ \mu\mathrm{m})/\tau(9.7\ \mu\mathrm{m})$, $P(3.1\ \mu\mathrm{m})/\tau(3.1\ \mu\mathrm{m})$. Formulas (5) and (8) were used to calculate these ratios for the imperfect Davies–Greenstein orientation. We see from the figures that the grain polarizability in both bands decreases monotonically by a few percent with an increasing orientation parameter ξ. The figures were drawn for oblate spheroidal grains with axial ratios of $a/b = 1.1, 2, 5, 10$ at $V_{core}/V_{total} = 0.9$ and $\Omega = 0°$. Similar results are obtained for any other relative volumes of the grain core and angles Ω between the line of sight and the magnetic-field direction. In this case, the FWHM of the 3.1-μm band increases slightly, while the FWHM of the 9.7-μm is virtually constant. The ratio of the optical depths in the bands, $\tau(9.7\ \mu\mathrm{m})/\tau(3.1\ \mu\mathrm{m})$, also depends weakly on ξ.

For the imperfect Davies–Greenstein orientation, just as for any other grain orientation or in its absence, the grain shape, i.e., the axial ratio a/b (for a spheroidal grain), has the strongest effect on the variations in the absorption band parameters. As we see from Fig. 4, increasing the grain nonsphericity causes a large increase in the grain polarizability and a significant broadening of the two bands. In this case, the ratio $\tau(9.7\ \mu\mathrm{m})/\tau(3.1\ \mu\mathrm{m})$ depends weakly on a/b.

The grain polarizability increases slightly with a growing ice mantle for the three-micron ice band (Fig. 4c) and decreases in the silicate band (Fig. 4d). The FWHM of the ice band depends strongly on the mantle thickness for a thin mantle, $V_{core}/V_{total} > 0.85$; here, it decreases rapidly from $FWHM \approx 0.8$ μm to 0.35 μm, and, for $V_{core}/V_{total} < 0.8$, it decreases slowly to 0.3–0.27 μm (Fig. 4e). The effect of the grain shape on the band FWHM is also strongest for a thin mantle; at $V_{core}/V_{total} < 0.8$, it decreases significantly, $FWHM(3.1\ \mu\mathrm{m})$ changes by no more than 0.05 μm. In contrast, the FWHM of the silicate band increases with growing ice mantle; the FWHMs of the bands produced by more oblate or prolate grains depend less strongly on the growth of the grain mantle (Fig. 4f). As we see from Fig. 4, the dependence of the FWHM for the ten-micron silicate band on the grain shape (the axial ratio a/b of the spheroid) is strongest at $V_{core}/V_{total} > 0.8$ or $V_{core}/V_{total} < 0.7$. At $0.7 < V_{core}/V_{total} < 0.8$, the grain shape affects the band FWHM only slightly.

The ratio of the optical depths at the band centers, $\tau(9.7\ \mu\mathrm{m})/\tau(3.1\ \mu\mathrm{m})$, monotonically decreases with growing ice mantle for any a/b, grain type (prolate or oblate), and angles Ω. The dependence of all parameters of the bands on the angle between the line of sight and the magnetic-field direction is presented in the table. We see from this table that the ratio of the optical depths and the FWHMs of the two bands depend very weakly on Ω (only the second decimal figure changes); their values are at a minimum at $\Omega = 30°–50°$ for oblate particles. For prolate particles, the dependence is also very weak. The grain polarizability decreases slowly with increasing Ω in both bands.

The central wavelengths λ_0 of the two bands depend neither on the orientation parameter ξ nor on the angle Ω between the line of sight and the magnetic-field direction and depend weakly on the thickness of the ice mantle and strongly on its shape, changing from $\lambda_0 = 3.02$ μm at $a/b = 1.1$ to $\lambda_0 = 3.07$ μm at $a/b = 10$ in the ice band and from $\lambda_0 = 9.7$ μm at $a/b = 1.1$ to $\lambda_0 = 10.5$ μm at $a/b = 10$ in the silicate band.

3. DISCUSSION

In the previous section, we studied the effect of model parameters (the size, shape, and relative core and mantle volumes) of a nonspherical grain (prolate and oblate spheroids) and its orientation mechanisms on the parameters of two infrared absorption bands (the ratio of the optical depths at the centers of the bands, their central wavelengths and FWHMs, and the polarization in the bands). In this section, we combine the results of our studies for each band and

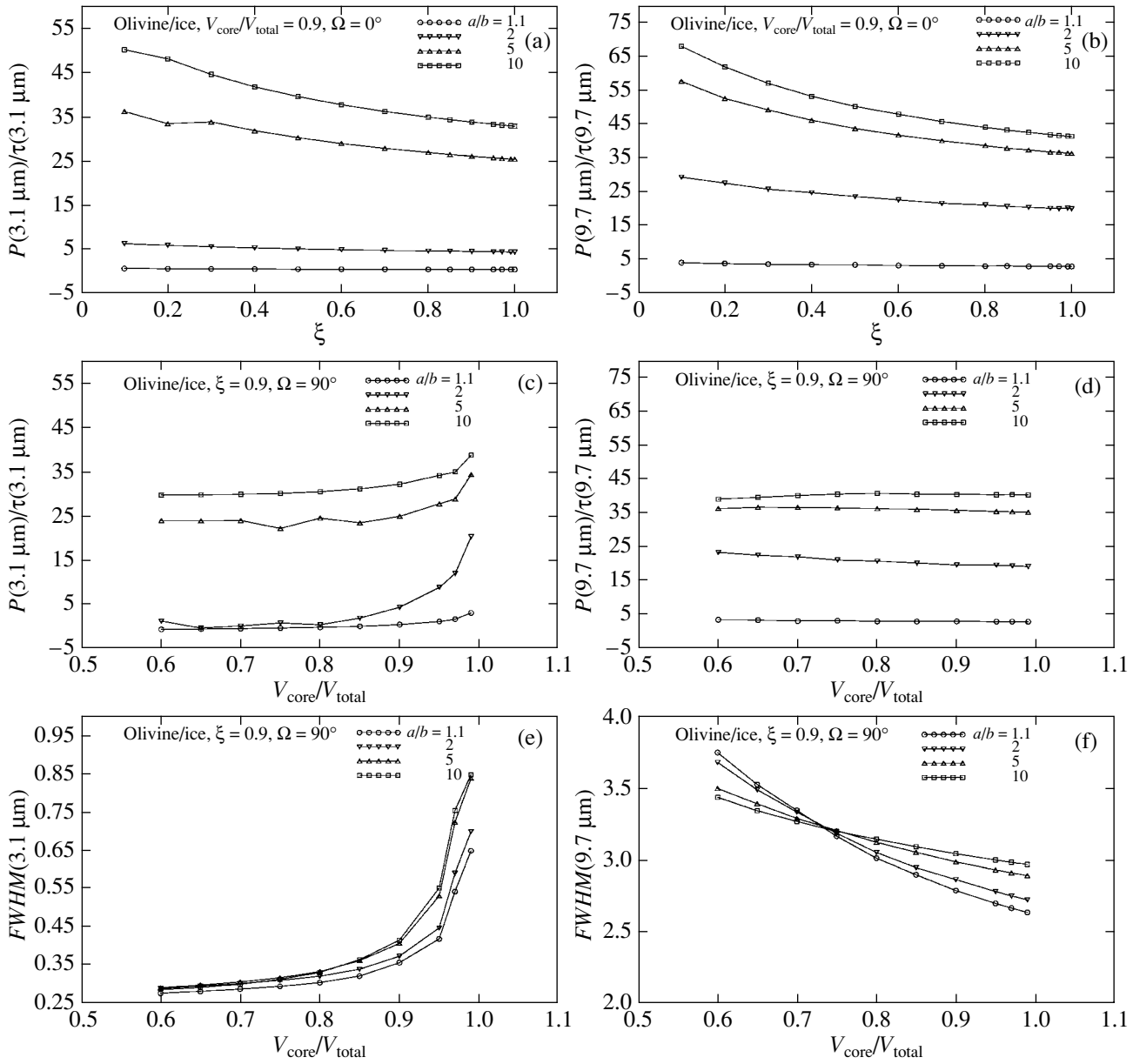

Fig. 4. Ratio of the polarization to the optical depth versus orientation parameter ξ in the (a) 3.1-μm ice and (b) 9.7-μm silicate absorption bands and versus relative core volume in the (c) ice and (d) silicate bands as well as band FWHMs versus relative core volume in the ice (e) and silicate (f) bands for various axial ratios of an oblate spheroid.

discuss the dependences of their profiles on the model properties and the type of orientation.

3.1. The Ice Band, $\lambda_0 = 3.1$ μm

(1) The central wavelength in the three-micron ice absorption band depends on the grain size and shape, the relative mantle volume, and the grain orientation. As the equivalent radius r_V of the radiation-absorbing grain increases, the central wavelength in the band shifts slightly to the longer wavelengths. As the thickness of the ice mantle increases, λ_0 also shifts to the longer wavelengths for any grain orientation. Changing the grain shape (increasing a/b) causes the central wavelength to shift to the longer wavelengths for all grain orientations, except the random ($3D$) orientation for which λ_0 shifts to the shorter wavelengths. The shift to the shorter wavelengths also takes place as the angle Ω between the line of sight and the magnetic field's direction increases

Dependence of the parameters of the ice and silicate absorption bands on the angle Ω between the line of sight and the magnetic-field direction at $a/b = 2, \xi = 0.9, V_{\rm core}/V_{\rm total} = 0.9$

Ω	$\frac{\tau(9.7\ \mu{\rm m})}{\tau(3.1\ \mu{\rm m})}$	$FWHM(3.1\ \mu{\rm m})$	$FWHM(9.7\ \mu{\rm m})$	$\frac{P(3.1\ \mu{\rm m})}{\tau(3.1\ \mu{\rm m})}$	$\frac{P(9.7\ \mu{\rm m})}{\tau(9.7\ \mu{\rm m})}$
0°	2.405	0.373	2.869	4.716	20.49
5	2.398	0.373	2.868	4.722	20.80
10	2.387	0.372	2.869	4.728	20.70
15	2.378	0.371	2.868	4.731	20.80
20	2.370	0.371	2.869	4.730	20.97
25	2.363	0.370	2.869	4.729	20.81
30	2.358	0.370	2.869	4.721	20.92
35	2.354	0.369	2.870	4.707	20.79
40	2.352	0.369	2.870	4.697	20.76
45	2.353	0.369	2.869	4.683	20.80
50	2.355	0.369	2.869	4.669	20.83
55	2.358	0.370	2.870	4.653	20.52
60	2.364	0.370	2.869	4.640	20.52
65	2.371	0.371	2.868	4.628	20.50
70	2.378	0.371	2.870	4.612	20.16
75	2.388	0.372	2.869	4.597	20.12
80	2.398	0.373	2.869	4.583	19.97
85	2.410	0.374	2.868	4.570	19.93
90	2.419	0.374	2.868	4.560	19.70

for the perfect Davies–Greenstein orientation. The central wavelength λ_0 is shortest ($\lambda_0^{\rm min} = 2.95\ \mu$m) when the incident radiation is absorbed by very small ($r_V \approx 0.05\ \mu$m), extremely prolate or oblate ($a/b = 10$) randomly oriented grains. The longest central wavelength in the band is 3.09 μm.

(2) The FWHM of the three-micron ice band depends weakly on the grain shape if the grain is randomly or statically oriented. For the complete or imperfect Davies–Greenstein orientation, the band FWHM increases greatly with grain axial ratio. The thickness of the mantle of a core–mantle spheroid has the strongest effect on the band FWHM (for any orientation). Grains with a very thin ice mantle, $V_{\rm core}/V_{\rm total} \approx 0.99$, produce the broadest bands: $FWHM \approx 0.7\ \mu$m. The band FWHM decreases rapidly to $FWHM \approx 0.3$–$0.4\ \mu$m with increasing mantle thickness for $V_{\rm core}/V_{\rm total} < 0.8$ and changes only slightly as the mantle thickness increases further.

(3) The linear polarization in the band for any type of grain orientation depends strongly on the grain shape, increasing rapidly for $a/b > 2$. Whereas the grain polarizability at $a/b \approx 1.1$ is a few percent, its value at $a/b = 10$ increases to 60%. The dependence on the mantle thickness is weak for any orientation. The dependence on the orientation parameter ξ (for the imperfect Davies–Greenstein orientation) and on the angle Ω between the line of sight and the magnetic field's direction is weak. For the perfect Davies–Greenstein orientation, oblate spheroids with $a/b > 2$ at large Ω ($\Omega > 30°$) produce a high polarization, which increases rapidly with Ω. In contrast, prolate spheroids produce a high linear polarization at small angles, decreasing rapidly with increasing Ω.

3.2. The Silicate Band, $\lambda_0 = 9.7\ \mu m$

(1) For a thin mantle, λ_0 shifts intangibly, irrespective of the type of grain orientation. Noticeable changes in λ_0 begin at $V_{\rm core}/V_{\rm total} < 0.7$. At such a mantle thickness, the neighboring 12-μm ice band

contributes to the ten-micron silicate band; as a result, the silicate band broadens, the shape of its profile changes, and the position of its center shifts. Increasing the axial ratio a/b of spheroidal grains causes the center of the band produced by them to shift greatly (to the longer wavelengths). Whereas the centers of the bands produced by nearly spherical grains ($a/b \approx 1.1$) are near 9.7 μm, extremely prolate or oblate grains produce bands with centers near $\lambda_0 \approx 10.5$ μm or longer. This is true for any type of orientation. For the perfect Davies–Greenstein orientation, the central wavelength shifts slightly to the shorter wavelengths with an increasing Ω when the incident radiation is absorbed by both prolate and oblate grains.

(2) The FWHM of the silicate band for any grain orientation depends strongly on the shape of the grain producing it and on the thickness of the ice mantle. For small a/b ($a/b < 2$) or thin mantles ($V_{\rm core}/V_{\rm total} > 0.8$), this dependence is weak; the band FWHMs are almost constant. Since the ten-micron silicate band virtually merges with the twelve-micron ice band, their total FWHM increases rapidly for $V_{\rm core}/V_{\rm total} < 0.6$. The minimum FWHM when the radiation is absorbed by oblate or prolate spheroids with $a/b < 2$ and a thin mantle is $FWHM = 2.5$ μm; in this case, the dust grains are randomly oriented. Statically or randomly ($FWHM = 3.2$ μm) oriented spheroids with large a/b ($a/b \approx 10$) produce the broadest bands, $FWHM = 3.3$ μm. The band FWHMs do not change as a/b (the grain nonsphericity) increases further. Grains with a thick mantle produce the same broad bands. The dependence of the band FWHM on the mantle thickness weakens as the axial ratio of the spheroid increases. If astronomical silicate (astrosil) is taken as the grain core, then the bands are even broader, about 4 μm.

The FWHM of the silicate band depends weakly on all the remaining model parameters of the grain and its position in space.

(3) The grain shape has the strongest effect on the linear polarization in the silicate band. Nearly spherical or slightly oblate (prolate) grains produce a low polarization for any grain orientation. The polarizability of spheroidal grains with large a/b can reach 80%; its value depends weakly on the mantle thickness. If the mantle is thin, $V_{\rm core}/V_{\rm total} > 0.7$, then the polarizability $Q_{\rm p}/Q_{\rm ext}$ varies near the same value, changing by no more than 1%. The linear polarization depends very weakly on the orientation parameter ξ and the angle Ω (for the imperfect Davies–Greenstein orientation). For the perfect Davies–Greenstein orientation, the polarization in the silicate band, just as in the ice band, increases rapidly at $\Omega > 30°$ (for oblate grains), and the linear polarization decreases rapidly starting from $\Omega > 0°$ (for prolate grains).

The ratio of the optical depths in the bands depends weakly on the grain shape, orientation, and location relative to the line of sight and the direction of the magnetic field. The value of $\tau(9.7\ \mu\text{m})/\tau(3.1\ \mu\text{m})$ depends strongly only on the thickness of the ice mantle (particularly at $V_{\rm core}/V_{\rm total} > 0.9$), decreasing severalfold with the growing mantle.

The central wavelengths in the two polarization bands are shifted slightly (compared to λ_0 at the centers of the absorption bands) to the longer wavelengths in all cases. When analyzing the parameters of the absorption and polarization bands, we considered $\tau(9.7\ \mu\text{m})/\tau(3.1\ \mu\text{m})$, $P(9.7\ \mu\text{m})/\tau(9.7\ \mu\text{m})$, and $P(3.1\ \mu\text{m})/\tau(3.1\ \mu\text{m})$ computed for the centers of the absorption bands. The polarizations in them differ from the central values of the polarization bands by no more than 0.5%.

The central wavelength in the band and the ratio of the optical depths are of paramount importance in studying the absorption bands. The central wavelength and the ratio of the optical depths determine the grain shape and the mantle thickness, respectively. For the silicate band, the appearance of its profile, which can also be used to estimate the thickness of the mantle of the band-producing grains, plays a major role.

4. COMPARISON WITH OBSERVATIONS

In this section, we compare the results of our model calculations performed in the previous section with the infrared absorption bands observed in the spectra of stars and protostellar objects and estimate the shape, size, structure, and chemical composition of the interstellar grains producing these bands. The observational data were taken from the following papers: Bowey *et al.* (1998), Brooke *et al.* (1999), Boogert *et al.* (2000), Gibb *et al.* (2000, 2001), Dartois and d'Hendecourt (2001), Palumbo (1997), Pendleton *et al.* (1999), Smith *et al.* (2000), Teixeira and Emerson (1999), Tielens *et al.* (1996), Whittet *et al.* (1983, 1996), and Hough *et al.* (1989). For the silicate band, we also use the observational data provided by Dr. Smith in electronic form.

4.1. Size

Figure 5 shows how the observed and theoretical FWHMs of the 3.1-μm ice and 9.7-μm silicate band depend on the ratio of the optical depths $\tau(9.7\ \mu\text{m})/\tau(3.1\ \mu\text{m})$ at their centers. It follows from the figures that both the ice and silicate bands with parameters similar to their observed values are obtained if we take small dust grains whose equivalent

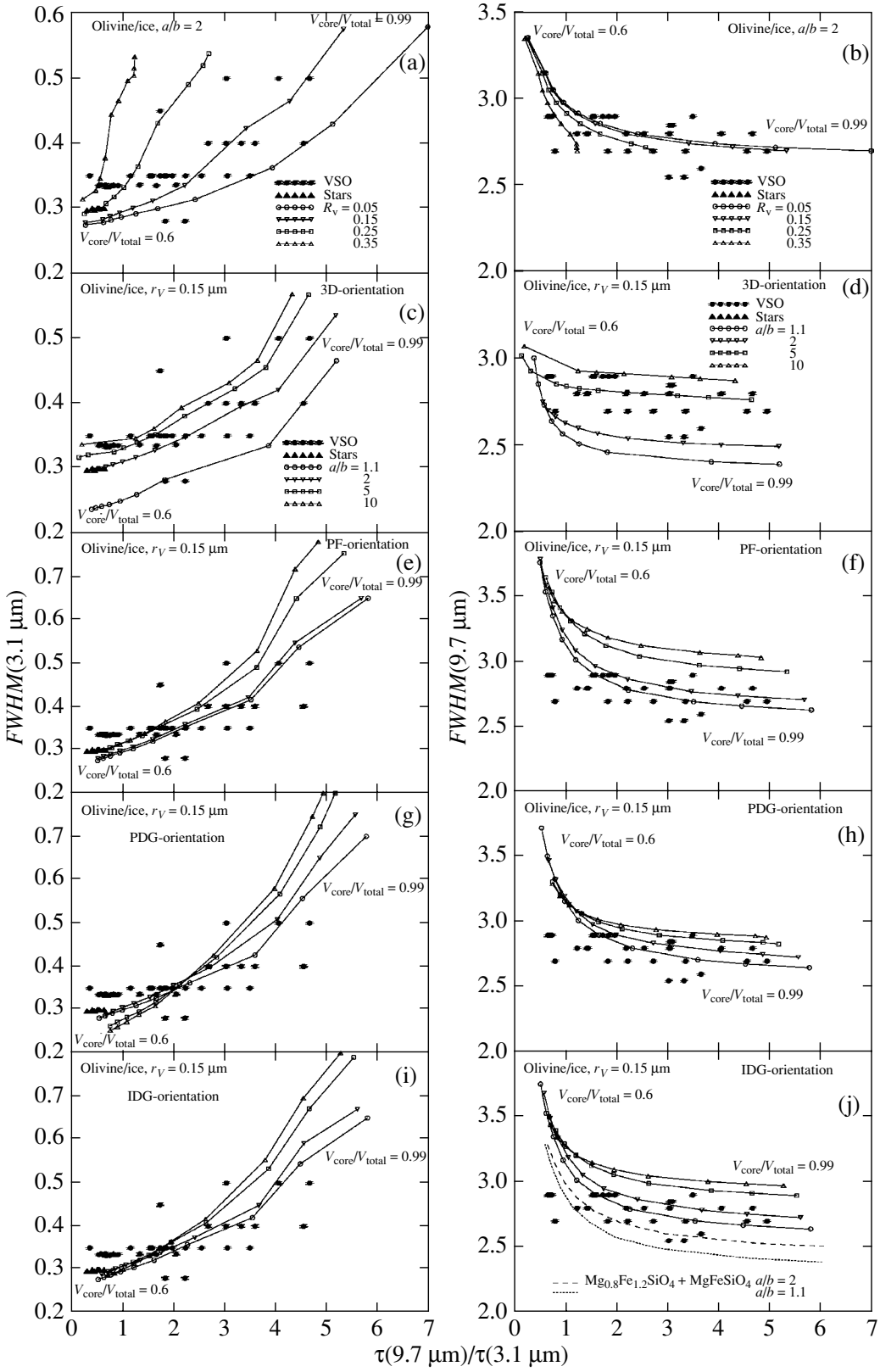

Fig. 5. FWHMs of the 3.1-μm ice (left column) and 9.7-μm silicate (right column) absorption bands versus ratio of the optical depth at the band centers. The effects of changes in the grain size (upper panels) as well as the effect of changes in the mantle shape and thickness for various grain orientation mechanisms are illustrated: random (3*D*), static (PF), perfect Davies–Greenstein (PDG), and imperfect Davies–Greenstein orientations.

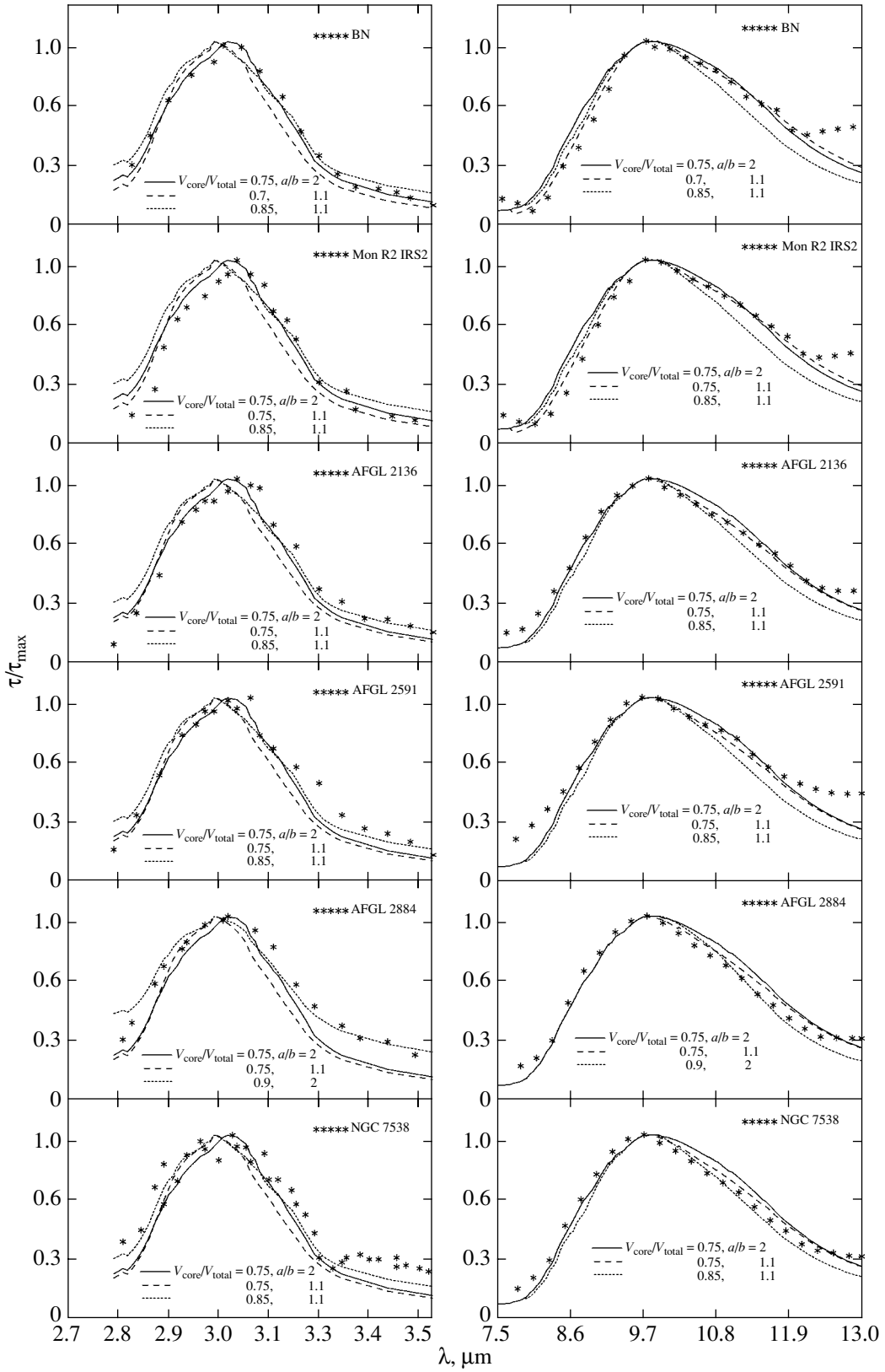

Fig. 6. Normalized optical depths of the 3.1-μm ice (left column) and 9.7-μm silicate (right column) absorption bands for some of the observed (denoted by asterisks) and modeled protostellar sources. Core–mantle oblate spheroids with a silicate ($Mg_{0.8}Fe_{1.2}SiO_4$) core and a thin ice mantle produce the modeled bands for the imperfect Davies–Greenstein orientation.

radius r_V does not exceed 0.35 μm (Figs. 5a and 5b). Such constraints on the grain size exist for any type of grain orientation. For our model calculations, we used the exact solution of the problem of light scattering by confocal core–mantle spheroids (Farafonov *et al.* 1996).

4.2. Structure

The observational data for protostellar objects show that $\tau(9.7\ \mu\text{m})/\tau(3.1\ \mu\text{m}) > 1$ for most of the objects. Such ratios of the optical depths are obtained only for thin mantles, $V_{\text{core}}/V_{\text{total}} \gtrsim 0.7$–$0.75$ for spheroids (Figs. 5c–5j) and $V_{\text{core}}/V_{\text{total}} \gtrsim 0.7$ for smooth spheres with uneven surfaces (Zinov'eva 2005). In this case, the grain can be oriented arbitrarily. For stars in molecular clouds, $\tau(9.7\ \mu\text{m})/\tau(3.1\ \mu\text{m}) > 0.3$; the upper limit was not determined due to the small number of observational data. In this case, however, it is necessary that $V_{\text{core}}/V_{\text{total}} \gtrsim 0.5$ for spheroids and $V_{\text{core}}/V_{\text{total}} \gtrsim 0.55$ for spheres.

The profiles of the 9.7-μm band in the spectra of protostellar objects can also be considered as evidence for the existence of thin ice mantles in the dust grains producing the silicate absorption bands. The 12-μm ice band, which affects the appearance of the profile of the neighboring 9.7-μm silicate band, must also be always present in sources with the 3.1-μm absorption band. In general, this band is barely seen in the observed protostellar objects where it distorts the 9.7-μm band only slightly. In our previous paper (Zinov'eva 2005), we chose the five profiles of protostars that were distorted most severely by the twelve-micron band (its contribution is negligible in the spectra of other protostars (see, e.g., Smith *et al.* 2000)) and showed that such profiles are obtained only in the case of a thin ice mantle, $V_{\text{core}}/V_{\text{total}} \gtrsim 0.5$ for the most severely distorted profiles. We used the model of a radially inhomogeneous sphere with intermediate layers that approximated spherical grains with uneven surfaces (Zinov'eva 2004). For the core–mantle spheroid used in this paper, the mantle must be even thinner, $V_{\text{core}}/V_{\text{total}} \gtrsim 0.6$. Such profiles are obtained for any type of grain orientation.

4.3. Shape

The shape of the grains producing the absorption bands is determined primarily by the central wavelength. In most cases, the observed bands have $\lambda_0 \approx 3.00$–3.06 μm for the ice band (see van de Bult and Greenberg 1985; Graham 1998; Dartois and d'Hendecourt 2001; Ishii *et al.* 1998; Whittet *et al.* 1983, 1996) and $\lambda_0 \approx 9.5$–9.8 μm for the silicate band (Bowey *et al.* 1998; Gillett and Forrest 1973; Capps *et al.* 1978; Smith *et al.* 2000). Spheroidal grains with axial ratios $a/b \approx 2$ or smaller produce bands with such a position of the center. Extremely prolate or oblate spheroids produce absorption bands with centers shifted greatly to the longer wavelengths (see Fig. 2) for any grain orientation. This is particularly noticeable for the silicate band whose center shifts to $\lambda_0 \approx 10.5$ μm. The central wavelength also shifts greatly with increasing thickness of the grain ice mantle, which confirms once again the existence of thin mantles. The polarizability of spheroids with large a/b is very high, which is also in conflict with the observational data. We see from Figs. 5e–5j that all the observed ice bands and most of the silicate bands can be explained in terms of grains (given their size) with axial ratios of $a/b = 2$ and 1.1.

4.4. Chemical Composition

Astronomical silicate (astrosil), a hypothetical material whose optical constants were constructed by Drain and Lee (1984) by considering the observed strength and shape of the silicate bands near 9.7 and 18 μm, is used most commonly as the grain core material. Which of the actual materials produce the observed absorption bands is still an unresolved question. In this paper, we used olivines, $Mg_{0.8}Fe_{1.2}SiO_4$ and $MgFeSiO_4$, to interpret the silicate bands. The model calculations of the absorption bands using $Mg_{0.8}Fe_{1.2}SiO_4$ are in best agreement with the observational data (Figs. 5 and 6). The observed silicate absorption bands with a small FWHM, $FWHM = 2.5$–2.6 μm, can be explained if we take $Mg_{0.8}Fe_{1.2}SiO_4$ and $MgFeSiO_4$ in equal amounts (see Fig. 5j). The central wavelength for some of the observed 9.7-μm silicate bands is near 9.4–9.6 μm, suggesting that various pyroxenes ($Mg_yFe_{1-y}SiO_3$) are also present in the objects. Pyroxenes produce narrower absorption bands than do olivines, but an ensemble of pyroxene and olivine grains can produce broader absorption bands than can an ensemble of grains with an olivine core alone. Increasing the fraction of pyroxene in the ensemble of grains with pyroxene and olivine cores leads to a shift in the central wavelength of the 9.7-μm silicate band to the shorter wavelengths and an increase in the band FWHM, in good agreement with the observational data (Bowey *et al.* 2003).

4.5. Orientation

In Figs. 5c–5j, the FWHMs of the two computed bands are plotted against the ratio of the optical depths at their centers for four types of grain orientation: random ($3D$), static, perfect Davies–Greenstein, and imperfect Davies–Greenstein orientations. We see from these figures that when

considering the absorption of the incident radiation by spheroids in terms of random orientation, we must take extremely prolate or oblate grains for good agreement with the observational data to be achieved, which is in conflict with the above conclusions about the grain shape. The other types of orientation mentioned above allow us to choose such values of $a/b \lesssim 2$ and $V_{\rm core}/V_{\rm total} \gtrsim 0.7$ at which the computed parameters of the modeled bands are comparable to their observed values. The figures were drawn for oblate spheroids; similar results are obtained for prolate particles.

The interpretation of the two bands (normalized to the center) for six observed protostars including all of the above constraints is illustrated in Fig. 6. We took the $Mg_{0.8}Fe_{1.2}SiO_4$ olivine as the core material of the grains producing these bands; the relative volume of the core is more than 0.7 in all cases, and the axial ratio a/b is 1.1 and 2. Here, we used the calculations performed in terms of the imperfect Davies–Greenstein orientation.

5. CONCLUSIONS

Our main results can be summarized as follows:

(1) We investigated the effect of dust grain size, shape, structure, and chemical composition on the parameters of two infrared absorption bands (the 3.1-μm water-ice and 9.7-μm silicate bands): the central wavelengths λ_0 of the two bands, their FWHMs, the ratio of the optical depths at the band centers $\tau(9.7\ \mu\text{m})/\tau(3.1\ \mu\text{m})$, and the polarization in the bands. We used the model of a confocal spheroid composed of a (silicate) core and a (water ice with impurities) mantle. The calculations were performed by considering various types of grain orientation: random, static, complete rotational, and partial rotational Davies–Greenstein orientations.

(2) An increase in the axial ratio a/b of the spheroid or in the thickness of the ice mantle was found to cause the central wavelength to shift greatly to the longer wavelengths. The ratio of the optical depths at the centers of the bands depends primarily on the thickness of the ice mantle and the grain size. The FWHMs of the bands are determined by the grain shape and the mantle thickness, increasing with a/b or $V_{\rm core}/V_{\rm total}$. The polarization in the bands increases rapidly with a/b; it depends weakly on the orientation parameter ξ at small a/b.

(3) The 3.1-μm ice and 9.7-μm silicate bands with parameters similar to their observed values in the spectra of protostellar sources and stars were shown to be obtained for an equivalent grain radius $r_V \lesssim 0.35\ \mu$m, an axial ratio $a/b \lesssim 2$, and a relative volume of the core material $V_{\rm core}/V_{\rm total} \gtrsim 0.7$. Extremely prolate or oblate spheroidal grains cannot be used to interpret the silicate bands, since the positions of their centers shift to $\lambda_0 \approx 10.5\ \mu$m, in conflict with most of the observational data. The ice mantles of the grains cannot be thick; the amount of the silicate material must be at least twice that of the ice material, since otherwise the silicate band will be strongly distorted by the 12-μm ice band, which is not the case in most of the observed protostellar objects.

(4) The $Mg_{0.8}Fe_{1.2}SiO_4$ olivine produces the 9.7-μm silicate bands with profiles, FWHMs, and positions of the centers similar to the observed ones. The $MgFeSiO_4$ silicate produces narrower bands. The broad bands with the centers near 9.5 or 9.6 μm can be explained by adding pyroxenes in the composition of the dust that absorbs the incident radiation.

(5) The orientation of dust grains is still an open question. When modeling the bands in terms of random orientation (with allowance made for the above conclusions), we obtained bands narrower than the observed bands. Static, perfect, and imperfect Davies–Greenstein orientations equally allow the model calculations to be compared with observations.

ACKNOWLEDGMENTS

I wish to thank Dr. Smith, who provided observational data, and T.E. Derviz and N.V. Voshchinnikov for helpful advice and remarks.

REFERENCES

1. P. Aannestad and E. Purcell, Annu. Rev. Astron. Astrophys. **11**, 309 (1973).
2. S. Asano and G. Yamamoto, Appl. Opt. **14**, 29 (1975).
3. C. Bohren and D. Huffman, *Absorption and Scattering of Light by Small Particles* (Wiley, New York, 1983; Mir, Moscow, 1986).
4. A. Boogert, A. Tielens, C. Ceccarelli, *et al.*, Astron. Astrophys. **360**, 683 (2000).
5. J. Bowey, A. Adamson, and D. Whittet, Mon. Not. R. Astron. Soc. **298**, 131 (1998).
6. J. Bowey, A. Adamson, and J. Yates, Mon. Not. R. Astron. Soc. **340**, 1173 (2003).
7. T. Brooke, K. Sellgren, and T. Geballe, Astrophys. J. **517**, 883 (1999).
8. R. Capps, F. Gillett, and R. Knacke, Astrophys. J. **226**, 863 (1978).
9. E. Dartois and L. d'Hendecourt, Astron. Astrophys. **365**, 144 (2001).
10. L. Davies and J. Greenstein, Astrophys. J. **114**, 206 (1951).
11. A. Z. Dolginov, Yu. N. Gnedin, and N. A. Silant'ev, *The Propagation and Polarization of Radiation in Space* (Nauka, Moscow, 1979) [in Russian].
12. B. Draine and H. Lee, Astrophys. J. **285**, 89 (1984).
13. V. G. Farafonov, Differ. Uravn. **19**, 1765 (1983).
14. V. G. Farafonov, Opt. Spektrosk. **76**, 79 (1994) [Opt. Spectrosc. **76**, 79 (1994)].

15. V. Farafonov, N. Voshchinnikov, and V. Somsikov, Appl. Opt. **35**, 5412 (1996).
16. G. E. Forsythe, M. A. Malcolm, and C. B. Moler, *Computer Methods for Mathematical Computations* (Prentice-Hall, Englewood Cliffs, N.J., 1977; Mir, Moscow, 1980).
17. E. Gibb, D. Whittet, and J. Chiar, Astrophys. J. **558**, 702 (2001).
18. E. Gibb, D. Whittet, W. Schutte, *et al.*, Astrophys. J. **536**, 347 (2000).
19. F. Gillett and W. Forrest, Astrophys. J. **179**, 483 (1973).
20. J. Graham, Astrophys. J. **492**, 213 (1998).
21. M. Greenberg, *Interstellar Grains* (Univ. of Chicago Press, Chicago, 1968; Mir, Moscow, 1970).
22. Th. Henning, V. Il'in, N. Krivova, *et al.*, Astron. Astrophys., Suppl. Ser. **136**, 405 (1999).
23. S. Hong and J. Greenberg, Astron. Astrophys. **88**, 194 (1980).
24. J. Hough, D. Whittet, S. Sato, *et al.*, Mon. Not. R. Astron. Soc. **241**, 71 (1989).
25. A. Il'in, Rev. Mex. Astron. Astrofis. **29**, 218 (1994).
26. M. Ishii, T. Nagata, Sh. Sato, *et al.*, Astron. J. **116**, 868 (1998).
27. S. Kim and P. Martin, Astrophys. J. **442**, 172 (1995).
28. H. Lee and B. Drain, Astrophys. J. **290**, 211 (1985).
29. P. Martin, *Cosmic Dust* (Oxford Univ. Press., Oxford, 1978).
30. P. Mezger, J. Mathis, and N. Panagia, Astron. Astrophys. **105**, 372 (1982).
31. M. I. Mishchenko, Pis'ma Astron. Zh. **15**, 694 (1989) [Sov. Astron. Lett. **15**, 299 (1989)].
32. J. O'Donnel, Astrophys. J. **437**, 262 (1994).
33. T. Onaka, Ann. Tokyo Astron. Observ. **18**, 1 (1980).
34. M. Palumbo, Astrophys. J. **479**, 839 (1997).
35. Y. Pendleton, A. Tielens, A. Tokunaga, and M. Bernstein, Astrophys. J. **513**, 294 (1999).
36. C. Rogers and P. Martin, Astrophys. J. **228**, 450 (1979).
37. C. Smith, C. Wright, D. Aitken, *et al.*, Mon. Not. R. Astron. Soc. **312**, 327 (2000).
38. V. V. Somsikov, Pis'ma Astron. Zh. **22**, 696 (1996) [Astron. Lett. **22**, 625 (1996)].
39. V. Somsikov and N. Voshchinnikov, Astron. Astrophys. **345**, 315 (1999).
40. L. Spitzer, Jr., *Physical Processes in Interstellar Medium* (Wiley, New York, 1978; Mir, Moscow, 1981).
41. T. Teixeira and J. Emerson, Astron. Astrophys. **351**, 292 (1999a).
42. T. Teixeira and J. Emerson, Astron. Astrophys. **351**, 303 (1999b).
43. A. Tielens, D. Wooden, L. Allamandola, *et al.*, Astrophys. J. **461**, 210 (1996).
44. C. van de Bult and M. Greenberg, Mon. Not. R. Astron. Soc. **214**, 289 (1985).
45. H. C. van de Hulst, *Light Scattering by Small Particles* (Wiley, New York, 1957; Inostrannaya Literatura, Moscow, 1961).
46. N. V. Voshchinnikov, Astron. Zh. **67**, 1061 (1990) [Sov. Astron. **34**, 535 (1990)].
47. N. V. Voshchinnikov, *Optics of Interstellar Dust* (S.-Peterburg. Gos. Univ., St. Petersburg, 1991) [in Russian].
48. N. V. Voshchinnikov, *Interstellar Dust* (Mir, Moscow, 1986) [in Russian].
49. N. Voshchinnikov, in *Optics of Cosmic Dust. Part I. Proceedings of NATO Advanced Research Workshop, Bratislava, Slovak Republik, 2001* (Kluwer, Dordrecht, 2002), Vol. 12, p. 1.
50. N. V. Voshchinnikov and V. G. Farafonov, Opt. Spektrosk. **58**, 135 (1985a) [Opt. Spectrosc. **58**, 81 (1985a)].
51. N. V. Voshchinnikov and V. G. Farafonov, Vestn. Leningr. Univ., Ser. Mat., Mekh., Astron. **8**, 86 (1985b).
52. N. V. Voshchinnikov and V. G. Farafonov, Opt. Spektrosk. **59**, 1250 (1985c) [Opt. Spectrosc. **59**, 750 (1985c)].
53. N. V. Voshchinnikov and V. G. Farafonov, Opt. Spektrosk. **60**, 1026 (1986) [Opt. Spectrosc. **60**, 635 (1986)].
54. N. V. Voshchinnikov and V. G. Farafonov, Vestn. Leningr. Univ., Ser. Mat., Mekh., Astron. **1**, 90 (1987).
55. N. Voshchinnikov and V. Farafonov, Astrophys. Space Sci. **204**, 19 (1993).
56. N. V. Voshchinnikov, A. E. Il'in, and V. B. Il'in, Astrofizika **24** (3), 523 (1986) [Astrophys. **24** (3), 299 (1986)].
57. D. Whittet, M. Bode, A. Longmore, *et al.*, Macmillan J. **102**, 218 (1983).
58. D. Whittet, R. Smith, A. Adamson, *et al.*, Astrophys. J. **458**, 363 (1996).
59. T. V. Zinov'eva, Astron. Astrophys. Trans. **22**, 51 (2003).
60. T. V. Zinov'eva, Opt. Spektrosk. **97**, 451 (2004) [Opt. Spectrosc. **97**, 433 (2004)].
61. T. V. Zinov'eva, Astron. Zh. **82**, 466 (2005) [Astron. Rep. **49**, 417 (2005)].

Translated by V. Astakhov

Astronomy Letters, Vol. 31, No. 7, 2005, pp. 474–486. Translated from Pis'ma v Astronomicheskiĭ Zhurnal, Vol. 31, No. 7, 2005, pp. 531–544.

Nonlinear Interaction between Alfvén and Acoustic-Gravity Waves in the Solar Atmosphere

M. Yu. Petukhov*

Lobachevsky State University, ul. Gagarina 23, Nizhni Novgorod, 603950 Russia

Received December 13, 2004

Abstract—Based on a plane-parallel isothermal model solar atmosphere permeated by a uniform magnetic field directed against the action of gravity, we considered the nonlinear interaction between vertically propagating Alfvén and acoustic-gravity waves. We established that Alfvén waves are efficiently generated at the difference and sum frequencies. We ascertained that no acoustic-gravity waves are formed at the corresponding combination frequencies. A horizontal magnetohydrodynamic wind whose direction changes with height was found to be formed in the solar atmosphere at zero difference frequency.

Key words: *Sun, atmosphere, waves, MHD.*

INTRODUCTION

At present, considerable attention is being given to studying the propagation and nonlinear generation of low-frequency acoustic-gravity waves (AGWs) and magnetohydrodynamic (MHD) waves in the solar atmosphere (Roberts 2000; Priest and Wood 1991). These studies are of great interest largely due to the development of physical mechanisms for the transfer of the mechanical energy radiated during the oscillations of the corresponding boundaries into the upper atmosphere.

Since the ambient density in the atmosphere decreases fairly sharply (in general, exponentially) with increasing height, the influence of nonlinear effects on the propagation of AGWs and MHD waves must be taken into account in certain height ranges due to an increase in the AGW and MHD wave oscillation velocity (Priest 1982; Fleck and Schmitz 1998; Sutmann and Ulmschneider 1995; Uchida and Kabuaki 1974; Cohen and Kulsrud 1974; Tsiklauri *et al.* 2001, 2002).

As was noted previously (Priest 1982), a nonlinear profile distortion is not typical of Alfvén waves, and their damping is low compared to AGWs. This is why the solar coronal heating by Alfvén waves, which can reach the coronal heights relatively freely because the nonlinearity and dissipation mechanisms noted above are weak, is considered by many authors as the most likely mechanism (Axford and McKenzie 1996; Ulmschneider *et al.* 1991; Narain and Ulmschneider 1996; Sakai *et al.* 2001). A major difficulty of this heating mechanism is the very weak dissipation of Alfvén waves as they propagate in the solar corona due to the low resistivity of the coronal plasma (Priest 1982). In this case, the nonlinear generation of acoustic waves by Alfvén waves is assumed to be the most likely mechanism of Alfvén wave energy transformation into the thermal energy of the surrounding plasma (Priest 1982; Wentzel 1974; Kudoh and Shibata 1999; M. Pekukhov and Yu. Petukhov 2002; Moriyasu *et al.* 2004); in turn, acoustic waves are affected fairly strongly by the nonlinearity and dissipation effects (Priest 1982).

Using the nonlinear equation (an analog of the scalar Cohen–Kulsrud–Burgers equation; Kennel *et al.* 1990) that was derived in the short-wavelength approximation and that describes the propagation of linearly polarized, spherical Alfvén waves in a solar coronal hole, Nakariakov *et al.* (2000) pointed out that the nonlinear propagation of an Alfvén wave not only contributes to the generation of acoustic waves, but is also accompanied by a nonlinear distortion of its profile. In fact, the formation of high Alfvén wave harmonics is attributable to the manifestation of a cubic nonlinearity (Nakariakov *et al.* 2000). As a result of the latter, the Alfvén waves during their nonlinear propagation in the solar corona turn into shock waves only at fairly large heights, ~ 5–$10 R_\odot$ (Nakariakov *et al.* 2000).

Here, it is important to note that the nonlinear distortion of the Alfvén wave profile followed by the formation of a shock front not only is accompanied by the formation of acoustic waves, but also, as follows from the results of our studies in terms of a quadratic nonlinearity of the medium presented below, is a direct

*E-mail: petukhov@rf.unn.ru

1063-7737/05/3107-0474$26.00

result of the nonlinear generation of acoustic waves by the Alfvén wave. An analysis of the latter assertion is one of our goals.

In this paper, we study the weakly nonlinear interaction of Alfvén waves with AGWs in terms of a plane-parallel isothermal solar model atmosphere. We consider the nonlinear generation of Alfvén waves and AGWs at the corresponding combination frequencies and the formation of an MHD flow at zero difference frequency.

FORMULATION OF THE PROBLEM

Let us consider the vertical propagation of Alfvén waves and AGWs in a plane-parallel isothermal atmosphere permeated by a uniform, vertically directed magnetic field. We assume that the z axis is directed vertically upward against the action of gravity whose free-fall acceleration is constant and equal to g and that the magnetic induction vector $\mathbf{B}_0 = (0, 0, B_0)$ is constant and directed vertically along the z axis. This atmosphere is characterized by the equilibrium distributions of density ρ_0 and pressure p_0 in height z

$$\rho_0 = \rho_{00}\exp(-2\eta z), \qquad (1)$$
$$p_0 = \frac{\rho_{00}c_\mathrm{s}^2}{\gamma}\exp(-2\eta z)$$

and by a constant adiabatic speed of sound $c_\mathrm{s} = \sqrt{\gamma p_0/\rho_0}$, the scale height $H = c_0^2/\gamma g$, and the Alfvén speed $c_\mathrm{a} = c_{\mathrm{a}0}\exp(\eta z)$. Here, $\rho_{00} = \rho_0(z = 0)$ is the density at the lower $z = 0$ atmospheric boundary, $\eta = 1/2H$, γ is the adiabatic index, $c_{\mathrm{a}0} = B_0/\sqrt{\mu_0\rho_{00}}$, and μ_0 is the magnetic constant.

We also assume that the Alfvén waves are excited vertically upward at the lower $z = 0$ atmospheric boundary at which there exist horizontal (along the x axis) magnetic field perturbations that lead to horizontal perturbations of the oscillation velocity with frequency ω_a and amplitude A_a:

$$v_x(z = 0) = A_\mathrm{a}\cos\omega_\mathrm{a}t, \quad -\infty < t < +\infty. \qquad (2)$$

In addition, the lower $z = 0$ atmospheric boundary executes time-independent vertical (along the z axis) oscillations with frequency ω_s and amplitude A_s:

$$v_z(z = 0) = A_\mathrm{s}\cos\omega_\mathrm{s}t, \quad -\infty < t < +\infty, \qquad (3)$$

which lead to the generation of AGWs. Note that the assumption about the existence of a lower atmospheric boundary at $z = 0$ with the specified boundary conditions (2) and (3) does not affect the generality of the problem, but serves only to properly describe the propagation of Alfvén waves and AGWs.

Here, it should also be noted that the model atmosphere used in this paper is most appropriate for the solar chromosphere for the following reasons: First, since the height of the chromosphere is much smaller than the solar radius, the approximation of a plane-parallel atmosphere stratified in the field of constant g is valid. Second, with the exception of the narrow chromosphere–corona transition layer in which the ambient temperature changes almost abruptly, we can also disregard the fact that the chromosphere is nonisothermal compared to the effects produced by the atmospheric stratification in the field of gravity. Indeed, at the distance of the middle solar chromosphere (its height is ~1000 km), the ambient temperature increases by less than a factor of 2, while the ambient density decreases by a factor of about e for every 200 km (see, e.g., Priest 1982). Third, since the magnetic field strength in the chromosphere decreases with height much more slowly than the ambient density, it is assumed to be constant. Nevertheless, the effects observed during the nonlinear propagation and interaction of Alfvén waves and AGWs, which are considered below, must also show up in the solar corona. However, we performed our numerical calculations using the typical parameters of the middle solar chromosphere.

To investigate the nonlinear interaction of Alfvén waves with AGWs, we use the following nonlinear equations:

$$\frac{\partial^2 v_x}{\partial t^2} - c_\mathrm{a}^2\frac{\partial^2 v_x}{\partial z^2} = -\frac{c_\mathrm{a}^2}{B_0}\frac{\partial^2}{\partial z^2}(B'v_z) - \frac{1}{\rho_0}\frac{\partial\rho'}{\partial t}\frac{\partial v_x}{\partial t} \qquad (4)$$
$$-\frac{\rho'}{\rho_0}\frac{\partial^2 v_x}{\partial t^2} - \frac{\partial v_z}{\partial t}\frac{\partial v_x}{\partial z} - v_z\frac{\partial^2 v_x}{\partial z\partial t},$$

$$\frac{\partial^2 v_z}{\partial t^2} - c_\mathrm{s}^2\frac{\partial^2 v_z}{\partial z^2} + \gamma g\frac{\partial v_z}{\partial z} = \frac{\gamma}{\rho_0}\frac{\partial}{\partial z}\left(p'\frac{\partial v_z}{\partial z}\right) \qquad (5)$$
$$-\frac{\rho'}{\rho_0}\frac{\partial^2 v_z}{\partial t^2} - 2v_z\frac{\partial^2 v_z}{\partial z\partial t} - \frac{\partial v_z}{\partial t}\frac{\partial v_z}{\partial z} - \frac{1}{2}\frac{c_\mathrm{a}^2}{B_0^2}\frac{\partial^2(B')^2}{\partial z\partial t}.$$

These equations were derived previously (M. Petukhov and Yu. Petukhov 2002) from the system of equations of ideal magnetohydrodynamics to quantities of the second order of smallness in perturbations of the hydrodynamic (ρ'/ρ_0, p'/p_0, v_z/c_0, v_x/c_a) and magnetic (B'/B_0) quantities and describe the vertical propagation of Alfvén waves (4) and AGWs (5). The perturbations of density $\rho'(v_z)$, pressure $p'(v_z)$, and magnetic field $B'(v_x)$ on the right-hand sides of Eqs. (4) and (5) are related to the vertical, v_z, and horizontal, v_x, oscillation velocity components by linear differential equations:

$$\frac{\partial\rho'}{\partial t} = \rho_0\left(\frac{1}{H} - \frac{\partial}{\partial z}\right)v_z, \qquad (6)$$
$$\frac{\partial p'}{\partial t} = \rho_0 c_\mathrm{s}^2\left(\frac{1}{\gamma H} - \frac{\partial}{\partial z}\right)v_z, \quad \frac{\partial B'}{\partial t} = B_0\frac{\partial v_x}{\partial z}.$$

The following conclusions can be reached by analyzing the appearance of the nonlinear equations for Alfvén waves (4) and AGWs (5):

(1) The vertical propagation of AGWs is accompanied by a nonlinear distortion of their profile; as was shown previously (M. Petukhov and Yu. Petukhov 2002), no Alfvén waves are formed at the corresponding difference and sum frequencies. Indeed, the first four terms on the right-hand (nonlinear) side of Eq. (5) are the quadratic products of the linear solutions for AGWs. Consequently, substituting the linear solutions for AGWs into the right-hand side of Eq. (5) gives rise to a "driving force" responsible for the generation of AGWs at the corresponding combination frequencies: the second harmonic and the difference and sum frequencies. In contrast, the right-hand side of Eq. (4) for Alfvén waves is the sum of the products, in our case, of the zero linear solution for Alfvén waves by the nonzero linear solution for AGWs, and, hence, it becomes equal to zero.

(2) In the approximation of quadratic nonlinearity under consideration and in the absence of AGWs, the Alfvén waves propagate without any nonlinear distortion of their profile; however, as M. Petukhov and Yu. Petukhov (2002) showed, AGWs are formed at the corresponding difference and sum frequencies. Indeed, assuming the existence only of Alfvén waves in the atmosphere and substituting their linear solutions into Eqs. (4) and (5), we obtain a zero right-hand nonlinear side of the equation for Alfvén waves and a nonzero right-hand nonlinear side of the equation for AGWs. In the latter case, only the fifth term on the right-hand side of Eq. (5) is responsible for the generation of the AGW combination frequencies.

(3) The absence of terms composed of the quadratic products of the linear solutions of Alfvén waves with AGWs on the right-hand side of Eq. (5) implies that the nonlinear interaction of Alfvén waves with AGWs does not contribute to the AGW generation at the combination frequencies. However, the corresponding terms exist on the right-hand side of Eq. (4); hence, the nonlinear interaction of Alfvén waves with AGWs must contribute to the generation of Alfvén waves at the difference and sum frequencies. Below, we focus our attention on the latter process.

Here, it should also be noted that Eqs. (4) and (5) allow the pattern of generation of the combination frequencies of Alfvén waves to be traced in higher orders of the perturbation theory. More specifically, as can be seen from Eq. (5), the propagation of an Alfvén wave must be accompanied by the formation of an AGW at the second harmonic. The latter, in turn, can interact with the primary Alfvén wave, contributing to the generation of high Alfvén wave harmonics in the third approximation (see Eq. (4)).

THE PARAMETRIC GENERATION OF ALFVÉN WAVES

Let us consider the parametric generation of Alfvén waves at the difference frequency $\Omega = \omega_a - \omega_s$ through the nonlinear interaction between an Alfvén wave with frequency ω_a and an AGW with frequency ω_s.

First, to elucidate some of the peculiar features that crop up during the nonlinear interaction of an Alfvén wave with an AGW, let us consider a homogeneous medium without dispersion ($g \to 0$). Given the boundary conditions (2) and (3), the linear solutions of the equations for Alfvén (4) and acoustic (5) waves then take the forms, respectively,

$$v_x^{(1)} = A_a \cos(\omega_a t - \alpha_a z), \qquad (7)$$
$$v_z^{(1)} = A_s \cos(\omega_s t - \alpha_s z),$$

where $\alpha_a = \omega_a/c_a$, $\alpha_s = \omega_s/c_s$, $c_a = \text{const}$.

Substituting expressions (7) into the right-hand side of Eq. (4) with the separation of the terms at the difference frequency and then solving the derived differential equation with the boundary condition

$$v_x^{(\Omega)}(z=0) = 0 \qquad (8)$$

yields the following simple solution for Alfvén waves at the difference frequency:

$$v_x^{(\Omega)} = D\left[\cos(\Omega t - \xi z) - \cos\left(\Omega t - \frac{\Omega}{c_a}\text{sgn}(\Omega\xi) z\right)\right], \qquad (9)$$

where

$$D = \frac{A_a A_s \left[w^2 + w + \frac{w}{\sigma}(1-2w) - \sigma\right]}{2c_s[(w-\sigma)^2 - (w-1)^2]}, \qquad (10)$$

$$w = \omega_a/\omega_s, \quad \xi = \alpha_a - \alpha_s, \quad \sigma = c_a/c_s,$$
$$\text{sgn}(\Omega\xi > 0) = 1, \quad \text{sgn}(\Omega\xi < 0) = -1.$$

An analysis of solution (9) suggests that, if one of the conditions

$$\begin{cases} \Omega > 0 \\ w > \sigma, \end{cases} \quad \begin{cases} \Omega < 0 \\ w < \sigma \end{cases} \qquad (11)$$

is satisfied, then the Alfvén wave at the difference frequency propagates in the same direction with the primary waves (along the z axis); if, however, one of the conditions

$$\begin{cases} \Omega < 0 \\ w > \sigma, \end{cases} \quad \begin{cases} \Omega > 0 \\ w < \sigma \end{cases} \qquad (12)$$

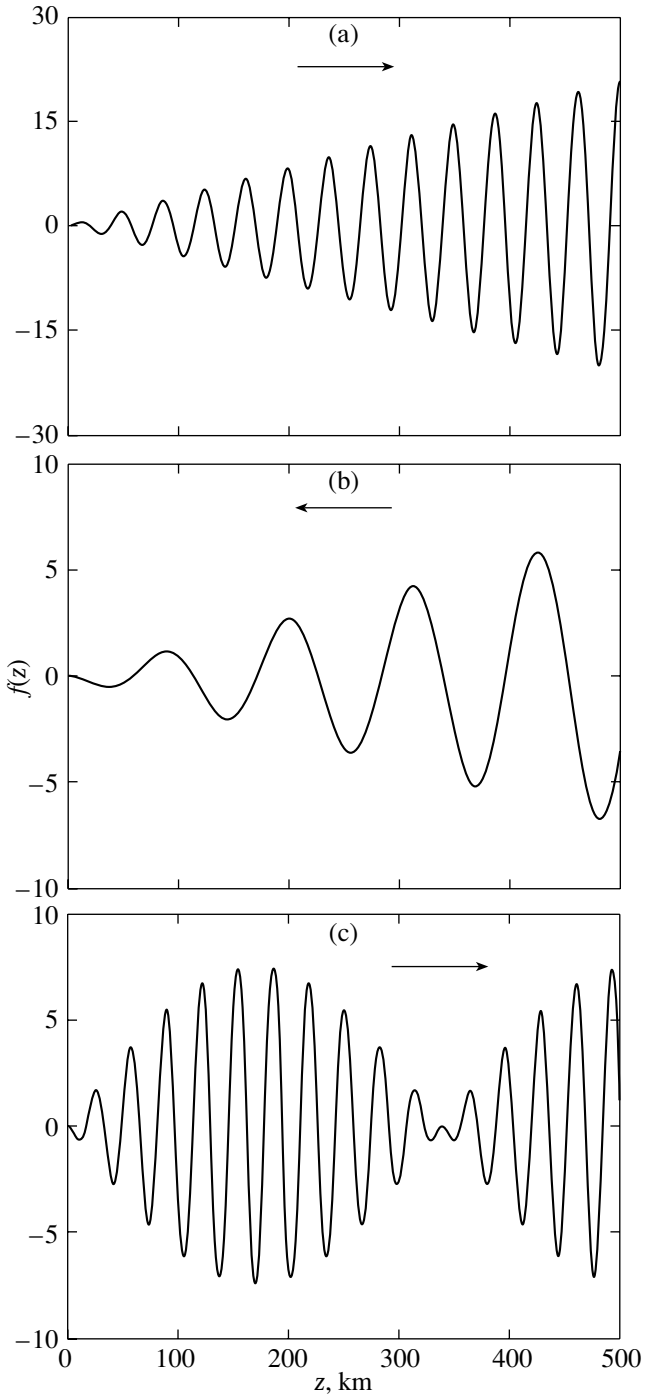

Fig. 1. Normalized function $f(z) = c_s v_x^{(\Omega)}(z, t = 0)/A_a A_s$, which characterizes the solution for the Alfvén waves at the difference frequency, versus height z at $\sigma =$ (a) 1, (b) 3, and (c) 0.9. For all dependences, $c_a = 6$ km s^{-1}, $\omega_a = 2$ rad s^{-1}, and $\omega_s = 1$ rad s^{-1}.

is satisfied, then the direction of propagation of the Alfvén wave at the difference frequency is opposite to that of the primary waves (against the z axis).

In addition, as might be expected (Rudenko and Soluyan 1975), when the Alfvén speed is equal to the speed of sound ($\sigma \to 1$), the phase synchronism conditions are satisfied,

$$\omega_a - \omega_s = \Omega, \qquad (13)$$
$$\alpha_a - \alpha_s = \frac{\Omega}{c_a},$$

and an increase in the amplitude of the solution pro-

portional to z is observed in the medium for the Alfvén wave at the difference frequency propagating in the same direction with the primary waves (see Fig. 1a). It can be shown that it is also possible to satisfy conditions (13) for the Alfvén waves at the difference frequency propagating against the z axis (see Fig. 1b) if the following equality holds:

$$w = (1+\sigma)/2. \tag{14}$$

In this case, however, the amplitude of the solution for the Alfvén waves at the difference frequency decreases linearly in the direction of their propagation (see Fig. 1b). If, alternatively, conditions (13) are not satisfied, then amplitude beats are observed in the medium (see Fig. 1c).

It should be noted that expressions (9) and (10) also describe the solution for the Alfvén waves at the sum frequency $\Omega_+ = \omega_\mathrm{a} + \omega_\mathrm{s}$ if the following substitutions are made in them:

$$\Omega \to \Omega_+, \quad \xi \to \xi_+ = \alpha_\mathrm{a} + \alpha_\mathrm{s}, \quad w \to -w. \tag{15}$$

In this case, it can be easily shown that, first, the Alfvén wave at the sum frequency always propagates along the z axis, and, second, for $\sigma \to 1$, a linear increase in the amplitude of the Alfvén waves at the sum frequency with height is observed, as with the Alfvén waves at the difference frequency.

After the above remarks, let us consider a stratified atmosphere in the field of gravity. In this case, the linear solutions for Alfvén waves and AGWs with the boundary conditions (2) and (3) are, respectively, (Ferraro and Plumpton 1958; Lamb 1932)

$$v_x^{(1)} = A_\mathrm{a}\cos(\omega_\mathrm{a}t)J_0(b_\mathrm{a}e^{-\eta z})/J_0(b_\mathrm{a}), \tag{16}$$

$$v_z^{(1)} = A_\mathrm{s}\begin{cases} e^{\eta z}\cos(\omega_\mathrm{s}t - \alpha_\mathrm{s}z), & \omega_\mathrm{s} > \omega_\mathrm{L} \\ e^{(1-\sqrt{1-\omega_\mathrm{s}^2/\omega_\mathrm{L}^2})\eta z}\cos(\omega_\mathrm{s}t), & \omega_\mathrm{s} < \omega_\mathrm{L}. \end{cases} \tag{17}$$

Here, $J_0(b_\mathrm{a}e^{-\eta z})$ is the zeroth-order Bessel function of the first kind, $b_\mathrm{a} = \beta\omega_\mathrm{a}/\omega_\mathrm{L}$, $\beta = c_\mathrm{s}/c_{\mathrm{a}0}$, $\alpha_\mathrm{s} = \eta\sqrt{\omega_\mathrm{s}^2/\omega_\mathrm{L}^2 - 1}$, and $\omega_\mathrm{L} = \eta c_\mathrm{s}$ is the Lamb frequency.

We see from the linear solution (17) that the AGWs are propagating ones if their frequency is higher than the Lamb frequency, $\omega_\mathrm{s} > \omega_\mathrm{L}$ (Lamb 1947). The linear solution (16) for Alfvén waves is described by the Bessel function $J_0(b_\mathrm{a}e^{-\eta z})$. This is an oscillating function, thereby describing explicitly the oppositely propagating Alfvén waves only at fairly high values of its argument, $b_\mathrm{a}e^{-\eta z} \gg 1$, and in the range of relatively small heights, $z \ll 2H$ (see, e.g., M. Petukhov and Yu. Petukhov 2002):

$$v_x^{(1)} \approx \frac{A_\mathrm{a}e^{\frac{\eta z}{2}}}{2\cos(b_\mathrm{a} - \pi/4)} \times \left\{\cos\left(\omega_\mathrm{a}t - b_\mathrm{a}\eta z + b_\mathrm{a} - \frac{\pi}{4}\right) + \cos\left(\omega_\mathrm{a}t + b_\mathrm{a}\eta z - b_\mathrm{a} + \frac{\pi}{4}\right)\right\}. \tag{18}$$

For $b_\mathrm{a}e^{-\eta z} \ll 1$ and as z increases, the Bessel function tends to a constant value ($J_0(0) = 1$), implying the formation of a peculiar oscillatory process in the atmosphere through the strong linear interaction between the oppositely propagating Alfvén waves (M. Petukhov and Yu. Petukhov 2002). In what follows, it is convenient to introduce the characteristic height z_H that corresponds to the first (last in height z) zero of the Bessel function $J_0(\bar{b}_1) = 0$,

$$z_H = 2H\ln\frac{b_\mathrm{a}}{\bar{b}_1}, \quad \bar{b}_1 \approx 2.4, \tag{19}$$

and that delimits the region of oscillations ($z < z_H$) with the region of a monotonic increase ($z > z_H$) as the function $J_0(b_\mathrm{a}e^{-\eta z})$ tends to unity. In particular, for the Alfvén wave frequency $\omega_\mathrm{a} = 0.15$ rad s^{-1} and typical parameters of the middle solar chromosphere, $c_\mathrm{s} = 10$ km s^{-1}, $c_{\mathrm{a}0} = 6$ km s^{-1}, $\gamma = 5/3$, $g = 275$ m s^{-1}, the characteristic height is $z_H \approx 660$ km.

In addition, as we see from (16), the zeroth-order Bessel function in the denominator of the solution for $v_x^{(1)}$ makes the resonant excitation of Alfvén waves possible at certain frequencies

$$\omega_\mathrm{a} = \bar{\omega}_n = \omega_\mathrm{L}\frac{\bar{b}_n}{\beta}, \quad n = 1, 2, \ldots; \tag{20}$$

the zeros of this function, $J_0(\bar{b}_n) = 0$, correspond to these frequencies at $b_\mathrm{a} = \bar{b}_n$.

Let us consider the parametric generation of Alfvén waves at the difference frequency through the nonlinear interaction of an Alfvén wave with an AGW. In this case, using (6), (16), and (17), we separate out the terms at the difference frequency on the right-hand side of Eq. (4) and then obtain the following solution for the oscillation velocity of the Alfvén waves at the difference frequency $v_x^{(\Omega)}$ in integral form by solving the derived differential equation:

$$v_x^{(\Omega)} = \mathrm{Re}\{e^{i\Omega t}[S_1(z)J_0(b_\Omega e^{-\eta z}) + S_2(z)Y_0(b_\Omega e^{-\eta z})]\}, \quad (21)$$

$$S_1(z) = \int q_1(z)dz + \overline{S_1}, \quad (22)$$

$$S_2(z) = \int q_2(z)dz + \overline{S_2}, \quad (23)$$

$$q_1(z) = \frac{G(z)Y_0(b_\Omega e^{-\eta z})}{\eta b_\Omega c_{a0}^2[J_0(b_\Omega e^{-\eta z})Y_1(b_\Omega e^{-\eta z}) - J_1(b_\Omega e^{-\eta z})Y_0(b_\Omega e^{-\eta z})]}, \quad (24)$$

$$q_2(z) = \frac{G(z)J_0(b_\Omega e^{-\eta z})}{\eta b_\Omega c_{a0}^2[J_1(b_\Omega e^{-\eta z})Y_0(b_\Omega e^{-\eta z}) - J_0(b_\Omega e^{-\eta z})Y_1(b_\Omega e^{-\eta z})]}, \quad (25)$$

$$G(z) = \frac{A_a A_s e^{2\eta z + i\alpha_s z}}{J_0(b_a)}\{G_1(z) - iG_2(z)\}, \quad (26)$$

$$G_1(z) = -J_1(b_a e^{-\eta z})e^{\eta z}\frac{c_{a0}^2 b_a \eta^2 \alpha_s}{\omega_a} + \alpha_s J_0(b_a e^{-\eta z})\left(\frac{c_{a0}^2 b_a^2 \eta^2}{\omega_a} - \frac{\omega_a}{2} + \frac{\omega_a^2}{2\omega_s}\right), \quad (27)$$

$$G_2(z) = \frac{\eta b_a}{2}J_1(b_a e^{-\eta z})\left\{\Omega e^{-\eta z} + \frac{c_{a0}^2 e^{\eta z}}{\omega_a}[\alpha_s^2 - \eta^2(1 - b_a^2 e^{-2\eta z})]\right\} - \frac{\Omega\omega_a\omega_L}{2\omega_s c_s}J_0(b_a e^{-\eta z}). \quad (28)$$

Here, $b_\Omega = \beta\Omega/\omega_L$; $Y_0(b_\Omega e^{-\eta z})$ and $Y_1(b_\Omega e^{-\eta z})$ are the Neumann functions of the zeroth and first orders, respectively; $\overline{S_1}$ and $\overline{S_2}$ are the constants to be determined from the boundary conditions. Whereas the first boundary condition is the absence of a difference-frequency wave on the $z = 0$ boundary surface (8), the second boundary condition

$$\overline{S_2} = 0 \quad (29)$$

follows from the impossibility of an increase in the solution for the oscillation velocity of the Alfvén waves at the difference frequency proportional to the zeroth-order Neumann function $Y_0(b_\Omega e^{-\eta z})$, because the energy conservation law is violated (Ferraro and Plumpton 1958).

Note that expressions (21)–(28) also describe the solution for the Alfvén waves at the sum frequency if the following substitutions are made in them:

$$\Omega \to \Omega_+, \quad \omega_s \to -\omega_s, \quad \alpha_s \to -\alpha_s, \quad (30)$$
$$b_\Omega \to b_{\Omega_+} = \beta\Omega_+/\omega_L.$$

The following conclusions can be drawn from the results of our numerical calculations (see Figs. 2–5) of the oscillation velocity for the Alfvén waves at the difference, $v_x^{(\Omega)}$ (Figs. 2 and 3), and sum, $v_x^{(\Omega_+)}$ (Figs. 4 and 5), frequencies:

(1) The nonlinear interaction of a propagating Alfvén wave with an AGW leads to an efficient generation of Alfvén waves at the difference and sum frequencies. Although the phase synchronism conditions (13) are not satisfied, the oscillation velocity amplitudes $|v_x^{(\Omega)}|$ and $|v_x^{(\Omega_+)}|$ increase rapidly with height z (see Figs. 2–5), much more rapidly than the linear solution (16) for Alfvén waves. The latter stems from the fact that even the amplitudes of the first three terms on the right-hand side of Eq. (4), which is the Alfvén wave generation source at the combination frequencies, increase with height more rapidly than the amplitude of the solution for any of the linear waves (16) and (17). In the special case of $z \ll z_H$, we can show using (4), (6), (16), (17), and (21) that the amplitude of the Alfvén waves at the difference frequency increases with height approximately as $\sim e^{2.25\eta z}$, while the amplitudes of the linear Alfvén waves (at $z < z_H$) and AGWs increase with height as $\sim e^{0.5\eta z}$ (see (18)) and $\sim e^{\eta z}$ (see (17)), respectively.

Here, it should be noted that the generation of Alfvén waves at the difference and sum frequencies is possible when an Alfvén wave interacts not only with a propagating AGW, but also with a nonpropagating AGW whose frequency is lower than the characteristic Lamb frequency ω_L. In this case, the oscillation velocity amplitude increases with height more slowly

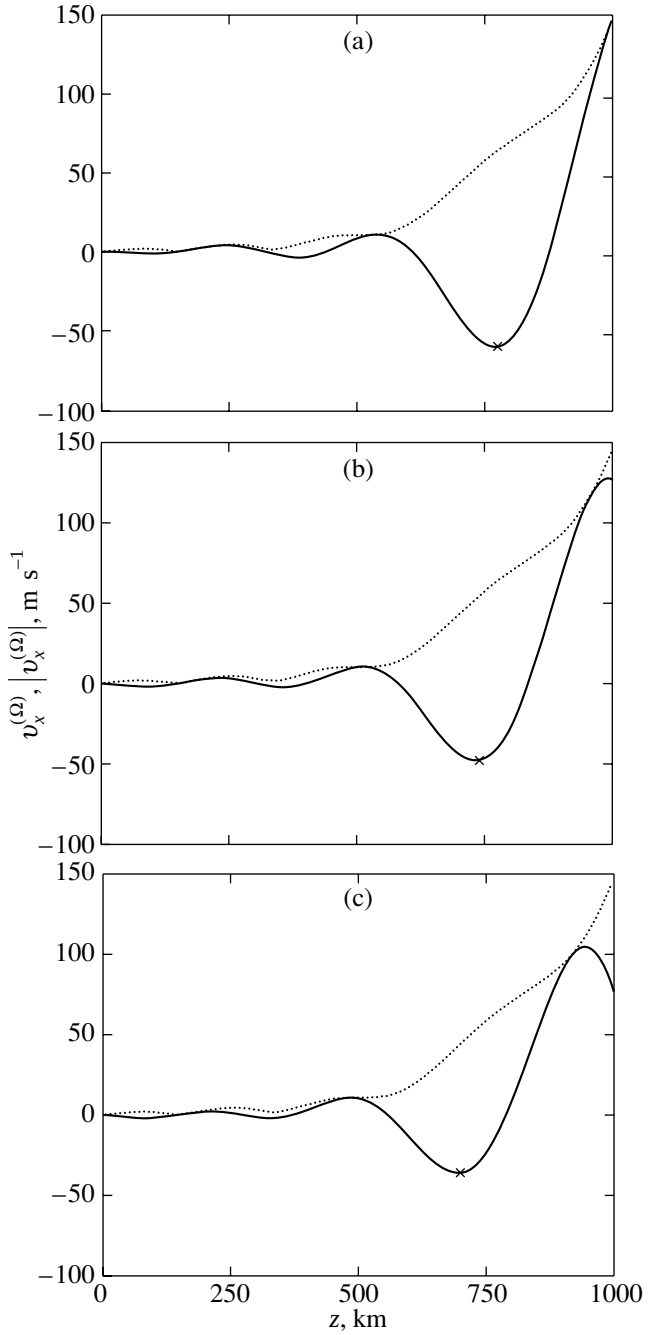

Fig. 2. Horizontal oscillation velocity $v_x^{(\Omega)}$ (solid lines) and its amplitude $|v_x^{(\Omega)}|$ (dotted lines) versus height z for the Alfvén waves at the difference frequency for $\omega_a = 0.15$ rad s^{-1} and $\omega_s = 0.1$ rad s^{-1} at times $t =$ (a) 0, (b) 10, and (c) 20 s. For all dependences, $A_a = 100$ m s^{-1}, $A_s = 100$ m s^{-1}, $\gamma = 5/3$, $g = 275$ m s^{-2}, $c_{a0} = 6$ km s^{-1}, and $c_s = 10$ km s^{-1}.

than that for the interaction with a propagating AGW. The latter is attributable to different growth rates of the oscillation velocity amplitude in the primary AGWs or, more specifically, to a slower increase in the oscillation velocity amplitude with height for a nonpropagating AGW than that for a propagating AGW (see (17)).

(2) As we see from Figs. 2 and 3, the Alfvén wave at the difference frequency propagating against (see the position of the minimum marked by a cross at various times in Fig. 2) and along (see Fig. 3) the z axis is clearly observed in the range of fairly large z ($z > z_H$) for $\omega_a > \omega_s$ and $\omega_a < \omega_s$, respectively. In contrast, in the range of fairly small heights ($z < z_H$), an interference pattern is formed in which the prop-

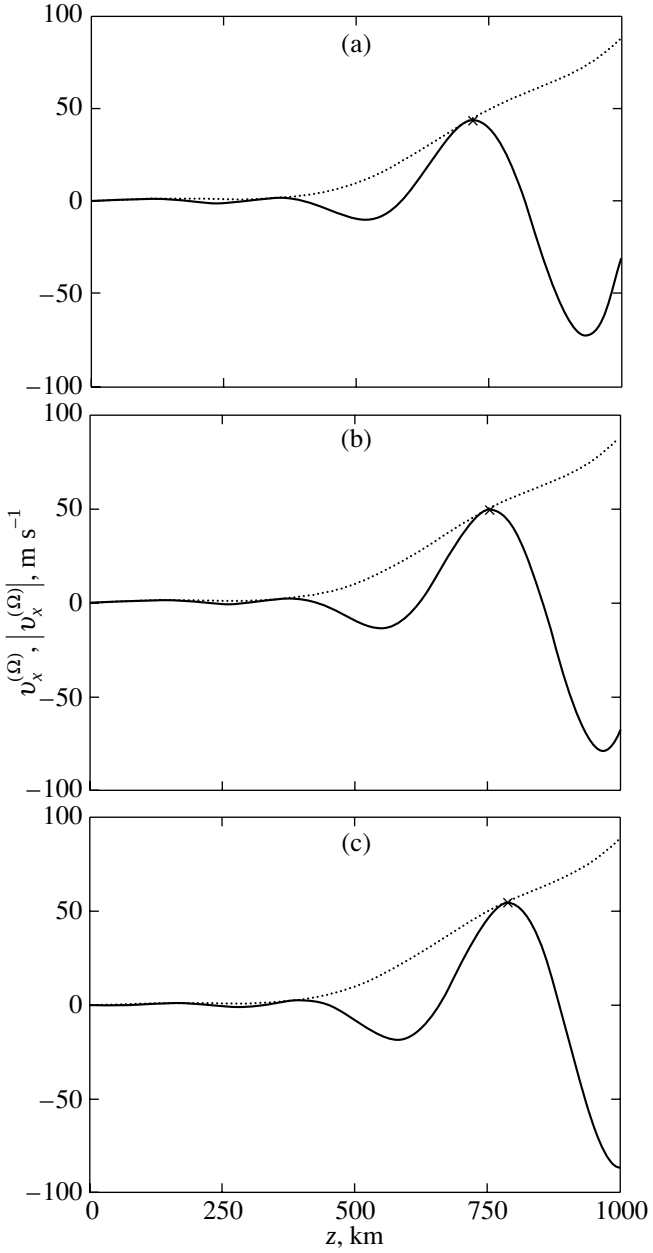

Fig. 3. Same as Fig. 2 for $\omega_a = 0.1$ rad s^{-1} and $\omega_s = 0.15$ rad s^{-1}.

agating Alfvén waves are more difficult to separate clearly (see Figs. 2 and 3)

The explanation of this behavior of the Alfvén waves at the difference frequency can be simplified significantly if we divide the total solution (21) for Alfvén waves into the forced solution

$$v_{x\text{forced}}^{(\Omega)} = \mathrm{Re}\left\{ e^{i\Omega t}\left[J_0(b_\Omega e^{-\eta z})\int^z q_1(z)dz \right.\right. \quad (31)$$
$$\left.\left. + Y_0(b_\Omega e^{-\eta z})\int^z q_2(z)dz \right]\right\}$$

and the eigensolution

$$v_{x\text{eigen}}^{(\Omega)} = \mathrm{Re}\{e^{i\Omega t}\overline{S_1}J_0(b_\Omega e^{-\eta z})\} \quad (32)$$

and introduce the wave vector of the linear Alfvén wave ζ. At large heights, $z \gg z_H$, the magnitude of the wave vector virtually approaches zero, $\zeta \to 0$, because the propagating linear Alfvén waves cannot be separated clearly; in contrast, at small heights, $z \ll z_H$, the following approximate equality is valid: $\zeta \approx b_a\eta$ (see (18)).

For $z > z_H$, the forced solution (31) describes two Alfvén waves at the difference frequency with

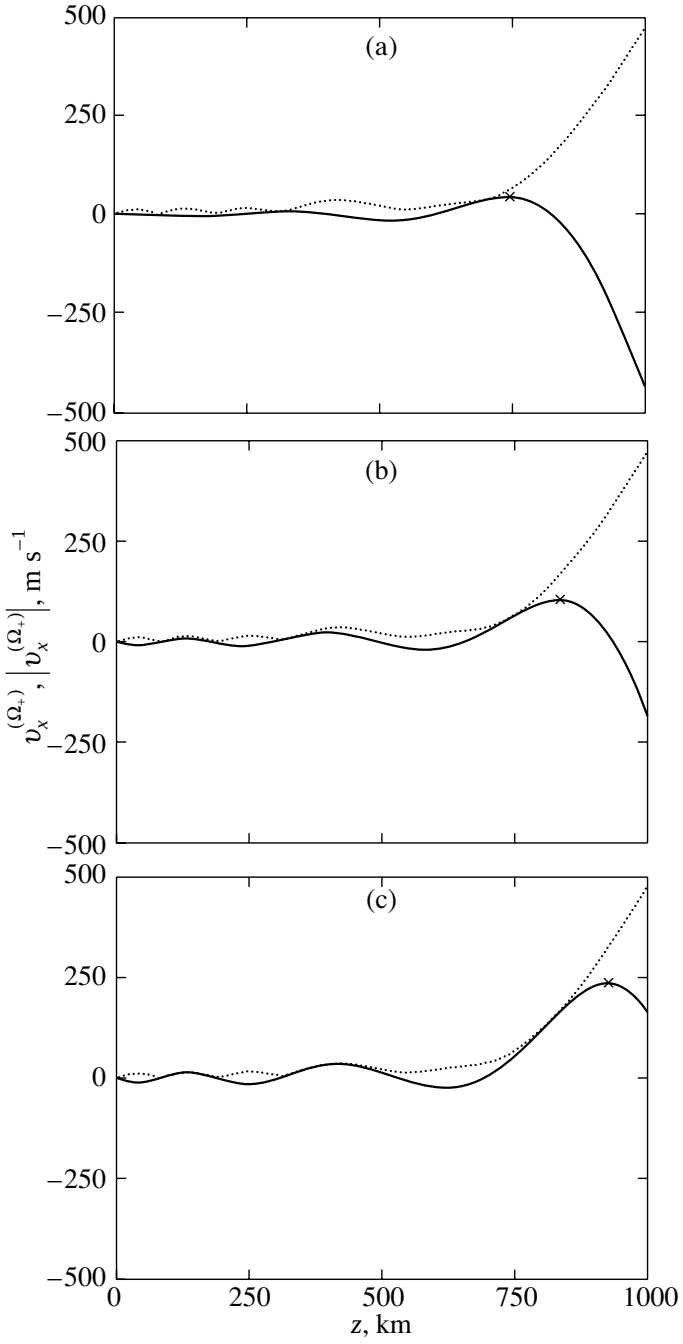

Fig. 4. Horizontal oscillation velocity $v_x^{(\Omega_+)}$ (solid lines) and its amplitude $|v_x^{(\Omega_+)}|$ (dotted lines) versus height z for the Alfvén waves at the sum frequency for $\omega_a = 0.15$ rad s^{-1} and $\omega_s = 0.1$ rad s^{-1} at times $t =$ (a) 0, (b) 3, and (c) 6 s. For all dependences, $A_a = 100$ m s^{-1}, $A_s = 100$ m s^{-1}, $\gamma = 5/3$, $g = 275$ m s^{-2}, $c_{a0} = 6$ km s^{-1}, and $c_s = 10$ km s^{-1}.

phases $\Omega t + (\alpha_s \pm \zeta)z$, which degenerate into one wave with phase $\Omega t + \alpha_s z$ in the range of fairly large heights, $z > z_H$ ($\zeta \to 0$); in contrast, the eigensolution (32) makes almost no contribution to the total solution (21) (see Fig. 6). Therefore, for $z > z_H$, in fact, there is only one Alfvén wave at the difference frequency that propagates against or along the z axis, depending on the satisfaction of the conditions $\omega_a > \omega_s$ or $\omega_a < \omega_s$, respectively (see Figs. 2 and 3). By analogy, we can show that the Alfvén wave at the sum frequency for $z > z_H$ always propagates along the z axis for any relation between the frequencies of the primary waves (see Figs. 4 and 5).

For $z < z_H$, both solutions, (31) and (32) (see Fig. 6), contribute to the overall interference pattern of the Alfvén waves at the difference frequency. More

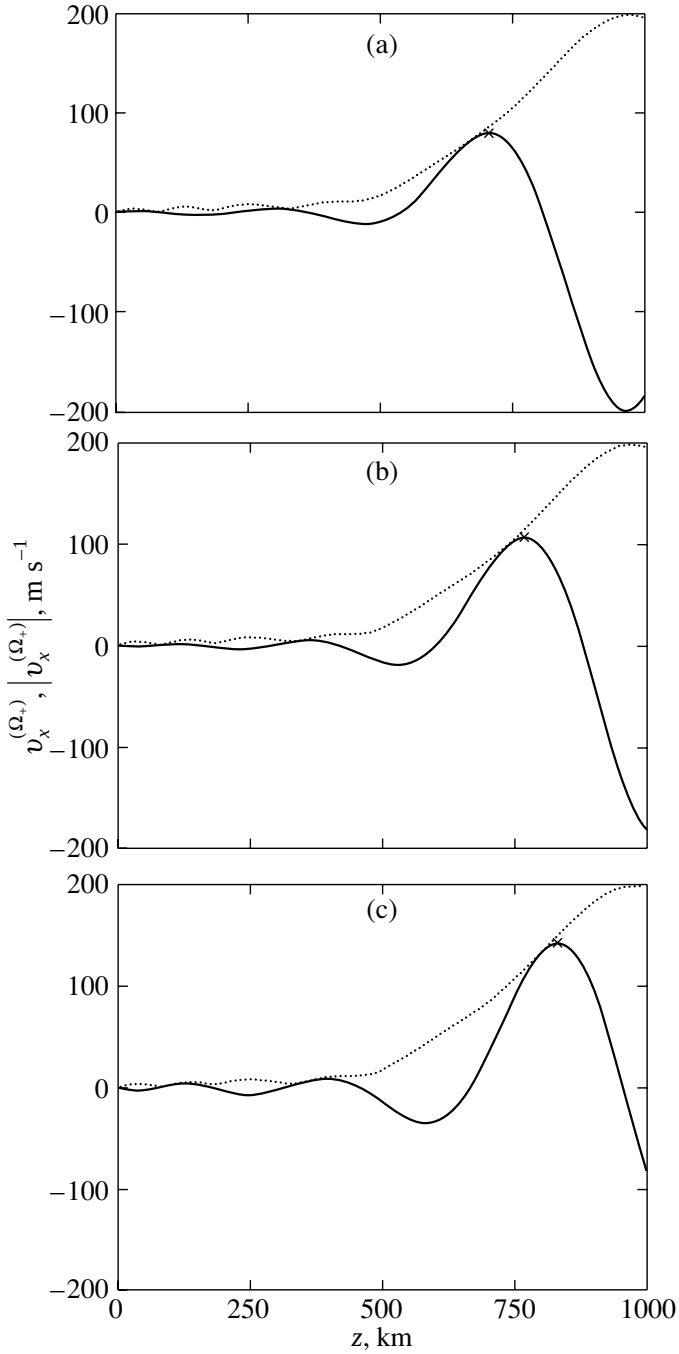

Fig. 5. Same as Fig. 4 for $\omega_a = 0.1$ rad s^{-1} and $\omega_s = 0.15$ rad s^{-1}.

specifically, the forced solution (31) describes two Alfvén waves at the difference frequency with the corresponding phases $\Omega t + (\alpha_s \pm \zeta)z$ that can propagate both in the same direction for $\zeta < \alpha_s$ (against the z axis) and in the opposite directions (if $\zeta > \alpha_s$). By analogy with (18), the eigensolution (32) for small z describes two oppositely propagating Alfvén waves at the difference frequency. This is why the oppositely traveling waves are more difficult to separate clearly from the results of our numerical solution for the oscillation velocity of the Alfvén waves at the difference frequency in the range $z < z_H$. Similar reasoning is also valid for the Alfvén waves at the sum frequency, since the forced solution in this case describes two Alfvén waves with phases $\Omega_+ t - (\alpha_s \pm \zeta)z$.

(3) Since expression (21) for the oscillation velocity does not become identically equal to zero when

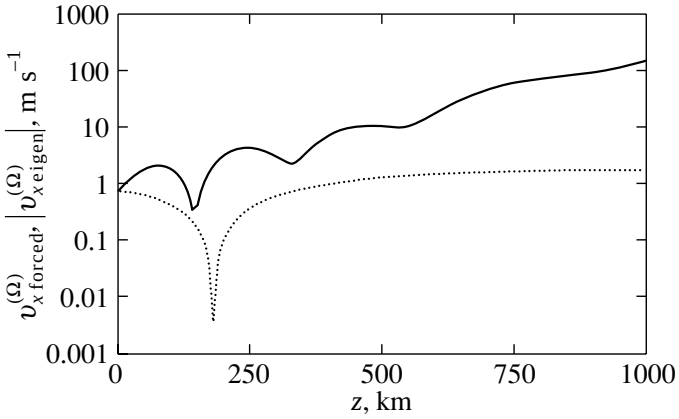

Fig. 6. Amplitudes of the forced solution $|v^{(\Omega)}_{x\mathrm{forced}}|$ (solid line) and the eigensolution $|v^{(\Omega)}_{x\mathrm{eigen}}|$ (dotted line) versus height z for the Alfvén waves at the difference frequency for $\omega_\mathrm{a} = 0.15$ rad s^{-1}, $\omega_\mathrm{s} = 0.1$ rad s^{-1}, $A_\mathrm{a} = 100$ m s^{-1}, $A_\mathrm{s} = 100$ m s^{-1}, $\gamma = 5/3$, $g = 275$ m s^{-2}, $c_\mathrm{s} = 10$ km s^{-1}, and $c_{\mathrm{a}0} = 6$ km s^{-1}.

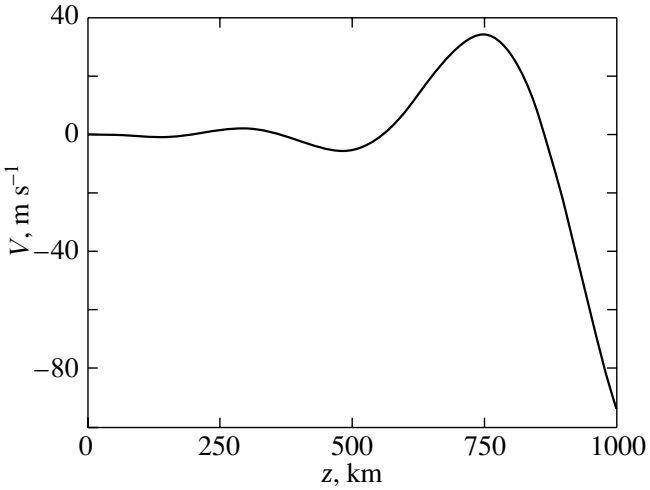

Fig. 7. Horizontal flow velocity $V(z)$ versus height z for $\omega_\mathrm{a} \to \omega_\mathrm{s} = 0.1$ rad s^{-1}, $A_\mathrm{a} = 100$ m s^{-1}, $A_\mathrm{s} = 100$ m s^{-1}, $\gamma = 5/3$, $g = 275$ m s^{-2}, $c_{\mathrm{a}0} = 6$ km s^{-1}, and $c_\mathrm{s} = 10$ km s^{-1}.

$\Omega \to 0$ (see Fig. 7),

$$V(z) = v_x^{(\Omega)}(z,t)\Big|_{\Omega\to 0} \neq 0, \qquad (33)$$

the latter implies the formation of a horizontal MHD flow in the atmosphere. We see from Fig. 7 that the direction of the horizontal flow changes with height. Since the flow is actually formed by two Alfvén waves with phases $(\Omega t + (\alpha_\mathrm{s} \pm \zeta)z)|_{\Omega\to 0}$, the variations in the direction of the flow velocity with height are determined by their respective wave numbers $\alpha_\mathrm{s} \pm \zeta$. For $z > z_H$, the wave number of the linear Alfvén waves ζ approaches zero; therefore, the variations in the direction of the horizontal flow at large heights are actually determined by the wave number α_s of the primary AGW. The flow velocity, along with the Alfvén wave amplitude for $\Omega \neq 0$, increases with height, on average, fairly rapidly (see Fig. 7).

Here, it should be noted that the magnitude of the MHD flow approaches zero for a homogeneous medium ($g \to 0$) (see (9)). Thus, the physical cause of the formation of such an MHD flow can be treated as a parametric effect of an inhomogeneous medium on the nonlinear interaction of an Alfvén wave with an AGW at zero difference frequency. Since the parameters of the medium vary nonperiodically both in time (with a zero frequency) and in space (the equilibrium density and pressure decrease exponentially with height), from the viewpoint of the parametric effect, the medium can efficiently contribute to the generation of zero-frequency waves whose wave spatial scale (wave number) is also equal to zero. Such conditions are achieved during the nonlinear

vertical propagation of AGWs in the atmosphere; as M. Petukhov and Yu. Petukhov (2003) showed, a vertically downward-directed acoustic wind (flow) whose velocity increases exponentially with height is formed in the atmosphere at zero difference frequency. In the case considered here, the wave at zero difference frequency has a nonzero wave number. The latter is responsible for the inefficient parametric effect of the medium on the generation of Alfvén waves at zero difference frequency, which manifests itself in the form of spatial oscillations of the flow velocity along the vertical of the atmosphere.

In addition, in both this and our previous paper (M. Petukhov and Yu. Petukhov 2003), the flow is formed only by propagating (energy-transferring) waves. Indeed, as the AGW frequency tends to the Lamb frequency, $\omega_s \to \omega_L$, the AGW wave number become equal to zero, $\alpha_s \to 0$, and, as can be easily seen from expressions (21)–(28), the flow velocity also approaches zero, $V \to 0$. The latter implies that the flow is associated with the wave energy transfer in the medium.

Here, it should also be noted that the formation of such a plane-stratified flow does not give rise to an instability in the atmosphere, because periodic (in space) variations of the flow velocity lead to the corresponding curvature of the field lines of an initially vertically directed uniform magnetic field. Consequently, the forces of magnetic tension that are opposite to the flow direction and that hinder the growth of instability in the atmosphere along the horizontal axis must arise. However, the method of a specified field used here and the method of successive approximations do not allow the above force of magnetic tension that must hinder the growth of the flow to be clearly separated, since, in fact, we assume that the vertical magnetic field component is constant and equal to B_0 at any point in space, i.e., we disregard the magnetic field being curved under the effect of the flow. Thus, the above reasoning leads us to conclude that the initial stage of the simultaneous propagation and nonlinear interaction of an Alfvén wave and an AGW, $0 \le t \le t_*(z)$, at zero difference frequency in the actual atmosphere is accompanied by the formation of plane-stratified MHD flows in it. In the course of time, a magnetic field configuration such that the driving force of the flow at a certain time $t_*(z)$ will be offset by the tension of magnetic field lines will be established in the atmosphere, and the flow will disappear. However, $t_*(z)$ cannot be determined using the formulation of the problem under consideration and the method of its solution, since this requires solving a self-consistent problem.

CONCLUSIONS

Below, we formulate our main results and the conclusions that follow from them.

Based on a plane-parallel isothermal solar model atmosphere permeated by a uniform vertically directed magnetic field, we investigated the pattern of nonlinear interaction between Alfvén waves and vertically propagating AGWs.

We established that the nonlinear interaction of an Alfvén wave with a propagating AGW leads to an efficient generation of Alfvén waves at the difference and sum frequencies; in this case, no AGWs are formed at the corresponding combination frequencies. We pointed out that Alfvén waves could also be formed at the combination frequencies during the nonlinear interaction of an Alfvén wave with a nonpropagating AGW, but this process is less efficient.

The nonlinear generation of Alfvén waves at both the difference and sum frequencies was shown to be accompanied by the formation of a fairly complex interference wave pattern in the atmosphere. We specified the range of atmospheric heights where the field of Alfvén waves at the corresponding combination frequency is determined by one wave that propagates against or in the direction of the action of gravity, depending on the frequency ratio of the primary waves.

We found that a horizontal MHD flow is formed in the atmosphere at zero difference frequency. The direction of the flow was shown to change with height.

Thus, our studies suggest that even in the case of a quadratic nonlinearity of the medium, the propagation of an Alfvén wave is accompanied by a nonlinear distortion of its profile. Indeed, the propagation of an Alfvén wave is accompanied by the formation of an AGW at the second harmonic (see M. Petukhov and Yu. Petukhov 2002); interacting with the primary Alfvén wave, the latter, in turn, leads to the generation of Alfvén wave combination frequencies in the third approximation. At the same time, the interaction of an Alfvén wave with initially existing AGWs in the solar atmosphere gives rise to new Alfvén wave harmonics in the second order of the perturbation theory. Therefore, the distance traveled by an Alfvén wave before the formation of a shock front decreases appreciably compared to that obtained by Nakariakov *et al.* (2000).

ACKNOWLEDGMENTS

This work was supported by the Russian Foundation for Basic Research (project no. 02-02-17374), the Leading Scientific Schools of Russia program (project nos. 838.2003.2 and 1483-2003.2), and the Universities of Russia program.

REFERENCES

1. W. I. Axford and J. F. McKenzie, *Magnetodynamic Phenomena in the Solar Atmosphere—Prototypes of Stellar Magnetic Activity,* Ed. by Y. Uchida, T. Kosugi, and H. S. Hudson (Kluwer, Dordrecht, 1996), p. 115.
2. R. H. Cohen and R. M. Kulsrud, Phys. Fluids **17**, 2215 (1974).
3. V. C. A. Ferraro and C. Plumpton, Astrophys. J. **127**, 459 (1958).
4. B. Fleck and F. Schmitz, Astron. Astrophys. **337**, 487 (1998).
5. C. F. Kennel, R. D. Blandford, and C. C. Wu, Phys. Fluids B **2**, 253 (1990).
6. K. Kudoh and K. Shibata, Astrophys. J. **514**, 493 (1999).
7. H. Lamb, *Hydrodynamics,* 6th ed. (Cambridge Univ. Press, Cambridge, 1932; Gostekhizdat, Moscow, 1947).
8. S. Moriyasu, T. Kudoh, T. Yokoyama, and K. Shibata, Astrophys. J. **601**, 107 (2004).
9. V. M. Nakariakov, L. Ofman, and T. D. Arber, Astron. Astrophys. **353**, 741 (2000).
10. U. Narain and P. Ulmschneider, Space Sci. Rev. **75**, 453 (1996).
11. M. Yu. Petukhov and Yu. V. Petukhov, Pis'ma Astron. Zh. **28**, 382 (2002) [Astron. Lett. **28**, 335 (2002)]; Pis'ma Astron. Zh. **29**, 720(E) (2003) [Astron. Lett. **29**, 640(E) (2003)].
12. M. Yu. Petukhov and Yu. V. Petukhov, Pis'ma Astron. Zh. **29**, 137 (2003) [Astron. Lett. **29**, 116 (2003)].
13. E. R. Priest, *Solar Magnetohydrodynamics* (Reidel, Dordrecht, 1982; Mir, Moscow, 1985).
14. E. R. Priest and A. W. Wood, *Advances in Solar System Magnetohydrodynamics,* Ed. by E. R. Priest and A. W. Wood (Cambridge Univ. Press, Cambridge, 1991; Mir, Moscow, 1995).
15. B. Roberts, Sol. Phys. **193**, 139 (2000).
16. O. V. Rudenko and S. I. Soluyan, *Theoretical Foundations of Nonlinear Acoustics* (Nauka, Moscow, 1975; Consultants Bureau, New York, 1977).
17. J. L. Sakai, R. Minamizuka, T. Kawata, and N. F. Cramer, Astrophys. J. **550**, 1075 (2001).
18. G. Sutmann and P. Ulmschneider, Astron. Astrophys. **294**, 241 (1995).
19. D. Tsiklauri, T. D. Arber, and V. M. Nakariakov, Astron. Astrophys. **379**, 1098 (2001).
20. D. Tsiklauri, T. D. Arber, and V. M. Nakariakov, Astron. Astrophys. **395**, 285 (2002).
21. Y. Uchida and O. Kabuaki, Sol. Phys. **35**, 451 (1974).
22. P. Ulmschneider, E. R. Priest, and R. Rosner, *Mechanisms of Chromospheric and Coronal Heating* (Springer, Berlin, 1991).
23. D. J. Wentzel, Sol. Phys. **39**, 129 (1974).

Translated by V. Astakhov

Astronomy Letters, Vol. 31, No. 7, 2005, pp. 487–493. Translated from Pis'ma v Astronomicheskiĭ Zhurnal, Vol. 31, No. 7, 2005, pp. 545–552.

Particular Solutions of the Singly Averaged Hill Problem

M. A. Vashkov'yak*

Keldysh Institute of Applied Mathematics, Russian Academy of Sciences, Miusskaya pl. 4, Moscow, 125047 Russia

Received February 22, 2005

Abstract—We consider the case of averaging the perturbing function of the Hill problem over the fastest variable, the mean anomaly of the satellite. In integrable special cases, we found solutions to the evolutionary system of equations in elements. © *2005 Pleiades Publishing, Inc.*

Key words: *celestial mechanics, averaged Hill problem, orbital evolution.*

INTRODUCTION. FORMULATION OF THE PROBLEM

The model of a singly averaged restricted circular problem of three material points was suggested by N.D. Moiseev in two of its last papers (Moiseev 1945a, 1945b). In the celestial mechanics literature, this model is referred to as Moiseev's scheme (Grebenikov and Ryabov 1971; Abalakin *et al.* 1976). This scheme is most suitable for satellite problems: In introducing simplifications, it eliminates only the fastest variable, the mean anomaly of the satellite, while retaining the time functions attributable to the motion of the perturbing body in the equations. In the commonly used model of a *doubly* averaged problem, the influence of the perturbing body during its revolution cannot be taken into account in principle. At the same time, such periodic perturbations play a prominent role in the motion of distant satellites of the giant planets, in particular, Jupiter's satellite S/2001 J10 (Euporie) (Vashkov'yak and Teslenko 2005).

In the papers mentioned above, Moiseev gave the most general expression for the singly averaged perturbing function for the model considered here, revealed the existence of the first two integrals for the evolutionary system of differential equations in elements, and pointed out an integrable case of the problem: satellite orbits lying in the plane of motion of the perturbing body. Since the singly averaged problem under consideration is not integrable in the general (three-dimensional) formulation, it seems natural first to analyze its particular solutions (integrable cases). This is the goal of our work.

Let us consider the problem of the motion of a planetary satellite perturbed by the attraction from a distant external body (Sun). Denote the planetocentric Keplerian orbital elements of the satellite, i.e., the semimajor axis, eccentricity, inclination, argument of the pericenter, longitude of the ascending node, and the mean anomaly, by a, e, i, ω, Ω, and M, respectively. The angular variables are referred to the plane of motion of the perturbing body and to a fixed direction in this plane. The perturbing body is assumed to move in a circular orbit of radius a'. Let us also introduce the notation for the mean motions of the satellite, $n = \dfrac{\sqrt{\mu}}{a^{3/2}}$, and the perturbing body, $n' = \dfrac{\sqrt{\mu+\mu'}}{a'^{3/2}}$, as well as for the dimensionless parameter of the problem,

$$\nu = \frac{n'}{n\beta}, \tag{1}$$

where

$$\beta = \frac{3\mu' a^3}{16\mu a'^3}, \tag{2}$$

μ and μ' are the products of the gravitational constants by the masses of the planet and the perturbing body, respectively. Disregarding the small ratio μ/μ', which does not exceed $\sim$0.001 for the planets in the Solar system, we can assume that

$$n'^2 \approx \frac{\mu'}{a'^3}, \quad \beta \approx \frac{3n'^2}{16n^2}, \quad \nu \approx \frac{16n}{3n'}.$$

Since the ratio of the mean motions, n'/n, for the distant satellites of the giant planets known to date does not exceed $\sim$0.16, we find that $\nu > 100/3 = 33.3333\ldots$ in actual satellite systems. The hypothetically acceptable lower limit for ν can be determined from the relationship of this parameter to the semimajor axis of the satellite orbit and the radius of the

*E-mail: vashkov@keldysh.ru

planet's Hill sphere with respect to the perturbing body (Sun),

$$a_{\rm H} = a' \left[\frac{\mu}{3(\mu+\mu')}\right]^{1/3}. \quad (3)$$

This relationship is

$$\frac{a}{a_{\rm H}} = 4\left[\frac{4(\mu'+\mu)^2}{3\nu^2\mu'^2}\right]^{1/3} \approx 4\left(\frac{4}{3}\right)^{1/3}\nu^{-2/3}. \quad (4)$$

Assuming that the restricted planetocentric motion of the satellite must be within the Hill sphere, i.e., $a(1+e) \le a_{\rm H}$, we obtain $\nu_{\min} \approx 32(2/3)^{1/2} \approx 26.1$ at $e = 1$ and $\nu_{\min} \approx 16(3)^{-1/2} \approx 9.2$ at $e = 0$.

In place of the time t, we use the "normalized" time as an independent variable,

$$\tau = \beta n(t - t_0), \quad (5)$$

where t_0 is the initial time.

Note that the longitude of the ascending node of the satellite orbit, Ω, appears in the averaged perturbing function R only as a combination with the mean longitude of the perturbing body,

$$\lambda' = \lambda'_0 + n'(t - t_0) = \lambda'_0 + \nu\tau, \quad (6)$$

where λ'_0 is the initial value of λ' at $\tau = 0$. Denoting this combination by

$$\tilde{\Omega} = \Omega - \lambda'_0 - \nu\tau, \quad (7)$$

let us write the perturbing function R averaged over the mean anomaly of the satellite and normalized to the factor $\mu\beta/a$,

$$V = \frac{1}{2\pi}\int_0^{2\pi} R dM \quad (8)$$

in the Hill approximation ($a(1+e) \ll a'$),

$$\begin{aligned} V_{\rm H} = {} & 4/3 + 2(e^2 - \sin^2 i) \\ & + e^2\sin^2 i(5\cos 2\omega - 3) \\ & - 10e^2\cos i\sin 2\omega\sin 2\tilde{\Omega} \\ & + [2\sin^2 i + 10e^2\cos 2\omega \\ & + e^2\sin^2 i(3 - 5\cos 2\omega)]\cos 2\Omega, \end{aligned} \quad (9)$$

so that

$$V = V_{\rm H} + {\rm O}(a/a')^3. \quad (10)$$

As was established by Moiseev (1945b), the evolutionary system of differential equations for the singly averaged restricted circular problem of three material points admits of the first two integrals:

$$a = {\rm const}, \quad (11)$$

$$V + \nu\sqrt{1-e^2}\cos i = {\rm const}. \quad (12)$$

In the (Hill) approximation used, integral (12) can be written in explicit form as

$$V_{\rm H} + \nu\sqrt{1-e^2}\cos i = {\rm const}, \quad (13)$$

where the function $V_{\rm H}$ is defined by formula (9).

The evolutionary equations for the singly averaged Hill problem in the notation used are

$$\begin{aligned} \frac{da}{d\tau} &= 0, \\ \frac{de}{d\tau} &= 10e\sqrt{1-e^2}[\sin^2 i\sin 2\omega \\ &+ (2 - \sin^2 i)\sin 2\omega\cos 2\tilde{\Omega} + 2\cos i\cos 2\omega\sin 2\tilde{\Omega}], \\ \frac{di}{d\tau} &= -\frac{2\sin i}{\sqrt{1-e^2}}\{5e^2\cos i\sin 2\omega(1 - \cos 2\tilde{\Omega}) \\ &- [2 + e^2(3 + 5\cos 2\omega)]\sin 2\tilde{\Omega}\}, \\ \frac{d\omega}{d\tau} &= \frac{2}{\sqrt{1-e^2}}\{4 + e^2 - 5\sin^2 i \\ &+ 5(\sin^2 i - e^2)\cos 2\omega \\ &+ 5(e^2 - 2)\cos i\sin 2\omega\sin 2\tilde{\Omega} \\ &+ [5(2 - e^2 - \sin^2 i)\cos 2\omega - 2 \\ &- 3e^2 + 5\sin^2 i]\cos 2\tilde{\Omega}\}, \\ \frac{d\tilde{\Omega}}{d\tau} &= -\nu - \frac{2}{\sqrt{1-e^2}}\{[2 + e^2(3 \\ &- 5\cos 2\omega)]\cos i(1 - \cos 2\tilde{\Omega}) - 5e^2\sin 2\omega\sin 2\tilde{\Omega}\}. \end{aligned} \quad (14)$$

In the next section, we analyze particular solutions of system (14).

A PLANE PARTICULAR SOLUTION

As was established by Moiseev (1945a), a particular solution ($\sin i = 0$, $\dfrac{di}{d\tau} = 0$) also exists in the general case of the singly averaged problem with the "total" perturbing function V. Solving this plane problem is reduced to calculating quadratures. In the Hill approximation, these quadratures take a specific form and can be calculated analytically.

At $\sin i = 0$, system (14) can be transformed by introducing more convenient variables,

$$\zeta = \sqrt{1-e^2}, \quad (15)$$

$$\psi = \tilde{\Omega} + \sigma\omega = \Omega + \sigma\omega - \lambda', \quad (16)$$

where $\sigma = {\rm sgn}(\cos i_0) = \pm 1$. Therefore, physically, the angular variable ψ means the difference between the longitude of the pericenter of the satellite orbit, $\Omega + \sigma\omega$, and the mean longitude of the perturbing body, λ'.

Written in the new variables, the evolutionary system

$$\frac{d\zeta}{d\tau} = -20\sigma(1-\zeta^2)\sin 2\psi, \qquad (17)$$
$$\frac{d\psi}{d\tau} = -\nu + 4\sigma\zeta(1+5\cos 2\psi)$$

has the first integral

$$\zeta + \frac{2\sigma}{\nu}(1-\zeta^2)(1+5\cos 2\psi) = c_1, \qquad (18)$$

where the constant c_1 is determined by the initial values of ζ_0 and ψ_0.

Qualitative Analysis

Since the variable ψ enters into integral (18) via $\cos 2\psi$ and since the equalities

$$\frac{d\zeta}{d\tau} = \frac{d\zeta}{d\psi} = 0 \qquad (19)$$

hold at $\sin 2\psi = 0$, all of the integral curves are symmetric relative to the vertical $\psi = 0, \pi/2, \pi$, and $3\pi/2$ straight lines. Therefore, it will suffice to consider the solution of system (17) only for $0 \le \psi \le \pi/2$. In addition, the $\zeta = 1$ boundary line (circular orbits) is the integral straight line on which equalities (19) hold for any ψ.

In the ψ, ζ plane, the angular points of the rectangular region under consideration have the coordinates A(0, 0), B(0, 1), C($\pi/2$, 1), and D($\pi/2$, 0) and correspond to the following special values of the constant c_1:

$$c_1(\mathrm{A}) = \frac{12\sigma}{\nu}, \quad c_1(\mathrm{B}) = c_1(\mathrm{C}) = 1,$$
$$c_1(\mathrm{D}) = -\frac{8\sigma}{\nu}.$$

The boundaries of the rectangle ABCD also correspond to the special values of c_1 that depend on σ, ζ_0, and ψ_0:

(1) on the vertical straight line AB($\psi_0 = 0$) $c_1 = \zeta_0 + \frac{12\sigma}{\nu}(1-\zeta_0^2)$,

(2) on the horizontal straight line BC($\zeta_0 = 1$) $c_1 = 1$,

(3) on the vertical straight line CD($\psi_0 = \pi/2$) $c_1 = \zeta_0 - \frac{8\sigma}{\nu}(1-\zeta_0^2)$,

(4) on the horizontal straight line DA($\zeta_0 = 0$) $c_1 = \frac{2\sigma}{\nu}(1+5\cos 2\psi_0)$.

It follows from the second equation of (17) that $\frac{d\psi}{d\tau} < 0$ at $\nu > 16$ if $\sigma = -1$ and at $\nu > 24$ if $\sigma = 1$. These conditions are definitely satisfied in actual satellite systems.

At $\zeta = 0$, we obtain $\frac{d\zeta}{d\tau} = -20\sigma\sin 2\psi$, $\frac{d\psi}{d\tau} = -\nu$; hence,

$$\frac{d\zeta}{d\psi}\Big|_{\zeta=0} = -\frac{20\sigma}{\nu}\sin 2\psi. \qquad (20)$$

Therefore, at $\sin 2\psi \ne 0$, there exists a set of phase trajectories inclined to the $\zeta = 0$ axis at a finite angle. Moving along such trajectories, the phase point reaches this axis in a finite time; i.e., the eccentricity of the satellite orbit reaches unity, and the satellite falls to the central planet. In other words, in the plane case of the problem under consideration, there exists a set of initial values of ζ_0 and ψ_0 that correspond to the so-called "fall trajectories." Such trajectories are known in the doubly averaged Hill problem (Lidov 1961; Kozai 1962) and in the satellite case of the doubly averaged plane restricted elliptical three-body problem (Aksenov 1979a, 1979b).

In the problem under consideration, the set of fall trajectories is separated from the "regular" trajectories with limited variations in eccentricity (or variable ζ) by a special integral curve, the separatrix. The following constant corresponds to it:

$$c_1^{(\mathrm{s})} = \frac{2(\sigma+5)}{\nu}. \qquad (21)$$

The variable ζ varies within a limited range,

$$0 < \zeta_{\min} \le \zeta \le \zeta_{\max} \qquad (22)$$

for $c_1^{(\mathrm{s})} < c_1 \le 1$ and reaches zero for $c_{1\,\min} = \frac{2(\sigma-5)}{\nu} \le c_1 \le c_1^{(\mathrm{s})}$. Note also that the trajectories starting (or ending) at the point with the coordinates

$$\psi = \frac{1}{2}\arccos\left(-\frac{1}{5}\right) \text{ and } \zeta = 0 \qquad (23)$$

correspond to $c_1 = 0$, while only zero values of ζ correspond to $c_1 = c_{1\,\min}$.

Figure 1 shows a family of phase trajectories of system (17) in the entire ψ range for $\nu = 100/3$ and prograde orbits ($\sigma = 1$), while Fig. 2 corresponds to retrograde orbits ($\sigma = -1$). The values of c_1 are shown on each trajectory. The direction of the motion along all trajectories corresponds to a monotonic decrease in the variable ψ. The maximum values of ζ on the separatrixes can be determined from the formulas

$$\bar{\zeta} = (\sqrt{640+\nu^2} - \nu)/16 \text{ at } \sigma = 1, \qquad (24)$$

$$\bar{\bar{\zeta}} = (\sqrt{960+\nu^2} - \nu)/24 \text{ at } \sigma = -1. \qquad (25)$$

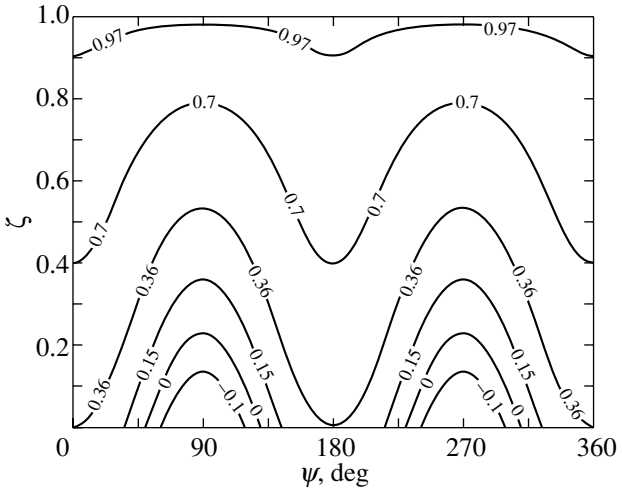

Fig. 1. Family of phase trajectories of system (17) for $\nu = 100/3$ and $\sigma = 1$. The values of c_1 are shown on each trajectory.

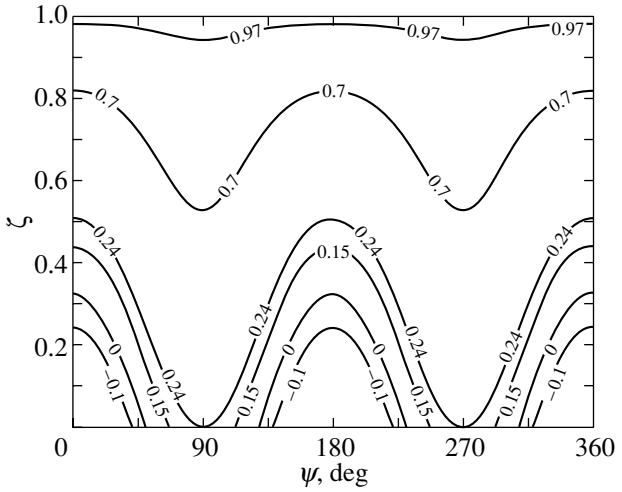

Fig. 2. Same as Fig. 1 for $\sigma = -1$.

The $\sigma = 1$ and $\sigma = -1$ cases differ not only in the shift of all trajectories of the families by 90°, but also in the parameters $\bar{\zeta}$, $\bar{\bar{\zeta}}$, and $c_1^{(s)}$. In particular, fall trajectories for the parameter ν adopted in the figures exist at $c_1 \le 0.36$ ($\sigma = 1$) and $c_1 \le 0.24$ ($\sigma = -1$).

An Analytical Solution

Expressing the variable ψ from integral (18) as a function of ζ and substituting it into the first equation of (17) yields

$$\tau = \frac{\sigma}{8\sqrt{6}} \int\limits_{\zeta_0}^{\zeta} \frac{d\xi}{\sqrt{(\xi-\xi_1)(\xi-\xi_2)(\xi-\xi_3)(\xi-\xi_4)}}. \tag{26}$$

The roots of the fourth-degree polynomial ξ_i ($i = 1, 2, 3, 4$) and the extreme values of ζ are given by the formulas that are presented in the table and that differ for $\sigma = 1$ and $\sigma = -1$.

Below, we consider only the regular trajectories for which $\zeta_{\min} > 0$. Slightly simplifying the problem, we set ζ_0 equal to the minimum value of $\zeta_{\min}$ and, accordingly, $\psi_0 = \pi(1-\sigma)/4$. Inverting quadrature (26), we can easily express $\zeta(\tau)$ in terms of Jacobi elliptic functions,

$$\zeta(\tau) = \left\{ \begin{array}{ll} \dfrac{\xi_4 - \dfrac{\xi_1-\xi_4}{\xi_1-\xi_2}\xi_2 \mathrm{sn}^2 u}{1 - \dfrac{\xi_1-\xi_4}{\xi_1-\xi_2}\mathrm{sn}^2 u}, & \sigma = 1 \\ \dfrac{\xi_2 - \dfrac{\xi_3-\xi_2}{\xi_3-\xi_4}\xi_4 \mathrm{sn}^2 u}{1 - \dfrac{\xi_3-\xi_2}{\xi_3-\xi_4}\mathrm{sn}^2 u}, & \sigma = -1 \end{array} \right\}, \tag{27}$$

where the argument u and the modulus q of the elliptic function sn are defined by the fomulas

$$u = 4\sqrt{6(\xi_1-\xi_2)(\xi_3-\xi_4)}\tau, \tag{28}$$

$$q = \sqrt{\frac{(\xi_1-\xi_4)(\xi_3-\xi_2)}{(\xi_3-\xi_4)(\xi_1-\xi_2)}}. \tag{29}$$

The function $\psi(\tau)$ can be found using integral (18),

$$\cos 2\psi(\tau) = \frac{1}{5}\left\{1 - \frac{\sigma\nu[c_1 - \zeta(\tau)]}{2[1-\zeta^2(\tau)]}\right\}. \tag{30}$$

The period of the ζ and ψ variations (in normalized time τ) is given by

$$T_1 = \frac{\mathbf{K}(q)}{\sqrt{6(\xi_1-\xi_2)(\xi_3-\xi_4)}}, \tag{31}$$

where $\mathbf{K}$ is the complete elliptic integral of the first kind with the modulus q.

In the simplest case of circular orbits, where $e_0 = 0$, $\zeta_0 = 1$, $q = 0$, and $\mathbf{K} = \pi/2$, the expression for T_1 is simplified, and the frequency of the ζ, ψ variations can be determined from the formula

$$\omega_{\zeta\psi}^2 = (\nu + 16\sigma)(\nu - 24\sigma). \tag{32}$$

Clearly, this oscillatory motion is possible only at $\nu > 24$ and $\nu > 16$ for $\sigma = 1$ and $\sigma = -1$, respectively.

A CIRCULAR PARTICULAR SOLUTION

It follows from the second equation of system (14) that $\dfrac{de}{d\tau} = 0$ at $e = 0$; i.e., circular orbits serve as its

Table

$\sigma = 1$	$\sigma = -1$
$\xi_1 = (-\nu + \sqrt{D_1^{(+)}})/16,$	$\xi_1 = (\nu + \sqrt{D_1^{(-)}})/16,$
$\xi_2 = (-\nu - \sqrt{D_1^{(+)}})/16,$	$\xi_2 = (\nu - \sqrt{D_1^{(-)}})/16,$
$\xi_3 = (\nu + \sqrt{D_2^{(+)}})/24,$	$\xi_3 = (-\nu + \sqrt{D_2^{(-)}})/24,$
$\xi_4 = (\nu - \sqrt{D_2^{(+)}})/24,$	$\xi_4 = (-\nu - \sqrt{D_2^{(-)}})/24,$
$D_1^{(+)} = 256 + 32\nu c_1^{(+)} + \nu^2,$	$D_1^{(-)} = 256 - 32\nu c_1^{(-)} + \nu^2,$
$D_2^{(+)} = 576 - 48\nu c_1^{(+)} + \nu^2,$	$D_2^{(-)} = 576 + 48\nu c_1^{(-)} + \nu^2,$
$c_1^{(+)} = \zeta_0 + 2(1 - \zeta_0^2)(1 + 5\cos 2\psi_0)/\nu,$	$c_1^{(-)} = \zeta_0 - 2(1 - \zeta_0^2)(1 + 5\cos 2\psi_0)/\nu,$
$\zeta_{\min} = \xi_4, \zeta_{\max} = \xi_1$	$\zeta_{\min} = \xi_2, \zeta_{\max} = \xi_3$

particular solution. By introducing the new variable $z = \cos i$, we can transform the evolutionary system at $e = 0$ to

$$\frac{dz}{d\tau} = -4(1 - z^2)\sin 2\tilde{\Omega}, \qquad (33)$$
$$\frac{d\tilde{\Omega}}{d\tau} = -\nu - 8z\sin^2\tilde{\Omega}$$

with its first integral

$$z + \frac{4}{\nu}(z^2 - 1)\sin^2\tilde{\Omega} = c_2, \qquad (34)$$

where the constant c_2 is determined by the initial values of z_0 and $\tilde{\Omega}_0$.

Qualitative Analysis

Since the variable $\tilde{\Omega}$ enters into integral (34) via $\sin^2\tilde{\Omega}$ (or $\cos 2\tilde{\Omega}$) and since the equalities

$$\frac{dz}{d\tau} = \frac{dz}{d\tilde{\Omega}} = 0 \qquad (35)$$

hold at $\sin 2\tilde{\Omega} = 0$, all of the integral curves are symmetric relative to the vertical $\tilde{\Omega} = 0, \pi/2, \pi$, and $3\pi/2$ straight lines. Therefore, it will suffice to consider the solution of system (33) only at $0 \le \tilde{\Omega} \le \pi/2$. In addition, the $z = \pm 1$ boundary lines (plane orbits) are the integral straight lines on which equalities (35) hold for any $\tilde{\Omega}$. In the $\tilde{\Omega}$, z plane, the angular points of the rectangular region under consideration have the coordinates A(0, −1), B(0, 1), C($\pi/2$, 1), and D($\pi/2$, −1) and correspond to the following special values of the constant c_2:

$$c_2(\mathrm{A}) = c_2(\mathrm{D}) = -1, \quad c_2(\mathrm{B}) = c_2(\mathrm{C}) = 1.$$

The boundaries of the rectangle ABCD also correspond to the special values of c_2 that depend on z_0:

(1) on the vertical straight line AB($\tilde{\Omega}_0 = 0$) $c_2 = z_0$,

(2) on the horizontal straight line BC($z_0 = 1$) $c_2 = 1$,

(3) on the vertical straight line CD($\tilde{\Omega}_0 = \pi/2$) $c_2 = z_0 - \frac{4}{\nu}(1 - z_0^2)$,

(4) on the horizontal straight line DA($z_0 = -1$) $c_2 = -1$.

It follows from the second equation of (33) that $\frac{d\tilde{\Omega}}{d\tau} < 0$ at any ν if $z > 0$ and at $\nu > 8$ if $z < 0$; this condition is definitely satisfied in actual satellite systems. The variation in the variable z is oscillatory in pattern, while its extreme values are defined by the formulas

$$z_{\min} = c_2, \qquad (36)$$
$$z_{\max} = \{-\nu + [\nu^2 + 16(4 + \nu c_2)]^{1/2}\}/8.$$

Figure 3 shows a family of phase trajectories of system (33) for $\nu = 100/3$ in the entire $\tilde{\Omega}$ range. The values of c_2 are shown on each trajectory. The direction of the motion along all trajectories corresponds to a monotonic decrease in the variable $\tilde{\Omega}$. In addition to the typical integral curves corresponding to $c_2 = \pm 0.9$ and ± 0.5, Fig. 3 shows two trajectories for $c_2 = 0$ and $c_2 = -4/\nu = -0.12$. For arbitrary ν, these trajectories bound the domain of variables in which the type of a nearly orthogonal evolving orbit can change from prograde ($z > 0$) to retrograde ($z < 0$) and vice versa at $-4/\nu < c_2 < 0$.

An Analytical Solution

Expressing the variable $\tilde{\Omega}$ from integral (34) as a function of z and substituting it into the first equation

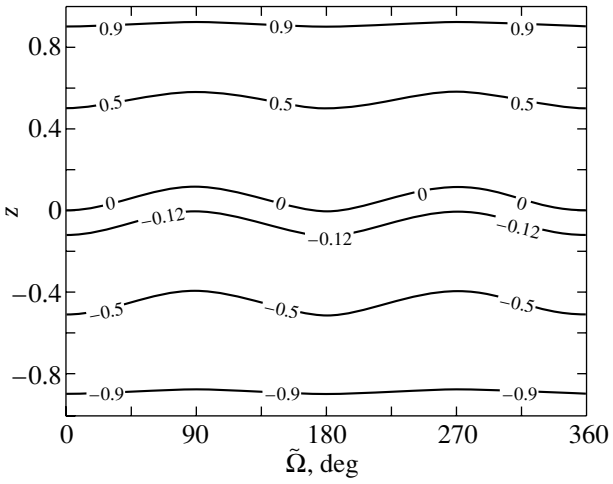

Fig. 3. Family of phase trajectories of system (40) for $\nu = 100/3$. The values of c_2 are shown on each trajectory.

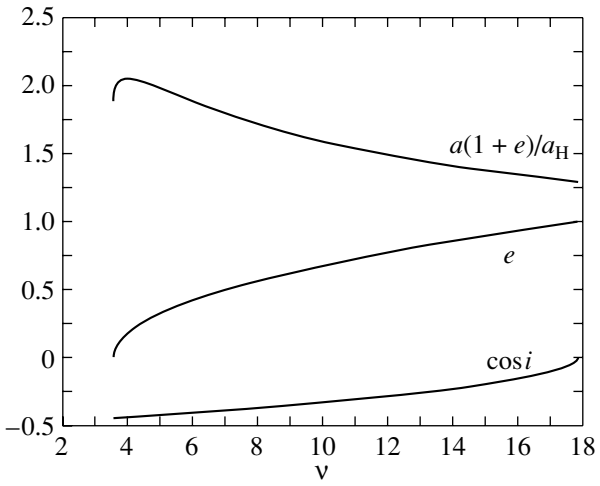

Fig. 4. Orbital parameters e and $\cos i$ for the stationary solution of system (14) and the ratio of the apocenter distance $a(1+e)$ to the radius of the Hill sphere $a_{\rm H}$ versus ν.

of (33) yields

$$\tau = \frac{1}{4\sqrt{\nu}} \int_{z_0}^{z} \frac{d\eta}{\sqrt{-(\eta-\eta_1)(\eta-\eta_2)(\eta-\eta_3)}}. \quad (37)$$

The roots of the third-degree polynomial η_i $(i = 1, 2, 3)$ are given by

$$\eta_1 = z_{\max}, \quad \eta_2 = \{-\nu - [\nu^2 + 16(4+\nu c_2)]^{1/2}\}/8,$$
$$\eta_3 = z_{\min},$$

where the extreme values of z are defined by formulas (36). Just as in the case of plane orbits, we set, for simplification, $z_0 = z_{\min}$ and, accordingly, $\tilde{\Omega}_0 = 0$. Inverting quadrature (37), we can easily express $z(\tau)$ in terms of Jacobi elliptic functions,

$$z(\tau) = \frac{\eta_3 - \eta_2 p^2 \mathrm{sn}^2 w}{1 - p^2 \mathrm{sn}^2 w},$$

where the argument w and the modulus p of the elliptic function sn are defined by the formulas

$$w = 2\sqrt{\nu(\eta_1 - \eta_2)}\tau, \quad (38)$$

$$p = \sqrt{\frac{\eta_1 - \eta_3}{\eta_1 - \eta_2}}. \quad (39)$$

The function $\tilde{\Omega}(\tau)$ can be found using integral (34),

$$\sin^2 \tilde{\Omega}(\tau) = \frac{\nu[z(\tau) - c_2]}{4[1 - z^2(\tau)]}. \quad (40)$$

The period of the z variation (in normalized time $\tau, \tilde{\Omega}$) is given by

$$T_2 = \frac{2\mathbf{K}(p)}{\sqrt{\nu(\eta_1 - \eta_2)}}, \quad (41)$$

where $\mathbf{K}$ is the complete elliptic integral of the first kind with the modulus p.

In the simplest case of plane orbits, where $\sin i_0 = 0$, $z_0 = \cos i_0 = \sigma = \pm 1$, $p = 0$, and $\mathbf{K} = \pi/2$, the expression for T_2 is simplified, and the frequency of the z and $\tilde{\Omega}$ variations can be determined from the formula

$$\omega^2_{z\tilde{\Omega}} = \nu(\nu + 8\sigma). \quad (42)$$

Clearly, this oscillatory motion is possible at any positive ν for $\sigma = 1$ and only at $\nu > 8$ for $\sigma = -1$.

A STATIONARY PARTICULAR SOLUTION

Setting the right-hand sides of Eqs. (14) equal to zero, we can determine the conditions for the existence of a formal stationary solution of the evolutionary system. It is easy to see that the conditions

$$\frac{de}{d\tau} = \frac{di}{d\tau} = 0$$

are satisfied if

$$\sin 2\omega = 0, \quad \delta_1 = \mathrm{sgn}(\cos 2\omega) = \pm 1 \quad (43)$$

and

$$\sin 2\tilde{\Omega} = 0, \quad \delta_2 = \mathrm{sgn}(\cos 2\tilde{\Omega}) = \pm 1.$$

In this case,

$$\frac{d\omega}{d\tau} = \frac{2}{\sqrt{1-e^2}}\{4 + e^2 - 5\sin^2 i + 5\delta_1(\sin^2 i - e^2) + \delta_2[5(2 - e^2 - \sin^2 i)\delta_1 - 2 - 3e^2 + 5\sin^2 i]\},$$

$$\frac{d\tilde{\Omega}}{d\tau} = -\nu - \frac{2}{\sqrt{1-e^2}}[2 + e^2(3 - 5\delta_1)](1 - \delta_2)\cos i.$$

Clearly, there are no stationary solutions at $\delta_2 = 1$ ($\tilde{\Omega} = 0, \pi$), since $\frac{d\tilde{\Omega}}{d\tau} = -\nu < 0$. At $\delta_2 = -1$ ($\tilde{\Omega} = \pm\pi/2$), we have

$$\frac{d\omega}{d\tau} = \frac{4}{\sqrt{1-e^2}}[3 + 2e^2 - 5\sin^2 i - 5\delta_1 \cos^2 i],$$

$$\frac{d\tilde{\Omega}}{d\tau} = -\nu - \frac{4\cos i}{\sqrt{1-e^2}}(2 + 3e^2 - 5\delta_1 e^2).$$

There are no stationary solutions for $\delta_1 = 1$ ($\omega = 0, \pi$) and $e < 1$, since

$$\frac{d\omega}{d\tau} = -8\sqrt{1-e^2} < 0.$$

At $\delta_1 = -1$ ($\omega = \pm\pi/2$), we have

$$\frac{d\omega}{d\tau} = \frac{8}{\sqrt{1-e^2}}(e^2 - 1 + 5\cos^2 i),$$

$$\frac{d\tilde{\Omega}}{d\tau} = -\nu - \frac{8}{\sqrt{1-e^2}}(1 + 4e^2)\cos i,$$

and the dependences of the stationary values of e and $\cos i$ on ν are expressed by the following formulas, which are valid in the range

$$8/\sqrt{5} \approx 3.6 \le \nu \le 8\sqrt{5} \approx 17.9, \qquad (44)$$

$$e = \sqrt{\frac{\nu\sqrt{5} - 8}{32}}, \quad \cos i = -\frac{1}{2}\sqrt{1 - \frac{\nu\sqrt{5}}{40}}. \qquad (45)$$

In addition to these dependences, Fig. 4 shows the ν dependence of the ratio of the apocenter distance $a(1+e)$ to the radius of the Hill sphere $a_{\rm H}$, where a is defined by the approximate formula (4). Clearly, the stationary solution obtained is only formal, since it corresponds to a ν range in which $a(1+e) > a_{\rm H}$. Nevertheless, our analysis of the evolutionary system (14) linearized in small deviations from the stationary values of the elements e, i, ω, and $\tilde{\Omega}$ shows that this formal stationary solution is stable in the linear approximation over the entire ν range (44).

CONCLUDING REMARKS

We qualitatively analyzed particular solutions of the singly averaged Hill problem and derived formulas for their analytical description using Jacobi elliptic functions. A family of "fall trajectories" corresponding to $e \to 1$, where the satellite collides with the central planet in a finite time, was found to exist in the plane solution.

Investigating the stability of the plane solution to inclination and the circular solution to eccentricity as well as searching for and constructing periodic trajectories of the nonintegrable problem under consideration are of considerable interest.

The problem considered here (as any averaged problem) is only the first approximation of the perturbation theory. To obtain more accurate solutions, it would probably be appropriate to analyze the problem using at least the second approximation.

ACKNOWLEDGMENTS

I wish to thank N.M. Teslenko for his help in preparing this paper.

REFERENCES

1. V. K. Abalakin, E. P. Aksenov, E. A. Grebenikov, *et al.*, *A Reference Manual on Celestial Mechanics and Astrodynamics* (Nauka, Moscow, 1976) [in Russian].
2. E. P. Aksenov, Astron. Zh. **56**, 419 (1979a) [Sov. Astron. **23**, 236 (1979a)].
3. E. P. Aksenov, Astron. Zh. **56**, 623 (1979b) [Sov. Astron. **23**, 351 (1979b)].
4. E. A. Grebenikov and Yu. A. Ryabov, *New Qualitative Methods in Celestial Mechanics* (Nauka, Moscow, 1971) [in Russian].
5. Y. Kozai, Astron. J. **67**, 591 (1962).
6. M. L. Lidov, Iskusstv. Sputniki Zemli **8**, 5 (1961).
7. N. D. Moiseev, Tr. Gos. Astron. Inst. im. P.K. Shternberga **XV**, 75 (1945a).
8. N. D. Moiseev, Tr. Gos. Astron. Inst. im. P.K. Shternberga **XV**, 100 (1945b).
9. M. A. Vashkov'yak and N. M. Teslenko, Pis'ma Astron. Zh. **31**, 154 (2005) [Astron. Lett. **31**, 140 (2005)].

Translated by V. Astakhov

Astronomy Letters, Vol. 31, No. 7, 2005, pp. 494–499. Translated from Pis'ma v Astronomicheskiĭ Zhurnal, Vol. 31, No. 7, 2005, pp. 553–559.

Evolution of the Velocity Field in Model Potentials

V. V. Orlov*

Sobolev Astronomical Institute, St. Petersburg State University, Universitetskiĭ pr. 28, St. Petersburg, Peterhof, 198504 Russia

Received November 2, 2004

Abstract—We consider the evolution of the structure of the velocity field formed by the loops of the trajectory in a generalized Hénon–Heiles model potential. Box-shaped orbits alternating with periodic trajectories are shown to dominate at low values of the energy integral. Signatures of shell- and tube-shaped structures appear as the energy increases. Tube-shaped orbits are associated with stable periodic trajectories with small resonance ratios. Zones of stochastic orbits appear at values of the energy integral close to its critical value, which corresponds to the opening of the zero-velocity contour.

Key words: *velocity field, structural evolution, model potential.*

The dynamics of a stellar system is determined by the orbits that are described by its stars. In galaxies composed of billions of stars and interstellar matter, the stellar orbits are determined almost exclusively by the smoothed regular gravitational field produced by the combined effect of their constituent objects. Since the irregular field associated with individual encounters between stars is generally weak compared to the regular field, it can be disregarded.

The properties of orbits in the axisymmetric and triaxial models of galactic gravitational fields are reviewed in the monograph by Contopoulos (2002). In particular, this author points out that periodic orbits play an important role in forming the phase portrait of the system. Stable periodic orbits form a kind of a skeleton on which the main types of orbits rest. At the same time, unstable periodic orbits produce regions of stochastic motions. Numerical simulations for a number of potentials showed (see, e.g., Hénon and Heiles 1964; Contopoulos 2002) that the relative area of the regions of stochastic motions increases with energy. This can be clearly displayed on the Poincaré section where the points for stochastic trajectories are scattered randomly. The islands of regularity around stable periodic trajectories form hierarchical, occasionally nested structures on the Poincaré section. The initial conditions for regular periodic orbits form linear Farey-tree-type structures. Irregular periodic orbits are concentrated toward the asymptotic curves for unstable periodic orbits and within the "tangles" of trajectories around homoclinic points (see also the paper by Barbanis and Contopoulos (1995) for three-dimensional systems).

To better understand how the manifolds of orbits are structured, we consider a model potential that is a generalization of the standard Hénon–Heiles (1964) model. The potential is

$$U(R,z) = -\frac{1}{2}\left(AR^2 + Bz^2\right) + \varepsilon R z^2 + \mu R^3, \quad (1)$$

where (R, z) are the coordinates of the trial point, and (A, B, ε, μ) are the parameters of the model. We consider the following set of parameters:

$$A = 3, \quad B = 2, \quad \varepsilon = -1, \quad \mu = 1/3. \quad (2)$$

We are interested in the change in the structure of the velocity field when varying the initial conditions and the energy integral I. The velocity field is determined by the angle f between the system's R axis of symmetry and the tangent to the trajectory at the point with coordinates (R, z).

The equation for the variation in the angle f is

$$2\,(U+I)\left(\frac{\partial f}{\partial R}\cos f + \frac{\partial f}{\partial z}\sin f\right) + \frac{\partial U}{\partial R}\sin f - \frac{\partial U}{\partial z}\cos f = 0. \quad (3)$$

Agekyan (1972) was the first to derive this equation using the Boltzmann equation for three-dimensional fields with rotational symmetry. However, Eq. (3) can also be obtained directly from the equations of motion

$$\frac{d^2R}{dt^2} = \frac{\partial U}{\partial R}, \qquad \frac{d^2z}{dt^2} = \frac{\partial U}{\partial z}. \quad (4)$$

*E-mail: vor@astro.spbu.ru

1063-7737/05/3107-0494$26.00

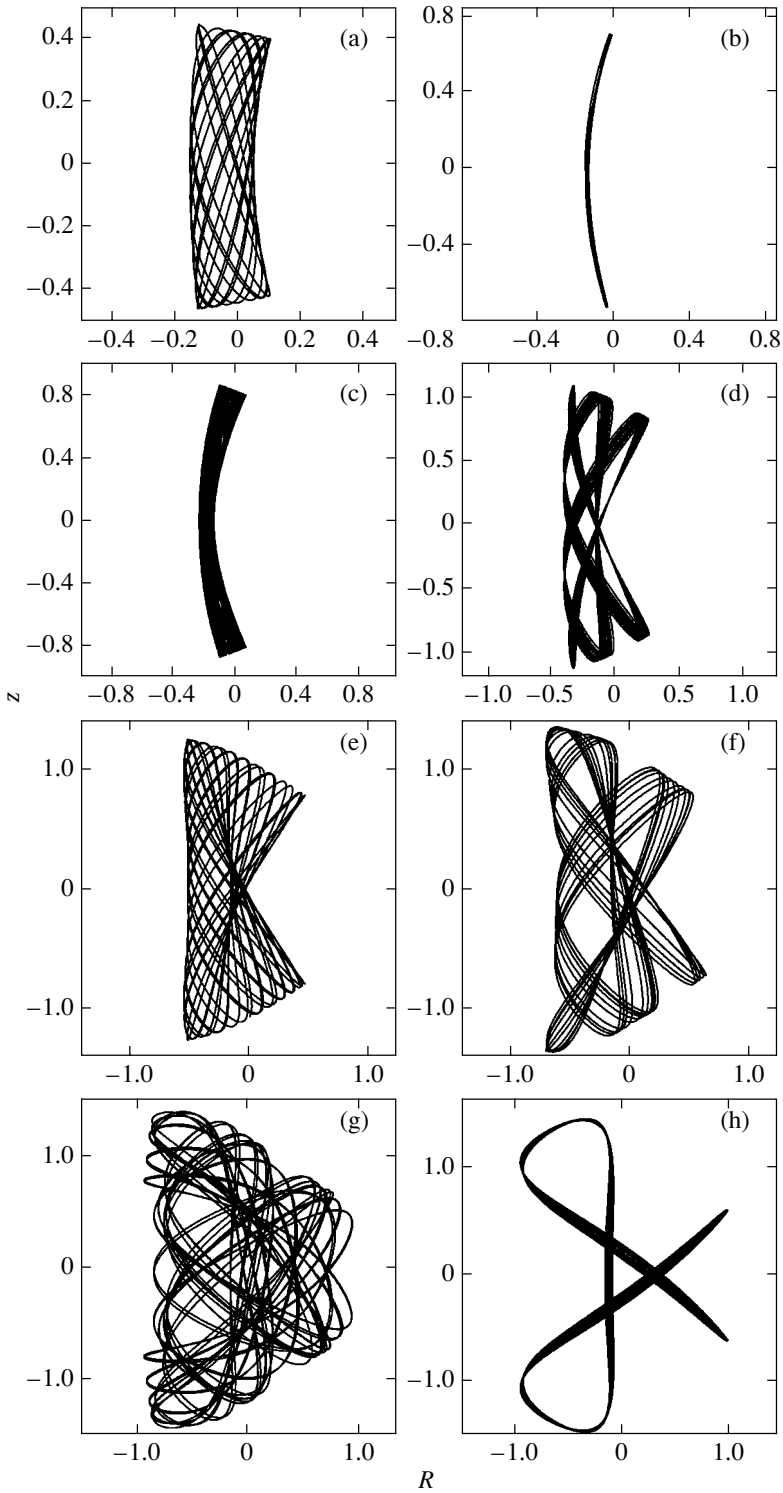

Fig. 1. Family of orbits at $R_0 = -0.15$ for the following values of the energy integral: $I =$ (a) 0.2, (b) 0.5, (c) 0.7, (d) 1.0, (e) 1.2, (f) 1.4, (g) 1.6, and (h) 1.9.

This was done by Sidorova (2000) in her senior research project.

The behavior of the velocity field when varying the initial conditions can be studied by numerically solving Eq. (3) or the equivalent system (4). Since Eq. (3) is a partial differential equation, it seems preferable to numerically solve system (4) to maintain a higher accuracy. To this end, we use the classical fourth-order Runge–Kutta method.

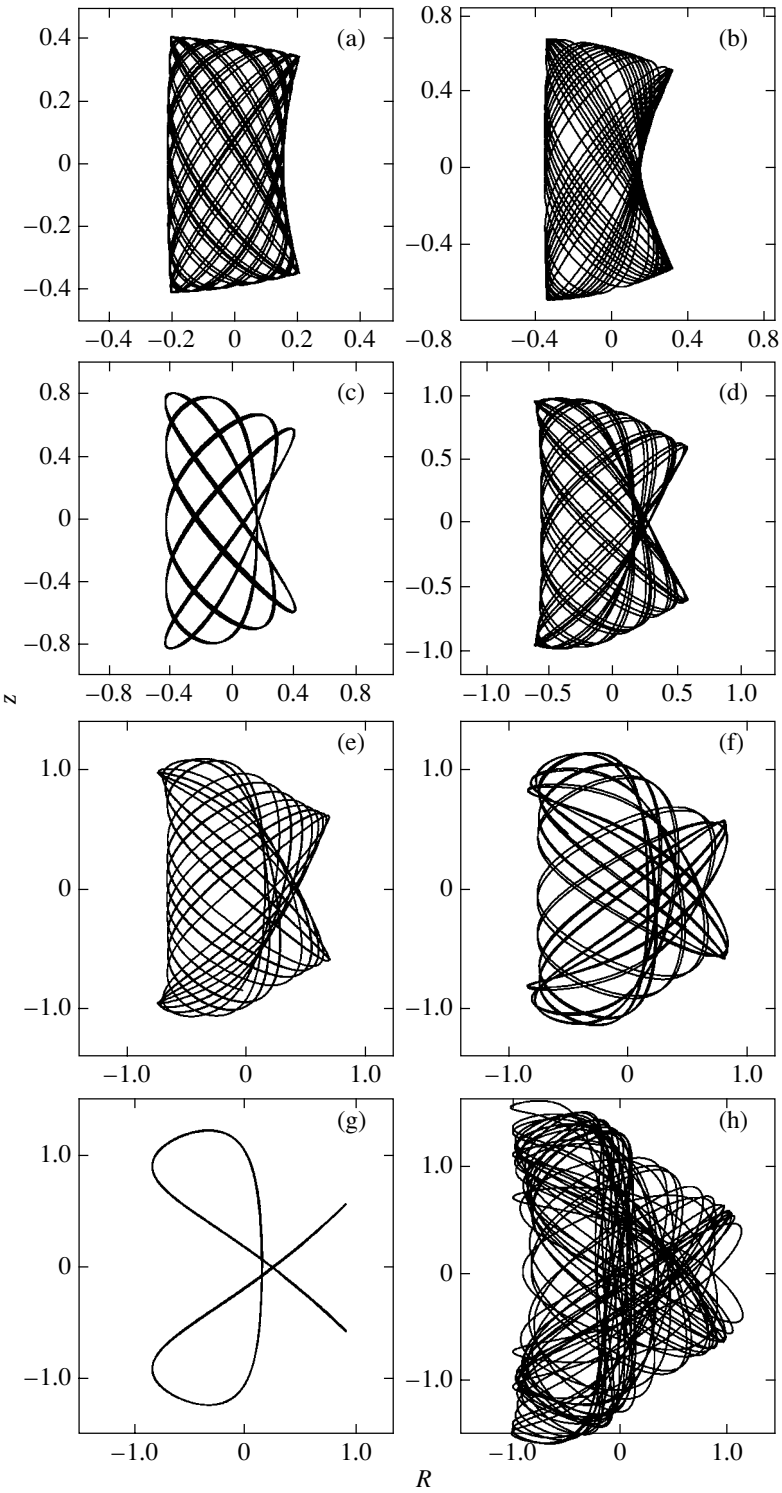

Fig. 2. Family of orbits at $R_0 = 0.15$. The values of the energy integral are the same as those in Fig. 1.

Figures 1a–1h show how the types of orbits change with increasing energy integral for fixed initial conditions—the coordinates of the starting point of the orbit, $(R_0, z_0) = (-0.15, 0)$, and the direction of particle motion, $f_0 = 90°$. At low $I \leq 1$, box-shaped orbits alternate with periodic trajectories. One of these is the so-called central orbit. Figure 1b shows a trajectory close to it.

At higher $I > 1$, we see new structural elements of the velocity field—pleats (or folds) of the velocity

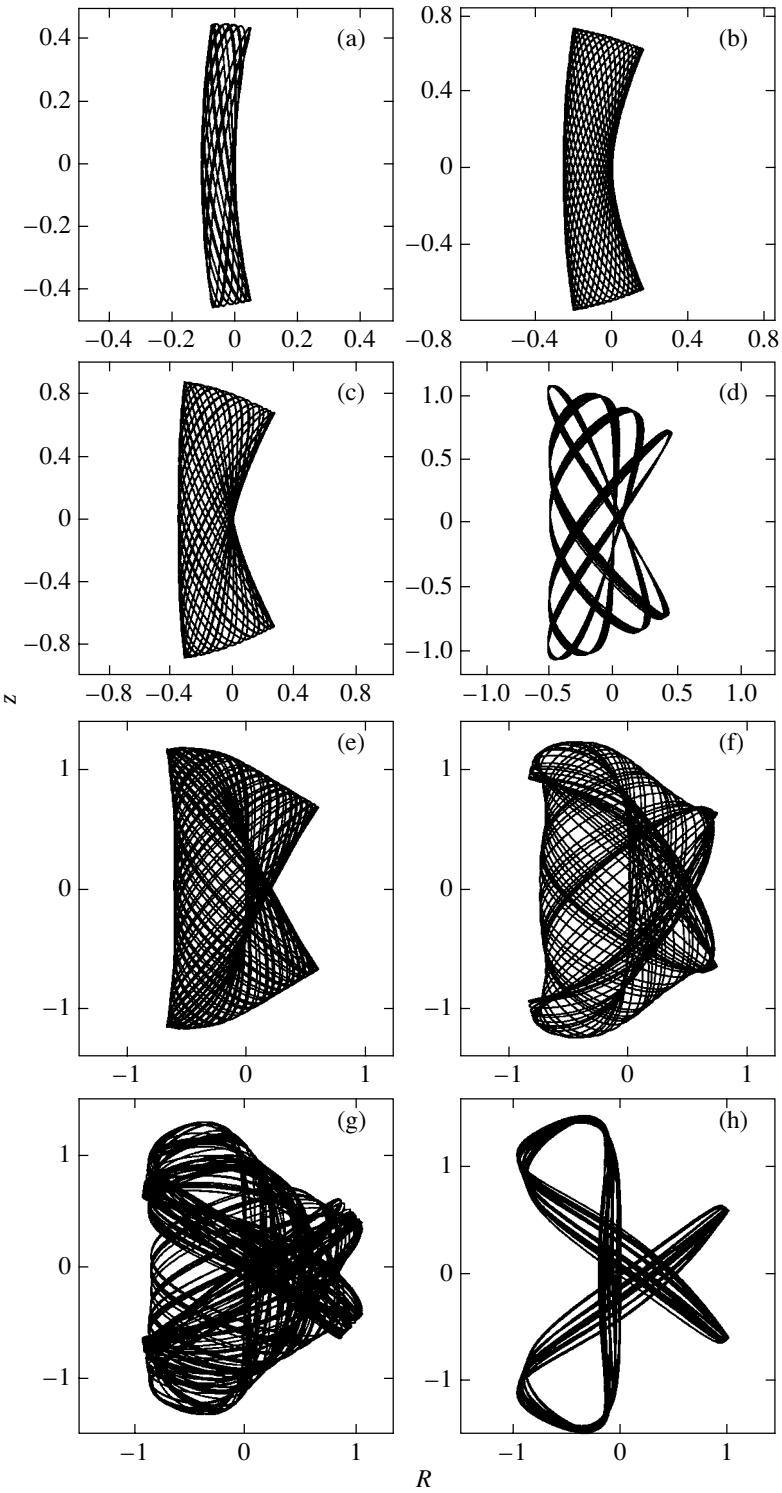

Fig. 3. Family of orbits at $R_0 = 0$. The values of the energy integral are the same as those in Fig. 1.

field (Fig. 1e), the appearance of tube-shaped orbits (Fig. 1f), stochasticity signs (Fig. 1g), and new periodic orbits (Fig. 1h).

Let us consider the initial conditions that are symmetric about the coordinate origin $(R_0, z_0) = (0.15, 0)$ at $f_0 = 90°$ (Figs. 2a–2h). At $I \leq 1$, the overall pattern of change in the velocity-field structure

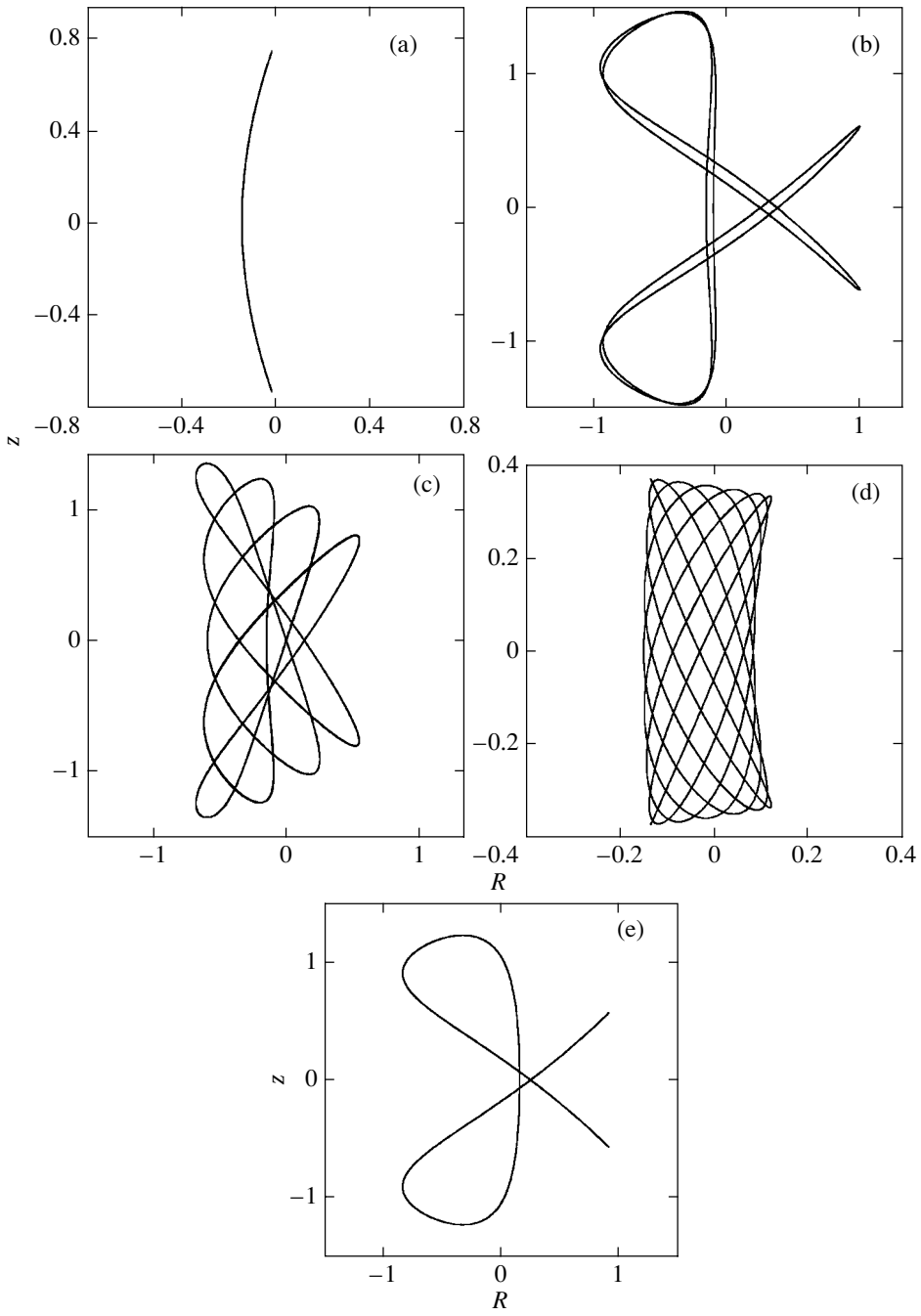

Fig. 4. Examples of periodic orbits at $R_0 = -0.15$ for various values of the energy integral: $I =$ (a) 0.5351, (b) 1.9136, (c) 1.3926, and (d) 0.1475. Figure 4e shows a periodic orbit with two cuspidal points at $R_0 = 0.15$ for $I = 1.5955$.

with increasing energy is generally retained: box-shaped orbits alternating with periodic trajectories are observed (Figs. 2a–2d). A pleat (fold) is formed on the right side of the box. The multiplicity of the velocity field is equal to four inside this fold, while only two conjugate loops of the trajectory intersect in the remaining part of the orbit region.

The shape of the orbit region changes with increasing I—curvatures are formed in the left corners of the box. The orbit acquires the features of initially a shell-shaped structure and subsequently a tube-shaped structure produced by the periodic orbit shown in Fig. 2g. As the energy increases further, the orbit becomes stochastic (Fig. 2h). At $I = I_{\text{crit}} = 11/6 \approx 1.833\ldots$, the zero-velocity contour breaks. At $I > I_{\text{crit}}$, the trajectory can go to infinity after a number of oscillations.

We also performed computations for $R_0 = 0$ (Figs. 3a–3h). The behavior of the structure of the velocity field with increasing I generally remains the same: box-shaped orbits alternate with periodic trajectories. In this case, the sizes and curvature of the box boundaries increase. Structurally, the orbits at $R_0 = 0$ are intermediate between the orbits at $(R_0, z_0) = (-0.15, 0)$ and $(R_0, z_0) = (0.15, 0)$ for the same energy integral.

As can be seen from Figs. 1–3, the phase portrait is largely determined by periodic and nearly periodic orbits. Let us identify the main types of periodic orbits at the values of R_0 under consideration. At $(R_0, z_0) = (-0.15, 0)$, the stable central periodic orbit occupies a special position (Fig. 4a). It is surrounded by narrow box-shaped orbits. As the energy integral increases, more complex periodic orbits appear. Figures 4b and 4c show two examples. These are the closed orbits that do not reach the zero-velocity contour. On the other hand, there are also periodic orbits with the cuspidal points on the zero velocity contour; Fig. 4d shows one of these orbits.

At other R_0, new periodic orbits can appear, while no other orbits are observed. For example, at $R_0 = 0$ and $R_0 = 0.15$, there is no central periodic orbit shown in Fig. 4a. At the same time, another simple periodic orbit with two cuspidal points was found at $R_0 = 0.15$ (Fig. 4e). This orbit produces a family of tube-shaped orbits. It is similar to the orbit shown in Fig. 4b at $R_0 = -0.15$, but its period is a factor of 2 shorter. At certain R_0 and I, the orbit shown in Fig. 4e probably bifurcates (the period doubles). The initial orbit becomes unstable (see Contopoulos 2002). As a result, closed orbits that do not reach the zero-velocity contour appear (see Fig. 4b). Such orbits also produce tube-shaped orbits (see Figs. 1h and 3h).

Thus, the structure of the field of directions formed by the trajectory loops depends on the initial conditions. At low energies, the orbits are box-shaped. They alternate with periodic orbits resembling boxes in shape. The limiting case of a box is the central periodic orbit (Fig. 4a) where the lateral sides of the box shrink into a single line.

The commensurabilities between the oscillation frequencies along the R and z axes can be arbitrarily high. Since the set of rational numbers is infinite and everywhere dense, there is a periodic orbit in an arbitrarily close neighborhood of any orbit. However, only some of these orbits (with the frequency ratio equal to the ratio of small integer numbers) play a significant role in forming the global structure of the velocity field and its changes.

It should be noted that the orbits of a particle on the (R, z) plane are the projections of phase trajectories in the four-dimensional space. In particular, the box-shaped and tube-shaped orbits that we identified are the projections of the conditionally periodic trajectories wound around the invariant tori in phase space onto coordinate space. The highlighted features like folds (see, e.g., Figs. 1e–3e) and curvatures (Fig. 3g) are examples of the standard features of projecting an invariant torus onto the coordinate space (see, e.g., Lichtenberg and Liebermann 1984; Contopoulos 2002).

The structure of the neighborhoods of periodic orbits was analyzed in detail in the KAM theory (see, e.g., the review by Arnold *et al.* 1985). According to this theory, a periodic trajectory in dynamical systems with two degrees of freedom in the phase space is surrounded by invariant tori with conditionally periodic trajectories. This is clearly seen from comparison of Figs. 1b and 4a as well as Figs. 1h and 4e. Both stochastic and periodic orbits can be between the invariant tori (see Arnold *et al.* 1985).

Thus, the results presented here clearly illustrate several patterns known in the theory of dynamical systems using the generalized Hénon–Heiles model as a specific example.

1. ACKNOWLEDGMENTS

I am grateful to the Foundation for the Support of Leading Scientific Schools (project no. 1078.2003.02) and the Russian Foundation for Basic Research (project no. 04-02-17447) for their financial support. I wish to thank the referee for several valuable remarks.

REFERENCES

1. T. A. Agekyan, Astron. Zh. **49**, 371 (1972) [Sov. Astron. **16**, 303 (1972)].
2. V. I. Arnold, V. V. Kozlov, and A. I. Neishtadt, Sovremennye Problemy Matematiki. Fundamental'nye Napravleniya **3**, 1 (1985).
3. B. Barbanis and G. Contopoulos, Astron. Astrophys. **294**, 33 (1995).
4. G. Contopoulos, *Order and Chaos in Dynamical Astronomy* (Springer-Verlag, New York, 2002).
5. M. Hénon and C. Heiles, Astron. J. **69**, 73 (1964).
6. A. Lichtenberg and M. Liebermann, *Regular and Stochastic Dynamics* (Mir, Moscow, 1984).
7. V. K. Sidorova, Diploma Work (S.-Peterburg. Gos. Univ., St. Petersburg, 2000).

Translated by A. Dambis

Astronomy Letters, Vol. 31, No. 7, 2005, p. 500.

ERRATA

Erratum: "Strong Cosmic-Ray Scattering in an Anisotropic Random Magnetic Field"

[*Astron. Lett.* 31 (3), 186 (2005)]

Yu. P. Mel'nikov and I. N. Toptygin

1. On p. 187 (left column), the phrase in line 20 from the top should read as "...the cosmic medium for $R_1 \leq L$...".

2. On p. 189 (left column, line 8 from the top of the first paragraph), J rather than I should be used to denote the Bessel function in the unnumbered formula and in the subsequent text:

$$J_n(\rho)\exp\left[\mathrm{in}\frac{\pi-\beta}{2}\right] = \sum_{k=-\infty}^{+\infty} J_{n+k}(z)J_k(z)\exp[ik\beta],$$

where $\rho = 2z\sin(\beta/2)$ and $J_n(\rho)$ is the nth order Bessed function.